Optoelectronic Properties and Applications of 3-D Hybrid a-Si:H/ZnO Nanowire Structures

by

Bright Chijioke Iheanacho

A thesis
presented to the University of Waterloo
in fulfillment of the
thesis requirement for the degree of
Doctor of Philosophy
in
Electrical and Computer Engineering

Waterloo, Ontario, Canada, 2017

Examining Committee Membership

The following served on the Examining Committee for this thesis. The decision of the Examining Committee is by majority vote.

External Examiner	Alberto Salleo Professor of Material Science and Engineering
Supervisor(s)	William S. Wong Professor of Electrical and Computer Engineering
Internal Member	Hany Aziz Professor of Electrical and Computer Engineering
Internal-external Member	Ting Tsui Professor of Chemical Engineering
Other Member(s)	Irene Goldthorpe Professor of Electrical and Computer Engineering

AUTHOR'S DECLARATION

I hereby declare that I am the sole author of this thesis. This is a true copy of the thesis, including any required final revisions, as accepted by my examiners.

I understand that my thesis may be made electronically available to the public.

Abstract

This Ph.D. dissertation presents the study and development of optoelectronic properties of 3-D hybrid zinc oxide nanowire (ZnO NW) and hydrogenated amorphous silicon (a-Si:H) core-shell structures and a demonstration of their application in infrared photodiodes. In addition, the demonstration of infrared photoconductors using the 3-D a-Si:H/ZnO NW structure, which are then integrated onto conventional back channel etched (BCE) a-Si:H thin film transistors (TFTs) for potential large-area sensor applications is also presented.

A hybrid 3-D core-shell structure formed using ZnO NW cores and conformally coated a-Si:H thin film shell was found to be infrared sensitive for wavelengths up to 2.5 μm wavelength. Scattering and multiple reflection enabled by the 3-D morphology were found to enhance the effective thickness of the a-Si:H shell by ~3 orders of magnitude. With the enhanced effective thickness, defects within the a-Si:H material were associated with enabling infrared absorption, achieving up to 73% infrared absorption at 2.3 μm infrared wavelength for 500 nm coated a-Si:H film on 7 μm long ZnO NWs having a nanowire density of 4.3×10^7 NW/cm^2. Comprehensive materials and device characteristics were studied to show a defect mediated infrared absorption process in the 3-D a-Si:H/ZnO NW material system.

3-D infrared photoconductors were fabricated afterwards at a temperature of ≤ 150°C using the infrared sensitive 3-D a-Si:H/ZnO NW hybrid material system. An intentional 'NW gap' was created between the edge of the NW array and the contacts of the infrared photoconductors to minimize parasitic conduction from conductive and connected NWs thereby reducing the dark current of the 3-D photoconductor. An ON/OFF ratio of 3.2×10^2 was achieved for 1 μm thick a-Si:H shell coating on 2.7 μm long ZnO NWs with a nanowire density of 3.9×10^8 NW/cm^2 using 1.55 μm LED illumination.

As an alternative infrared photodetector, 3-D infrared photodiodes were also fabricated using similar process conditions. Dark current as low as 1.6×10^{-9} A/cm^2 was achieved for a diode with NW length vs a-Si:H thickness ratio of 1.5× and NW density of 6.1×10^7 NW/cm^2 giving an infrared signal to noise ratio of 2.5×10^2 with 1.55 μm LED irradiation. The factors that influence the dark currents were studied and several optimizations were implemented. The top contact was optimized by replacing aluminum doped zinc oxide (AZO) top conducting oxide (TCO) with thinned-down, conductive gallium indium zinc oxide (GIZO) and p^+ doped a-Si:H to minimize the window layer absorption and enhance the its infrared transmission.

3-D infrared photoconductors were also integrated onto a-Si:H BCE TFT at a process temperature ≤ 150°C. The process development and the effects of both the structure and the integration process flow were evaluated. A 3× signal to noise ratio due to infrared irradiation using a heat lamp was obtained for the integrated device with a photoconductor section that contains only 20% 3-D a-Si:H/ZnO NW structure.

Acknowledgements

I like to thank my supervisor, Professor William S. Wong, for the opportunity to embark on this journey. I am grateful for your support, advice and mentorship throughout the period. I admit it was rough and I was bruised many times, but there were great lessons learnt afterwards.

I am also grateful to Professor Arokia Nathan who inspired my desire for a Ph.D. during my time with him in UCL. I also appreciate my Ph.D. committee members, Professors Irene Goldthorpe, Hany Aziz and Ting Tsui for serving in my committee. I am especially grateful to Professor Ting Tsui for your encouragement and blanket access to the SEM which helped me with better visualization. Thank you also to Professor Alberto Salleo for accepting to be my external supervisor.

I am most grateful to Dr Czang-Ho Lee for your encouragements and stimulating discussions. I also appreciate Professor Siva Sivoththaman and Joe Street for access to your lab and equipment, Professor Dietmar Knipp and Asman Tamang for collaborations and stimulating discussions and Professor Simmerjeet Saini and Dr Iman Khodadad for letting me use your characterization tools. I am most grateful to Richard Barber for your prompt attention to lab issues preventing breakdown and ensuring downtime is minimized. Thank you also for believing in me and entrusting me responsibilities to care for the PECVD as a user prime. I am also grateful to Dr Mohammad Esmaeili-rad, Dr Feng Chen and Dr Micheal Adachi for helping me to settle into the lab when I first arrived.

I am grateful to the wonderful friends and colleagues who became pillars of support in rough times, buddies during weekend work and comedians when humor is needed. Many thanks to all the members (past and present) of Giga-to-nanoelectronic centre and the AFET group (especially Dr Ali Tari, Dr Minoli Pathirane, Melissa Chow, Nancy Chun Nan, Mohsen Asad, Mohammad Nouri, Philippe Pearson, Pranav Garvinieni among others) for your support and friendship. I also appreciate friends and support groups external to the university, too numerous to mention, who have ensured my stay here

was not boring and depressing. In particular, I appreciate Nelson Obi-Alago and his family for being a true friend and brother in diaspora. Your presence, calls and care were very re-assuring and made a world of difference to me. I also appreciate support from Oby and Mudia Osamwonyi, Toyin and Adeoye Oyedokun, Chris and Maureen Ofenor, Veronica and Mohabir Persaud, Timi Febo and Nonye Anumudu. I am also grateful to you Fikayo Odunayo for the great companionship we developed. I am equally indebted to RCCG Potters House, Kitchener for emotional support, The Royals for the engagements and fun, the Arisekola family for support and emergency childcare support and Ego Uchendu for encouraging me to aim high.

Most importantly, I am mostly indebted to my wife, Onome Iheanacho for your support, encouragement and patience these many years. You indeed supported our young family in every way and made numerous sacrifices for us. I appreciate your patience and understanding as well, Chiebuka David Iheanacho, for the many times I had to leave even when you wanted me to stay and play with you. To my parents, Hilary and Emelia Iheanacho, my parents-in-laws, Felix and Bernadine Enisire, and my siblings, Emeka, Ada, Ebere and Obinna, thank you all for believing in me and for all your encouragements.

Lastly, I want to thank University of Waterloo Athletics department for the facilities, especially the skating rink. I could not be prouder of my accomplishment in that regard having taking up skating at a relatively old age.

Dedication

Dedicated to Chidiebube Daniel Iheanacho for the very brief moment we shared together

Table of Contents

List of Figures

List of Tables

List of Acronyms

Materials:

a-Si:H: Hydrogenated amorphous silicon
Al: Aluminum
AZO: Aluminum doped zinc oxide
B: Boron
B_2H_6: Diborane
c-Si: Crystalline silicon
Cr: Chrome
GaN: Gallium nitride
Ge: Germanium
GIZO: Gallium indium zinc oxide
H: Hydrogen
HCl: Hydrochloric acid
HgCdTe: Mecury cadmium telluride
HMTA: Hexamethylenetetramine
i: intrinsic (a-Si:H) layer
III-V: Three - five materials
InP: Indium phosphide
ITO: Indium tin oxide
Mo: Molybdenium
n^+: n-type a-Si:H
nip: n-type/intrinsic/p-type junction
NW: Nanowire
p^+: p-type a-Si:H
P: Phosphorus
pin: p-type/intrinsic/n-type junction
Si: Silicon
SiH_4: Silane
SiN_x: Silicon nitride
SiO_x: Silicon oxide
TCO: Transparent conductive oxide
Zn: Zinc
ZnO: Zinc oxide

Tools:

ALD: Atomic Layer Deposition
CVD: Chemical Vapor Deposition
EDX: Energy Dispersive X-ray spectroscopy
FTIR: Fourier Transform Infrared spectroscopy
MBE: Molecular Beam Epitaxy
PECVD: Plasma Enhanced CVD
PVD: Physical Vapor Deposition
SEM: Scanning Electron Microscope
UV-Vis-NIR: Ultraviolet-visible-near infrared spectroscopy

Characterization:

at. %: Atomic percentage
cm: centimeter
EQE: External quantum efficiency
eV: Electron volts
FDTD: Finite difference time domain
I-V: Current - voltage
J: Current density
m: Meters
MHz: Megahertz
mm: Millimeter
nm: Nanometer
rf: Radiofrequency
sccm: Standard cubic centimeter
µm: Micrometer (micron)

Material/Device Parameters:

BCE: Back channel etched
CMOS: Complementary metal oxide semiconductor
LRO: Long range order
ROIC: Read out integrated circuit
SNR: Signal to noise ratio
SOI: Silicon on insulator
SRH: Shockley Reed Hall
SRO: Short range order
TFT: Thin film transistor
VLS: Vapor-solid-liquid

Structure/Morphology:

1-D: One dimensional
2-D: Two dimensional
3-D: Three dimensional
NvF: Nanowire length vs Film thickness

Light:

EM: Electromagnetic
IR: Infrared
LED: Light emitting diode

Chapter 1
Introduction

1.1 Infrared (IR) Detectors

Infrared detectors can be classified into two main application categories – civilian and military – which have both received increased attention lately. The German Federal Ministry of Education and Research Department VDMA statistics predicted that the global market demand for civilian infrared technology will reach $12 billion in 2016 [1]. China's growth rate in this market is expected to reach 20 % by 2020 accounting for over $10 billion in value [1]. In a 2012 market research report, Yole Développement identified three emerging applications of infrared detectors in thermography power tools, automotive and surveillance systems [2]. A 2015 market research report predicted that the infrared market will more than double within the six years between 2014 and 2020 driven in part by newer applications in the civilian market such as in smart buildings and mobile device spot thermometer [3]. A 2016 infrared market research report by Maxtech International stated that uncooled infrared detector shipment increased for a second consecutive year in 2015 by more than 40 % [4].

The appeal for infrared detectors in these emerging applications is driven by three distinct characteristics of infrared signals. First, blackbodies radiate infrared making infrared radiation ubiquitous in the study, understanding and detection of these bodies. Secondly, the long wavelength of infrared radiation enables it to scatter less than visible light in the presence of haze and other atmospheric dimmers. This makes it suitable for applications in military, surveillance, poor vision or adverse weather environments. Also, infrared signals can be used to detect unique signatures of materials and compounds as used in spectroscopy and materials identification. The ability to detect unique signatures is also enabling a new type of application in infrared identification where facial biomarkers and anatomical information involving subsurface features which are unique to each person such as, blood vessels, are imaged [5].

The emerging applications of infrared detectors such as in automotive, smart buildings and motion detectors require detection over large areas. To achieve this, infrared detectors need to be fabricated over large area substrates and at low cost. These applications requires processing on low cost and/or low melting point substrates such as glass and plastic, using processing tools compatible with large-area coverage and low processing temperatures. Another desired property is the ability to integrate such detectors with other electronic devices such as transistors to increase functionality and expand its capability.

Infrared detectors are made up of the detector module and the read out module. The detector module is made of quaternary alloys of III-V materials that provide the capability to engineer a band gap suitable for infrared absorption. The use of these types of materials and the bandgap engineering technique determines the types of substrates and processing techniques that can be applicable. The consequence of this is that the alloying requires relatively complex and expensive processing techniques such as molecular beam epitaxy (MBE) [6], [7] on high-cost substrates such as indium phosphide (InP). At the present, most infrared photodetectors make use of mercury cadmium telluride alloys ($Hg_{1-x}Cd_xTe$) [7], [8]. In addition to the environmental and health implications of these materials, this alloying is also complicated due to the need to appropriately tune the band gap of the ternary alloy and often leads to complicated device geometries [9]. To collect the absorbed photons from the device, a separate read out integrated circuit (ROIC) is needed. In contrast to the detector module, ROIC is made of complementary metal oxide semiconductor (CMOS) technology on a crystalline silicon substrate [10]. The two separate modules are then bonded together using indium interconnects or bumps [10] to form the focal plane array. This procedure adds complexity to the infrared arrays, increases fabrication cost and limits the size of fabricated devices to the size of the starting (InP) substrates. In addition, integration with other electronic devices such as transistors is not seamless but require

bonding using indium bumps which impedes its ability to scale or adapt into large-area panels such as flat-panel technology and displays.

One approach to overcome this limitation is by using amorphous materials such as hydrogenated amorphous silicon (a-Si:H). A-Si:H materials are compatible with large area processing and are not limited by semiconducting substrate sizes. They can be processed on a variety of substrates such as glass or plastic which can be exploited for a variety of applications such as in automotive sensors or people counting applications. Devices based on a-Si:H are larger and cheaper. For example, typical infrared sensors range from 1 × 1 pixel to 80 × 80 pixels and have pixel pitch between 17 μm to 500 μm [3] giving them a pixel density between 43 – 250 pixel per inch (ppi). In contrast flat-panel displays based on a-Si:H materials and processing techniques have arrays of 4000 × 2000 pixels and pixel densities greater than 440 ppi [11]. Estimates from a 2015 Yole Développement report placed a typical infrared pixel at a price of ~ 24.4 cents per pixel. In comparison, flat panel displays using a-Si:H have a price of ~ 0.0013 cents per pixel [12].

Irrespective of the advantages of amorphous materials given above, suitable amorphous materials for infrared detection is still a challenge. Amorphous semiconducting materials used in everyday devices mostly absorb above infrared energies while their absorption within the infrared region is poor. Some of the few materials suitable for infrared absorption have other problems limiting their use. For example, germanium (Ge) with a band gap of ~ 0.8 eV has a high dark current in the range of 1.0×10^{-3} A/cm^2 [13]. This high dark current raises its noise level and leads to a degraded signal to noise ratio. The lack of infrared sensitive amorphous materials suitable for not only infrared detection but also large-area, low cost processing has led to a continued use of size-limited band gap engineered compound semiconductors for infrared detection [7], [8], [14] leading to expensive large-area implementations. To overcome this challenge, infrared absorption has to be improved in amorphous semiconductors.

The poor infrared absorption of amorphous semiconductors such as a-Si:H arise from their low absorption coefficient in the longer wavelength region. With a direct but high band gap, long wavelength absorption is greatly reduced. Increasing the film thicknesses to enable greater infrared absorption often leads to higher recombination due to the high defect states occasioned by their growth process. One approach to increase the film thickness without increasing the associated recombination is to conformally coat such a-Si:H thin film over a network of nanowires creating a 3-D material structure where scattering and multiple reflection can enable increased effective thickness of the coated thin film.

1.2 Large-area (3-D) Infrared Photodetectors

The versatility of a-Si:H for large-area applications has been recognized in the industry from thin-film transistors (TFTs) to solar cells [15]. The ability of a-Si:H to attain this status was largely based on the ability to tune its defect density with hydrogen and change its conductivity by doping [16]. Interestingly also, its optical properties can also be modified. Zhu *et al.* reported an increase in absorption past the mobility edge of a-Si:H nanocones and pyramidal structures [17] while Street *et al.* showed that absorption in only 20 nm a-Si:H material can be increased significantly by changing the surface morphology [18]. The large tail and defect states in a-Si:H then present an important parameter that can be tuned as needed for both electrical and optical gains.

Importantly, a-Si:H can be combined with a network of 1-D structures to create 3-D structures that can extend its absorption beyond planar geometry limits [19]. Through numerical simulations, Tamang *et al.* predicted a doubling of the short circuit current density (J_{sc}) of solar cells fabricated with 3-D structures of a-Si:H film coated on nanowires and showed 80 % increase in effective thickness of the coated film [20]. Pathirane *et al.* experimentally verified 22 % increase in J_{sc} of 3-D solar cells of a-Si:H coated on zinc oxide nanowires (ZnO NWs) over the planar cells due to suppressed reflection

from the 3-D solar cells [19]. The conformal coating of a-Si:H thin films on ZnO NWs to create a 3-D materials system has potential to increase the effective thickness of the a-Si:H thin film and thereby increase its absorption.

Currently, this approach has not been applied for infrared detection. As a result, there is little information to properly understand how a potential infrared absorption can be controlled or optimized. There is then a need to better understand this emerging technique and explore factors that can control any obtainable infrared absorption.

1.3 Integrated IR Sensor-Switch

The growing field of artificial intelligence, robotics and gesture control provide potential applications of infrared detectors. In machine learning for instance, sensors are needed to capture different types of data which will then be processed by algorithms to learn the environment and improve their ability to respond as humans would. Applications in internal temperature measurement of electronic devices to provide on-board diagnostics of the device's power and temperature performance will potentially utilize infrared detection. Also, the field of spot thermometry for mobile devices where infrared sensors are integrated onto mobile devices with other types of sensors and gyroscopes in what is called a sensor hub is promising [3].

In these applications and many more, infrared detection is needed but those detectors are also required to be able to integrate onto the platforms they serve. The inability of current infrared technologies, which is made of 2 separate arrays that are then bonded together, to integrate onto these platforms creates the need for an alternative approach. For example, in touch sensor applications for mobile devices, the touch sensing infrared device will be required to integrate onto the flat panel technology used for displays of mobile devices.

The ability of a-Si:H materials to be easily integrated onto these devices opens the opportunity to create integrated infrared sensing devices. Conceptual design architectures for use in integrated touch sensitive devices have already been proposed [21]–[23]. These architectures can be more readily realized with infrared sensitive a-Si:H materials.

The foregoing shows a growing need to develop infrared sensitivity to a-Si:H based platforms. Enabling such a-Si:H infrared detection platform will provide an alternative low cost material and processing system capable of large-area infrared detection. It will also enable infrared detection on a variety of substrates including plastic and flexible materials.

1.4 Ph.D. Research Goal

The main goal of this research is to develop and understand the optical and electrical characteristics of hybrid 3-D structure for infrared detection. This goal is divided into six distinct themes given below

I. Development of a 3-D material system by synthesizing NWs and conformally coating a-Si:H thin film shells on them

II. Engineering infrared absorption into 3-D materials structure of a-Si:H shell and zinc oxide (ZnO) nanowire (NW) cores

III. Demonstrating and controlling the factors that affect infrared absorption in 3-D ZnO NW/a-Si:H core-shell materials structure

IV. Demonstrating 3-D infrared photoconductors using a-Si:H as absorber material

V. Demonstrating 3-D infrared photodiodes using a-Si:H as absorber material

VI. Proof of concept integration of infrared a-Si:H/ZnO NW hybrid photoconductors onto a-Si:H TFTs for dual functionality of infrared sensing and signal switching.

1.5 Organization of Thesis

The motivation for this thesis has been given in Chapter 1. Chapter 2 provides a brief background on infrared detection. It also includes background discussions on 3-D material systems, processing and devices. Properties of a-Si:H thin films are provided and geometric modeling of the effective length of 3-D coated materials is provided. In Chapter 3, 3-D materials development is presented which includes the growth, characterization and optimization of the disordered NW network. The critical parameters affecting the NW network for optimum 3-D morphology are presented. This chapter also discusses the development of the conformal coating process of the different thin films on the NW network, the deposition conditions and how they affect the coating process. Chapter 4 discusses the optical properties of the hybrid 3-D material structure developed in Chapter 3 with special emphasis on its infrared sensitivity and absorption. The morphology of the 3-D material system and its absorption enhancement are considered. The source of infrared absorption in the 3-D material is systematically studied including the relative contributions from its constituent parts. In Chapter 5, the feasibility of using the developed 3-D material structure for infrared detection is demonstrated with the fabrication of a 3-D infrared photoconductor along with its infrared response and dark current optimizations. Chapter 6 presents the fabrication and development of 3-D infrared photodiodes as another alternative 3-D infrared photodetector. In-depth study of the dark currents of the fabricated 3-D diodes is presented including the various optimizations undertaken to minimize the challenges. A brief comparative analysis of the photodiode and photoconductor is also presented. In Chapter 7, a proof of concept integration of the 3-D photoconductor onto a-Si:H TFTs for a single integrated device structure is demonstrated. The fabrication and electro-optical results are also presented including the effect of design and process variables on the base TFT. Finally, Chapter 8 summarizes the contributions from this thesis and presents some areas for future work.

Chapter 2
Background Review

2.1 Infrared Absorption and Detection

The infrared region is part of the electromagnetic spectrum beyond the visible spectrum and below the microwave portion of the spectrum as shown in Fig 2.1. It spans wavelengths between 750 nm to 1 mm. Their long wavelength enables them to travel farther, longer and less susceptible to scattering by haze and atmosphere, enabling them to be detected in poor lighting or harsh environmental conditions. This property is exploited in night vision and security systems. In addition, infrared radiation is used in many other applications including spectroscopic studies of materials, astronomy, thermal imaging, military and space applications, telecommunication, life sciences and medical diagnostics, household electronics, cooking, signaling and remote controls [7], [10], [24]. Of growing interest is the potential to develop infrared detection on large-areas and integrate them onto existing large-area devices.

Infrared	
Wavelength	1mm – 750nm
Frequencies	0.03 – 4x10^{4}Hz
Energy	0.0012 – 1.65eV

Wavelength(nm)	300	350	400	450	500	550	600	650	700	750	800	850	900
Energy (eV)	4.14	3.55	3.11	2.76	2.49	2.26	2.07	1.91	1.78	1.66	1.55	1.46	1.38

Fig 2.1 Infrared spectrum and energies

To absorb infrared radiation, several techniques could be employed including thermal or photonic techniques. Thermal detection techniques make use of change in temperature of the absorbing material with infrared absorption [9]. Thermal detection techniques are generally independent of the wavelength of incident radiation but rather dependent on the incident power [9] thereby giving them a broad operation range but less specificity. It also limits their use to environments or conditions that enable a measurable temperature gradient.

Photon detectors are made up of semiconducting absorbers which utilize the interaction of absorbed photons with electrons to detect the presence of infrared radiation. Like semiconductor absorbers in general, infrared absorption occurs when incident photon energy is equal to or greater than the band gap of the absorber material. The band gap of the absorber material is the energy difference between the valence and conduction band edges. Absorption of a photon leads to the excitation of a valence band electron to the conduction band where it can be available for current conduction. The relationship between the minimum photon energy (or maximum wavelength) that can be absorbed and the material band gap is given by equation 2.1 where λ_c is the cutoff wavelength, h is Plank's constant, c is the speed of light and E_g is the material band gap.

$$\lambda_c = \frac{hc}{E_g} \qquad 2.1$$

Table 2.1 Photodetector Materials and Detection Range

Material	**Bang gap (eV)**	**Wavelength Range (nm)**	**Gap type**
Crystalline silicon (Si)	1.1	400 – 1050	Indirect
Amorphous silicon (a-Si:H)	1.8	400 – 800	Direct
Germanium (Ge)	0.7	600 – 1600	Indirect
Gallium Arsenide (GaAs)	1.4	650 – 870	Direct
Indium Gallium Arsenide (InGaAs)	0.7	900 – 1700	Direct
Indium Gallium Arsenide Phosphide (InGaAsP)	0.7 – 1.4	800 - 1650	Direct or Indirect

Equation 2.1 places a limit on the suitability of several materials for infrared absorption. For example, a-Si:H is widely used for large-area applications in image sensor arrays and flat panel displays. Due to its large band gap, its ability to absorb long wavelength is limited. Table 2.1 shows some band properties of some common semiconductor materials. The deficiency in semiconductor materials that can absorb infrared radiation has led research into engineering alternative schemes to absorb and detect

infrared. For example, bang gap engineered III-V semiconductors could be employed to tune the material band gap suitable for infrared absorption. This technique however relies on expensive InP substrates [6] which increases fabrication cost, complexity and limits the detector sizes to the starting substrate size.

Other techniques that have been proposed to overcome this limitation include mid-bandgap absorption (MBA), two-photon absorption (TPA) [25], excitation of local plasmons [26] and intersubband absorption.

Mid-bandgap absorption (MBA) uses an intermediate state to breakdown or reduce the bandgap of the absorber into small energies that are cumulatively equal to the band gap. In the developing field of intermediate band solar cells [27], [28], intermediate bands are introduced in the band gap of the absorber to enable a 2-step absorption as shown in Fig 2.2a thereby enabling the absorption of photon energies below the material's intrinsic band gap. For infrared applications, highly supersaturated chalcogen doped silicon commonly referred to as black silicon have been used to extend the absorption cutoff wavelength of Si beyond 1050nm [6], [29]–[34]. Recently, ion implantation using Zn atoms has been reported [35]. These materials rely on crystalline silicon substrate which leads to size-limitations and increased cost.

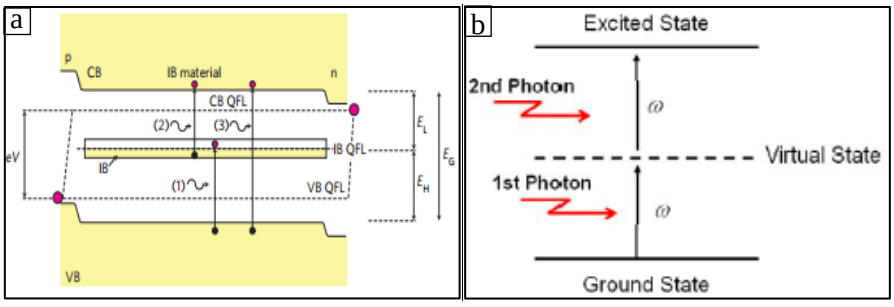

Fig 2.2 Schematic showing (a) 2-step absorption of intermediate band solar cells [27]**; (b) Two – photon absorption** [25]

In two-photon absorption (TPA), an electron absorbs two photons simultaneously and is then excited to an energy level corresponding to the sum of the incident photons (Fig 2.2b) [25]. This process requires no intermediate state but a virtual state which does not correspond to any electronic state. Simulations by Siampour and Dan showed that the realization of infrared absorption using this technique requires a complex light confinement system [36]. Such confinement system could be realized with SiNWs grown on silicon on insulator (SOI) substrates which limits its size and increases its fabrication cost.

Surface plasmons are localized electromagnetic oscillations at the metal-dielectric interface which have exponentially decreasing amplitudes, lower energy than bulk and opposing sign of the real part of their respective relative permittivity [37]. Surface plasmons have also been used to extend absorption beyond the bandgap cutoff wavelength [26], [38], [39]. Intersubband absorption makes use of transitions between quantized levels within a band often provided by quantization using a quantum well. Because these transitions have very low energies, they are sometimes integrated with a LED to form upconversion devices [40].

These techniques all attempt to increase long wavelength absorption or extend visible absorption beyond the band gap. They mostly make use of expensive processing, complex device structures and size-limited substrates. However, to absorb infrared over large areas, new material engineering approaches needs to be explored.

A-Si:H for example, is capable of large area processing and has been shown to be compatible with silicon based applications in flat panel displays [41]. Engineering infrared absorption into a-Si:H materials therefore have potential to enable large area infrared detection devices which would be capable of integration onto existing flat panel technology and onto a wide array of substrates.

2.2 Three Dimensional (3-D) Materials System and Processing

Three dimensional (3-D) materials system is most commonly used to describe materials with 3-D morphology. These include pyramidal structures, cones [17] or hybrid integration of a network of 1-D materials such as nanowires (NWs) and 2-D materials such as thin films [19], [20], [26], [42]–[46]. The morphology of 3-D materials enables light confinement within the material system due to internal multiple reflection leading to reduced total reflection from the material as shown in Fig 2.3. The strong light trapping and reduced reflectivity of 3-D materials have the potential of increasing its effective thickness beyond the nominal value due to increased light – matter interaction leading to increase in its absorption. The effectively thicker material could then extend the absorption of the material beyond its normal wavelength.

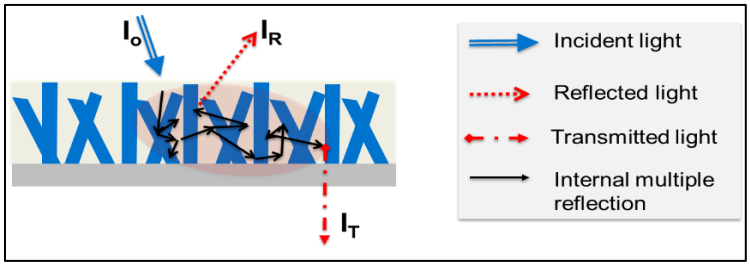

Fig 2.3 Schematic illustration of a 3-D Material System showing internal multiple reflection

Exploiting such property of 3-D materials is of great interest to push photon absorption beyond traditional limits. For example, Huang *et al.* showed that the ultimate efficiencies of solar cells fabricated with such 3-D materials will exceed those of their 2-D counterparts in all six materials they studied [46]. Tamang *et al.* showed that the short circuit current density (J_{sc}) of a-Si:H solar cells could double by the introduction of NWs which would transform it to a 3-D material [20] and Pathirane *et al.* showed a 22 % increase in J_{sc} of such 3-D solar cells compared to planar ones [19]. These enhancements were a result of their increased absorption which was attributed to scattering and multiple reflection

[18] leading to reduced reflectivity [19], [45], [46], strong light trapping and antireflection properties [17].

2.2.1 Light Absorption in 3-D Materials

The appeal of 3-D materials system is its ability to enhance optical absorption. From a classical perspective, Beer Lambert's law describes the attenuation of light intensity propagating through a medium. This attenuation, which is dependent on its extinction coefficient, represents the absorption of the propagating radiation by the material.

$$I(t) = I_0 e^{-\alpha t} \qquad 2.2$$

Beer Lambert's law given in equation 2.2, where *I(t)* is intensity at a depth *t* propagating through a material of absorption coefficient α with an initial incident intensity of I_0, indicates that the absorbing material could absorb more radiation if its thickness is increased. This requirement presents a practical limitation. The thicker films get, the greater their intrinsic stress and reflectivity which degrades their optical properties. Thicker films also require long deposition times which limits their practical thicknesses. In addition, as films get thicker, the distance between electrical contacts increases thus increasing the distance photo-generated carriers need to travel before collection and also increasing the scattering they will experience. This thicker film leads to higher recombination losses due to shorter carrier diffusion lengths and bigger transport distances in amorphous semiconductors. However, the discussion in Section 2.2 above shows that using a 3-D morphology could increase the effective thickness of coated films such that their reflectivity is suppressed and absorption enhanced.

Fig 2.4 shows a schematic illustration of the 3-D network of a-Si:H coated ZnO NWs. The 3-D network is made up of a ZnO NW core and a-Si:H shell. Predicting the effective thickness of such 3-D materials system using Beer Lambert's law as given in equation 2.2, requires that the absorption coefficient of the absorbing material is known. However, absorption coefficient is a function of

wavelength which would imply the effective thickness of the 3-D material varies with wavelength. More so, for a-Si:H materials, absorption coefficient decreases with increase in wavelength and information regarding absorption coefficient at infrared wavelengths is lacking. Since light-matter interactions are governed by Maxwell's equations, the solution to these equations would provide a better guide to the absorption of 3-D materials systems.

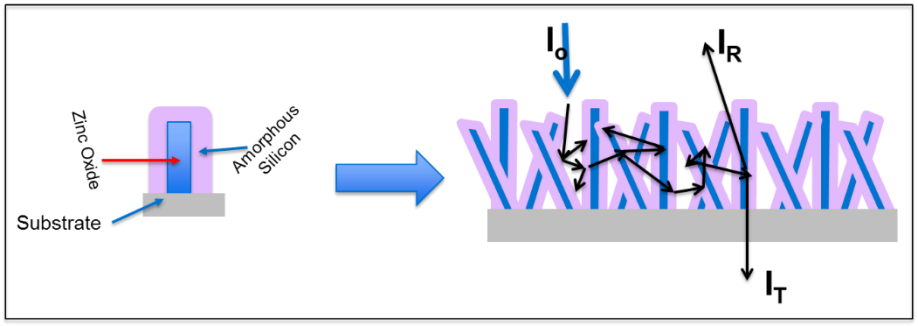

Fig 2.4 Schematic illustration of a 3-D system of a-Si:H coated ZnO NWs

By using finite difference time domain (FDTD) to rigorously solve Maxwell's equations in 3-D, the interaction of light with the 3-D core-shell structure can be mapped [20] and can be approximated by equation 2.3 where t_{eff} is the effective thickness, h is the NW height (length), d is the NW diameter, t is the nominal a-Si:H thickness, and p is the pitch or NW separation which is related to the NW density [20].

$$t_{eff} = \left(1 + \frac{\pi \times h(d+t)}{p^2}\right) \times t \qquad 2.3$$

While the effective thickness here was derived for an ordered NW network, it is a good approximation to evaluate the structure and optical properties of disordered 3-D core-shell structures. Numerical simulation of a 3-D structured solar cell shown in Fig 2.5a show a doubling of the J_{sc} and 80 % increase in optical thickness (effective thickness) of 100 nm absorber layer with the addition of 400 nm long NWs spaced at 600 nm apart [20]. The increased effective thickness causes an increase in

optical absorption that is then translated to increased J_{sc}. Quantum efficiency simulations confirmed this effect and show an increase in red absorption as the NW heights increase (Fig 2.5b).

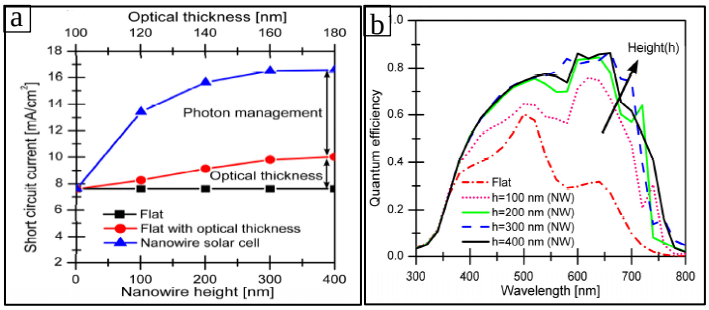

Fig 2.5 Increase in (a) J_{sc} and optical thickness (effective thickness) and (b) EQE of a simulated 3-D solar cell showing higher red spectrum absorption [20]

Equation 2.3 predicts, as shown in Fig 2.6a, that for 500 nm a-Si:H shell coated on 5 µm ZnO NWs, the effective shell thickness increases by about 3 orders of magnitude to 1.14×10^5 nm as the NW density is increased to 6.4×10^9 NW/cm^2. The same trend follows with a-Si:H thicknesses of 250 nm or 1000 nm. Similarly, for a uniform NW density and length, effective thickness of a-Si:H shell increases as the thickness of the coated shell increases (Fig 2.6b). With a uniform NW density and a-Si:H shell thickness, effective thickness of the a-Si:H shell increases as the length of the NWs increases also (Fig 2.6c). This increase however is more weighted towards higher NW densities increasing by almost 2 orders of magnitude for 1.0×10^9 NWs/cm^2 and 500 nm thick a-Si:H coated on the 10 µm NWs (Fig 2.6c). These enhancements strongly indicate that with 3-D material system, more absorption can be expected.

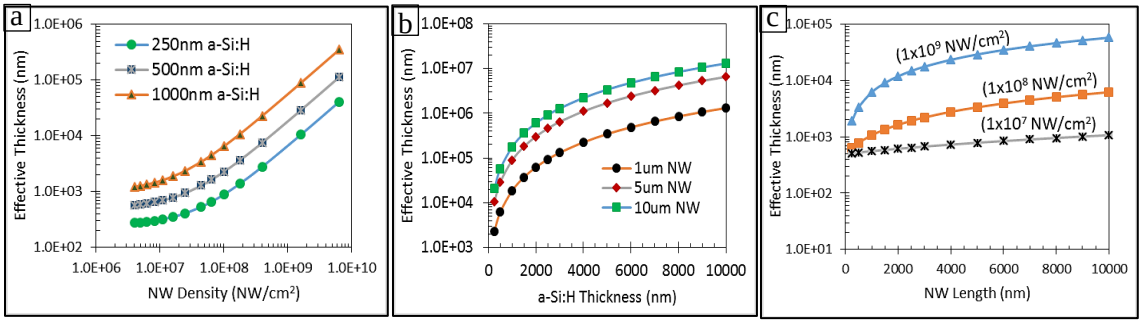

Fig 2.6 (a) Predicted effective thickness enhancement of a 3-D material with (a) increasing NW density for 250nm, 500nm and 1000nm a-Si:H shell coated on 5µm ZnO NW; (b) increasing a-Si:H thickness for 1µm, 5µm, and 10µm NWs and 1.0 × 10^9 NW/cm^2 NW density; and (c) increasing NW density to 1.0 × 10^7, 1.0 × 10^8 and 1.0 × 10^9 NW/cm^2 and of 500nm a-Si:H shell

2.2.2 3-D Structure Processing

Several approaches have been used to synthesize amorphous semiconductor based 3-D structures with different levels of complication and processing challenges. In one approach, a thick film of a-Si:H was first deposited on a substrate followed by self-assembly of silica nanoparticles on the a-Si:H surface. The a-Si:H film was then etched by reactive ion etching to create nanowires and nanocones using the silica nanoparticles as a mask [17]. Etching back a film or substrate to form the 3-D structure is relatively easy but practically limiting. This method first requires the deposition of the thin film up to desired thickness before the etch back. The requirement to first deposit the thin film limits the length of 3-D nanostructures that could be obtained making it less practical for high volume applications or applications that require high aspect ratios.

In another approach, nanoimprint lithography was used to make silicon oxide patterns over which thin films were deposited [47]. With this technique, a conformal recipe for the subsequent thin films will be required. In addition, the use of a stamp limits the ability to align multiple layers for device fabrication and limits the size that can be obtained to the size of the stamp.

A third approach involves conformally coating thin films such as a-Si:H on nanowires such as ZnO NWs in a core-shell structure [19]. This technique provides high aspect ratio structures with increasing length of the nanowires. In addition, the density of nanowires and thickness of the a-Si:H coating can be used to modify the properties of the 3-D material. This approach also requires that a conformal coating recipe for the thin film be developed. Such coating recipe should be able to coat the sidewalls of the NW network and preserve the distinct 3-D morphology. In general, conformally coating a network of NWs is a very viable method for synthesizing 3-D materials and may be easily manipulated for desired results.

2.2.3 ZnO Nanowire Synthesis

Nanowires (NWs) as 1-D structures have grown in popularity in recent times of which metallic, semiconducting, or insulating NWs have been realized. They can be synthesized from elemental semiconductors such as silicon (Si) [18] and germanium (Ge) [48] or from compound semiconductors such as zinc oxide (ZnO) [19] and gallium nitride (GaN) [49]. The size and aspect ratios of NWs can enable other types of functionalities which will otherwise not be feasible in the bulk material.

NW syntheses are generally classified into top-down and bottom-up approaches. In top-down approaches, the NWs are derived from the bulk material by removing surrounding bulk materials while in bottom-up approaches, the NWs are assembled from their basic building blocks. The choice of a NW synthesis method generally depends on the material to be grown, the substrate, allowable growth conditions such as temperature requirements and expected properties of the NWs. Among the bottom up approaches, the vapor-liquid-solid (VLS) technique and the hydrothermal technique are popularly used.

The VLS technique typically involves using a catalyst, usually formed by sputtering 2-5 nm thick metal such as gold or copper and annealing to form droplets, to seed the growth of nanowires from the

source gas at high temperatures (> 800°C). The VLS process involves three stages [50]. The first stage called the alloying process, involves the alloying of the catalyst and source gas leading to an increase in the volume of the catalyst alloy droplet; the second stage, the nucleation stage, involves the nucleation of the nanowire from the catalyst alloy above a saturation threshold while the third stage, the axial growth stage, involves the axial growth of the nanowire following further dissolution of the source gas into the catalyst alloy [50]. VLS technique is popularly used to grow Si NWs [51] and Ge NWs [50] but has also been used to grow ZnO NWs [52]. The use of a catalyst with the VLS technique introduces impurities that could propagate through the nanowire. It also requires high temperatures which limits its application to high temperature substrates that are normally size limited.

In addition to the VLS technique, hydrothermal synthesis is also popularly used to grow ZnO NWs. Hydrothermal synthesis of nanostructures is the thermal synthesis of nanostructured materials from solutions containing their salts. It is most commonly used to synthesize transition metal oxides such as ZnO NWs [53] and iron oxide nanocubes [54]. It is a low-cost technique with a low-processing temperature that can enable the use of several substrates such as silicon, glass or plastic.

Hydrothermal synthesis of ZnO nanostructures involves the thermal decomposition of zinc (Zn) containing salts in solutions. One approach involves the thermal decomposition of zinc nitrate hexahydrate ($Zn(NO_3)_2{\cdot}6H_2O$) in the presence of hexamethylenetetramine (HMTA) ($C_6H_{12}N_4$). However in the last few years, several implementations of this technique have been reported. Table 2.2 summarizes some of these implementations.

The $Zn(NO_3)_2{\cdot}6H_2O$ acts primarily as the source of Zn^{2+} ions while HMTA acts like a pH buffer and provides a slow and controlled supply of hydroxyl ions [55]. The thermal decomposition of HMTA into formaldehyde and ammonia regulates the pH of the solution [56]. Ashfold *et al.*, reported that the concentration of both Zn^{2+} and HMTA rapidly decreased in the first 2 hours of hydrothermal growth.

After the first 2 hours however, the concentration of Zn^{2+} linearly decreased with time while that of HMTA remained relatively constant and independent of ZnO precipitation [57]. The precipitation of ZnO from the solution could occur directly from the Zn^{2+} ions or through the hydroxide as given below [57].

$$C_6H_{12}N_4 + 10H_2O \rightleftharpoons 6CH_2O + 4NH_4^+ + OH^- \quad 2.4$$

$$Zn^{2+} + 2OH^- \rightleftharpoons ZnO + H_2O \quad 2.5$$

$$Zn^{2+} + 2OH^- \rightleftharpoons Zn(OH)_2 \rightleftharpoons ZnO + H_2O \quad 2.6$$

Table 2.2: Implementations of Hydrothermal Depositions of ZnO Nanoparticles

Reference	**Precursors**	**Nanostructure**
[57]	Zinc nitrate hexahydrate ($Zn(NO_3)_2{\cdot}6H_2O$) + Hexamethylenetetramine (HMTA) ($C_6H_{12}N_4$)	Nanowires, nanorods, nanotubes
[58]	Zinc acetate dehydrate ($Zn(Ac)_2{\cdot}2H_2O$) + TMAH ($(CH_3)_4NOH$)	Nanowires
[59]	Zinc chloride ($ZnCl_2$) + Sodium hydroxide (NaOH)	Nanowires, powders
[60]	Zinc nitrate hexahydrate ($Zn(NO_3)_2{\cdot}6H_2O$) + Hydrazine hydrate ($N_2H_4{\cdot}H_2O$) + Potassium Iodide (KI)	Nanowires, nanorods
[61]	Zinc acetate dehydrate ($Zn(Ac)_2{\cdot}2H_2O$) + cetyltrimethyl ammonium bromide (CTAB) ($C_{19}H_{42}BrN$)	Nanocrystals clusters
[62]	Zinc acetyltacetone ($Zn(acac)_2{\cdot}H_2O$)	Nanorods
[63]	Zinc tetraoxosulphate (VI) ($ZnSO_4$) + Carbamide ($CO(NH_2)_2$) + ethanol (C_2H_5OH) + Sodium hydroxide (NaOH)	Nanobelts
[64]	Zinc foil (Zn) + ammonium hydroxide (NH_4OH)	Nanorods

According to Xu and Gao [65], the relationship between the seed crystal size and its solubility in a hydrothermal growth process can best be understood using the Ostwald-Freundlich equation given in equation 2.7 where *c(r)* is solubility of small crystals of radius *r*, c_0 is the solubility of the bulk crystal,

Ω is the molecular volume, γ is the surface free energy, k_B is the Boltzmann constant and T is the temperature.

$$In\left[\frac{c(r)}{c_0}\right] = \frac{\gamma\Omega}{rk_BT} \quad 2.7$$

According to the Ostwald-Freundlich relationship, below a critical size, solubility is inversely proportional to crystal size and by extension, the supersaturation of a seed crystal is proportional to its size. Thus, larger sized seeds will have higher supersaturation around them than smaller sized seed crystals [65]. Hydrothermal synthesis is also sensitive to growth parameters such as solvent composition [66], temperature [67] and seed layer [68]. These parameters affect the surface free energy, molecular volume, crystal radius and temperature of the growth system thereby leading to observable changes.

2.2.4 Hydrogenated Amorphous Silicon (a-Si:H)

Hydrogenated amorphous silicon (a-Si:H) is a disordered form of Si that has been used in large-area electronics [16], [69], [70] and a wide variety of devices including position sensors, TFTs, active matrix liquid crystal displays, image sensor arrays and solar cells [15]. It can be deposited over a large-area and can also be processed at low temperatures. The later feature has enabled its use on flexible substrates with low melting points [19], [71].

A-Si:H is usually grown by chemical vapor deposition (CVD). CVD systems are a type of thin film deposition system that are based on the chemical assembly of a growing material from a vapor containing its reactive radicals. There are several variants of CVD systems that generally are products of the methods through which the reactive radicals are produced. The Plasma Enhanced CVD (PECVD) process for example uses a plasma technique to enhance the formation of these radicals from their

precursor gases while Hot Wire CVD (HWCVD) uses a hot wire or filament to decompose the precursor gases and generate these radicals.

PECVD has grown in popularity and has been used in research and industry scale production to grow various thin films. The unique feature of a PECVD is its ability to grow thin films at low temperatures (100 – 300°C) due to the plasma assisted decomposition of the precursor gases. In a conventional CVD system, temperatures ~ 600°C would be required to decompose the precursor gases. A-Si:H films grown by PECVD involves the plasma assisted decomposition of silane (SiH_4) gas molecules into radicals such as H, SiH, SiH_2, SiH_3, S_2H_5, and/or S_2H_6 [72]. The radicals then proceed to the growing surface where they attach and form the thin film. Of the possible radicals obtainable from SiH_4 dissociation, SiH_3 is considered the most stable and contribute to growth of acceptable quality a-Si:H film [16], [72].

The surface reactions involved in the growth of a-Si:H films include Si precursor attachment (or adsorption of molecular fragments onto the growing surface) and the release of hydrogen atoms (or molecules) from the surface [16], [72]. Adsorption of SiH_3 radicals are only successful at Si dangling bonds. For H passivated bonds, surface H removal is necessary for film growth [16], [72]. Fig 2.7 illustrates the possible surface processes involved in the growth of a-Si:H film [16].

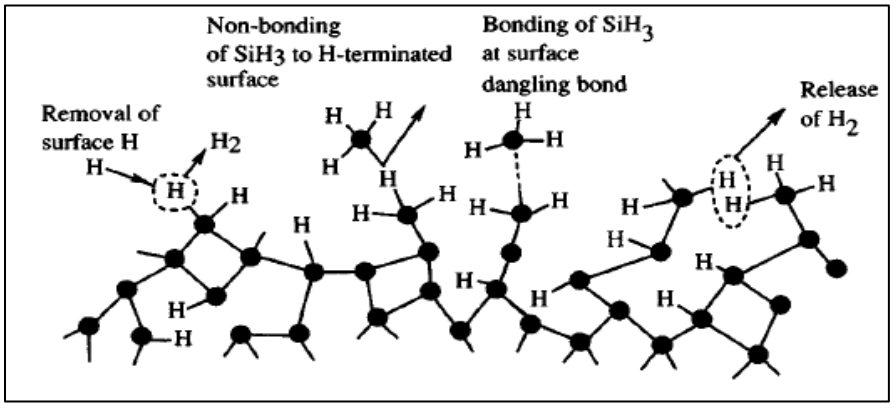

Fig 2.7 Illustration of possible surface processes involved in the growth of a-Si:H film [16]

Unlike crystalline silicon (c-Si), a-Si:H, like most amorphous materials, do not have a regular repeating crystal structure. Most features of a-Si:H matrix are defined during growth and therefore depend on the deposition process [16]. The quality of a-Si:H thin film is modulated by process parameters such as rf power, process pressure, process temperature and precursor gases. These process parameters affect growth factors such as SiH_4 dissolution rate, mean free path of radicals and surface energy of the growing surface. For example, the defect density of a-Si:H can be reduced by several orders of magnitude by passivating with hydrogen during growth. Similarly, the conductivity of a-Si:H can be increased by doping with boron or phosphorus precursor gases [16], [73].

As seen above, a-Si:H growth involves the attachment or self-assembly of H bonded Si radicals. This packing is not efficient and does not lead to long range order of regularly repeating crystal units, hence its amorphous nature. Distortions in the bond angle, length and configuration can exist in the matrix. Another consequence of this growth method is the presence of several instances of unterminated Si bonds, called dangling bonds. While a-Si:H growth is tuned to preferentially growth from SiH_3 radicals, the incorporation of other forms of radicals from the SiH_4 decomposition will lead to incorporation of Si atoms with varying amounts of H termination or dangling bonds.

Despite the absence of a long range order of repeating crystal units, a-Si:H has short range order. The short range order implies the bond angle and bond length are ordered within one interatomic distance, and determines its band structure. Fig 2.8 illustrates a typical crystalline matrix with its long range order of repeating crystal units and a disordered a-Si:H matrix lacking such regular repeating crystal units.

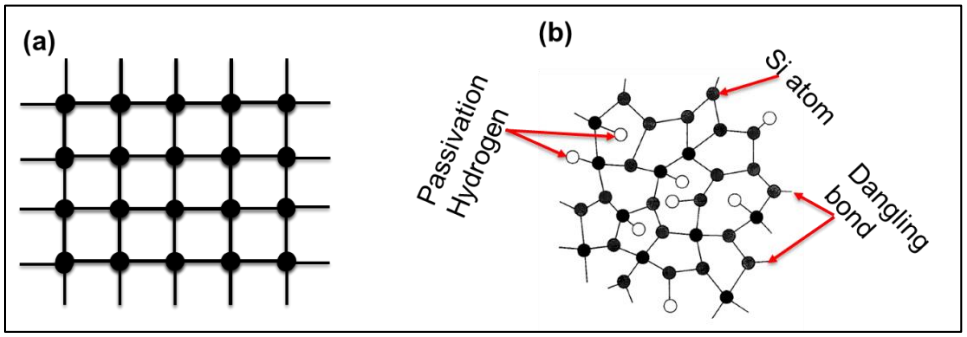

Fig 2.8 (a) Illustration of a crystalline matrix with a long range periodic crystal order; (b) Disordered a-Si:H matrix showing distortions in bond length and bond angles

The disordered nature of a-Si:H is a consequence of its growth method and has great implications for its electronic properties. Fig 2.9a shows the correlation between structural defects in a-Si:H matrix and resulting electronic properties while Fig 2.9b shows the resultant density of states. The consequence of its lack of long range order and disordered nature is the presence of a large concentration of defect states in its band gap and the presence of band tail states. Depending on the specific growth method used, these defect states can also vary. For example, a-Si:H materials grown from evaporation can have defects in the range of ~ 3×10^{18} cm^{-3} while defects are in the range of ~ 1×10^{16} cm^{-3} for PECVD a-Si:H films [74].

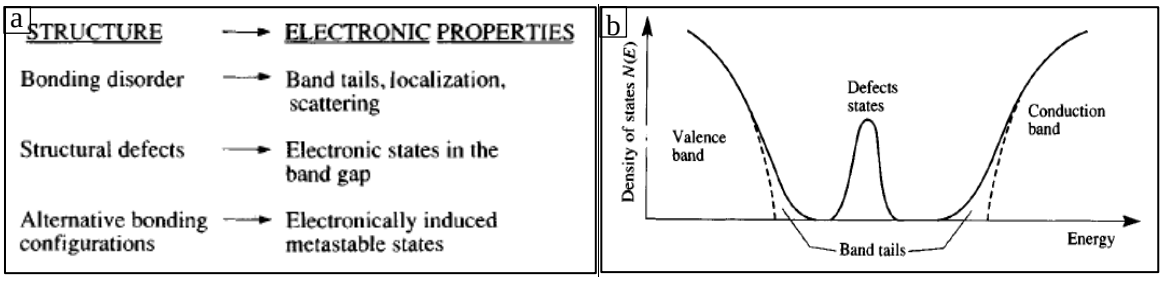

Fig 2.9 (a) Correlation between structural defects and electronic properties of a-Si:H [16]**; (b) Density of states of a-Si:H material** [16]

These defects can however be controlled by passivating the dangling bonds with hydrogen (H) [16], [72], [73]. This passivation will lead to changes in material properties such as improved

photoconductivity [74], film stress [74] and better devices [75]. In general, low-defect density a-Si:H material are desirable in devices such as solar cells, TFTs and photodiodes, because defects in a-Si:H can act like trap centers which could increase carrier recombination. For example, in a TFT, defects within the a-Si:H channel layer could lead to threshold voltage shifts and slow recovery when bias stability stress measurements are carried out. Similarly, defects in a solar cell absorber layer could lead to shorter diffusion length where photo-generated charge carriers are not easily collected at the contacts because they are trapped in these defect sites.

The H passivation for a-Si:H thin film is usually *in situ* supplied by the precursor gases of SiH_4 or mixture of SiH_4 and H_2, and serves to terminate some of the dangling bonds. By varying the H dilution, the defect concentration of a-Si:H could be changed by several orders of magnitude [16]. The effectiveness of H passivation during growth also depends on other growth factors such as temperature, rf power and gas concentration [16], [72]. For example, Street *et al.* showed change in defect concentration of different a-Si:H films by varying the growth temperature [76]. The effect of temperature and rf power on H passivation of a-Si:H films is summarized in Fig 2.10 [16]. *Ex situ* passivation using techniques such as plasma enhanced hydrogenation and forming gas anneal also exist. These generally depend on the hydrogen content of the starting a-Si:H material. PECVD deposited a-Si:H material contain between 10 – 40 at. % of H while Low Pressure CVD (LPCVD) deposited a-Si:H materials usually contain much less H at ~ 5 at. %. Sputtered or evaporated a-Si:H material contain H ranging from < 1 at. % to around 3 at. %. Using a starting a-Si:H material with a relatively high hydrogen content, *ex situ* hydrogenation techniques are less effective compared to H deficient a-Si:H. In addition, *ex situ* hydrogenation techniques are diffusion dependent and diffusion rate is limited by the trap density of the a-Si:H material. Table 2.3 shows the summary of the properties of a typical high quality a-Si:H film [72].

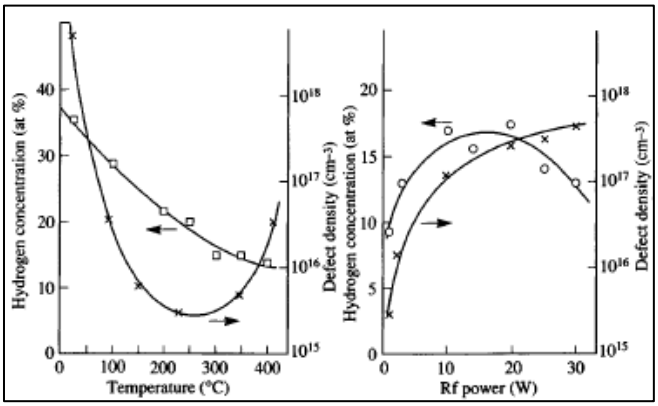

Fig 2.10 Effect of temperature and rf power on H passivation and defect density

Table 2.3 Properties of typical high quality a-Si:H films [72]

Bulk Hydrogen Content (C_H)	15 – 25 at. %
Bandgap (E_G)	1.7 – 1.8 eV
Density of States in the bandgap (DOS) (Annealed)	2 x 10^{15} cm^{-3}
Photo – to – dark conductivity ratio (σ_p/σ_d)	~ 10^5 - 10^6
Electron mobility-lifetime product $(\mu\tau)_{electron}$	4 x 10^{-7} cm^2/V
Hole mobility-lifetime product $(\mu\tau)_{hole}$	~ 10^{-8} cm^2/V

As stated earlier, addition of dopant gases during a-Si:H growth can lead to the incorporation of dopants and therefore increase in the conductivity of the resultant film. However, in the continuous random network of a-Si:H film, the concept of defects as vacancies or interstitials are not valid, rather, coordination defects are used to describe an atom with fewer or more bonds than its valency suggests [73]. The incorporation of dopants such as B or P thus leads to the creation of coordination defects. To preserve charge neutrality, compensating defects are created within the band gap, a consequence of the modified 8 – N rule [77].

Characterizing the defect concentration of a-Si:H material may be accomplished through Fourier Transform Infrared (FTIR) spectroscopy. FTIR measures atomic vibrations at the bonds that can be used to map the materials bonding configuration. With the appropriate constants, FTIR can give quantitative values of hydrogen content in the a-Si:H film. It can also be used in a comparative mode where the film quality is measured relative to a control sample. For a-Si:H materials, FTIR peaks at 2000 cm^{-1} correspond to Si-H bond while the peak at 2100 cm^{-1} corresponds to defective bonds of SiH_2, clusters of SiH_2 and other $SiH_{2+n(n\geq 0)}$ bond forms. Thus, the ratio of the 2000 cm^{-1}/2100 cm^{-1} peaks, known as the film microstructure parameter, represents the quality of the film where higher ratios are indicative of high film quality while low ratio indicates a defective film. This ratio can be obtained by de-convoluting the FTIR peak around 2000 cm^{-1} into its 2000 cm^{-1} and 2100 cm^{-1} components.

The disorder in a-Si:H matrix leads to scattering which causes its wavefunction to loose coherence, hence loss of conservation in its momentum. The loss of conservation of its momentum quantum number gives it a direct band gap of ~ 1.8 eV. This leads to a high absorption coefficient but also limits its use in absorbing long wavelength radiation. Even though increasing its thickness will lead to more absorption, the low carrier diffusion length unfortunately limits the ability to collect those photo-generated carriers thus limiting its practical thickness to below ~ 2 μm in photodiodes and ~ 300 nm in solar cells. Efforts to overcome this limitation has generated interests in its integration with 1-D nanostructure to form 3-D materials [19] where scattering within the 1-D nanostructures during interaction with light could lead to an increase in its effective thickness, beyond its nominal coating thickness.

2.3 Optoelectronic and Switching Devices

2.3.1 Photodetectors

Photodetectors are devices that detect or measure photons by absorbing incident light and generating excess carriers in the semiconductor. The excess carriers generated are then converted into a measurable quantity which could be in form of current or voltage difference. Photodetectors have found applications in spectroscopy and characterization, range finders, motion detectors and position sensors, instrumentation and medical imaging, photography and optical communication, among others.

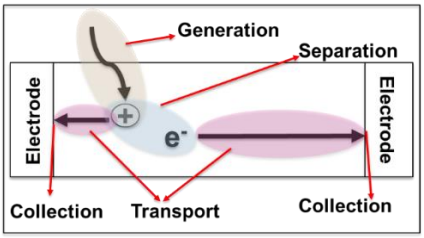

Fig 2.11 Photo-detection process

Semiconductor detectors (or photon detectors) work by internal photoelectric effect. This photoelectric effect is such that photo-generated or photo-excited carriers remain within the material. The processes involved from incident photon to read out can be summarized as shown in Fig 2.11. The incident photon is absorbed and electron – hole pairs are generated. The electron – hole pairs (also called excitons) are thereafter separated. This process is very fast in inorganic semiconductors due to its weak exciton binding energy and is often omitted. The generated (and separated) charge carriers are transported to the electrodes for collection and the collected carriers are sometimes amplified for read out. Photodetectors could be photodiodes or photoconductors and could be made from different materials. These materials generally have a detection range determined by their bandgap as given in Table 2.1. By changing the material or its optical properties such as can be realized using 3-D structures, photodetectors can be tuned to detect different aspects of the EM spectrum such as infrared.

2.3.2 Photoconductors

Photoconductors are a type of photodetectors that are based on the photoconductivity of the absorbing material. Photoconductivity refers to any phenomena by which a change in conductivity follows absorption of light [25]. Photoconductors are current injection devices where exposure to radiation leads to changes in the materials' resistance. These changes in resistance then cause changes in current or voltage. Detection mechanism is based on the measurement of such voltage or current changes in the output which can then be correlated to the incident radiation.

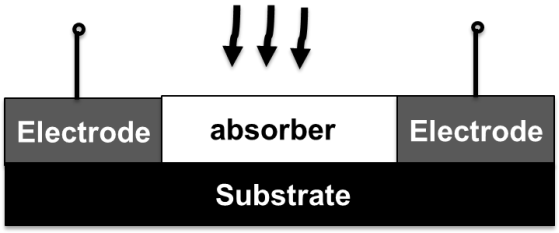

Fig 2.12 Schematic structure of a photoconductor

The structure of a typical photoconductor is shown in Fig 2.12. In photoconductors, only one type of charge carrier is involved. The carrier circulates under the influence of electric field through the device and in the external circuit. ON/OFF ratio, defined as the ratio between photo-generated current and dark current as given by equation 2.8, depends on the dark conductivity of the material. The longer length of the device between both contacts extends the distance that photo generated carriers need to travel, thus making the device switching slower than photodiodes. However, its simplicity makes it easy to realize and also makes it easy to tune across a wide range of operation. By replacing the absorber layer with 3-D materials system, photoconductors that are sensitive to long wavelength radiation could be realized.

$$\frac{ON}{OFF} = \frac{I_{ph}}{I_{dark}} \qquad 2.8$$

2.3.3 Photodiodes

Photodiodes are another form of photodetectors. For a-Si:H thin films, the photodiode is typically a light sensitive *p-i-n* diode as shown in Fig 2.13. Incident photons of sufficient energy are absorbed at the depletion region of the diode thereby generating excess carriers. The photo-generated carriers are then swept out of the depletion region by the built-in or externally applied electric field to generate a photocurrent. As a photodetector, the photodiode is operated in reverse biased mode. This is such that the depletion region can be expanded and the junction capacitance reduced.

Carrier conduction in a photodiode is by both electrons and holes. Here, both drift and diffusion transport mechanisms are employed. Within the depletion region, generated carriers are swept away by drift due to the built-in or applied electric field. Outside the depletion region, carrier transport is by diffusion. The length of the un-depleted region in this case then becomes an important parameter in determining the speed of the device.

In a *p-i-n* photodiode, the depletion region extends across the length (thickness) of the intrinsic (*i*) region as shown in Fig 2.13. The thickness of the intrinsic region hence determines the amount of photons that can be absorbed. Its bandgap also determines the wavelength that can be absorbed. The doped layers that sandwich the intrinsic layer provide rectifying contacts [15]. They do not contribute to light sensitivity and are thus made very thin [16] in order to minimize parasitic light absorption.

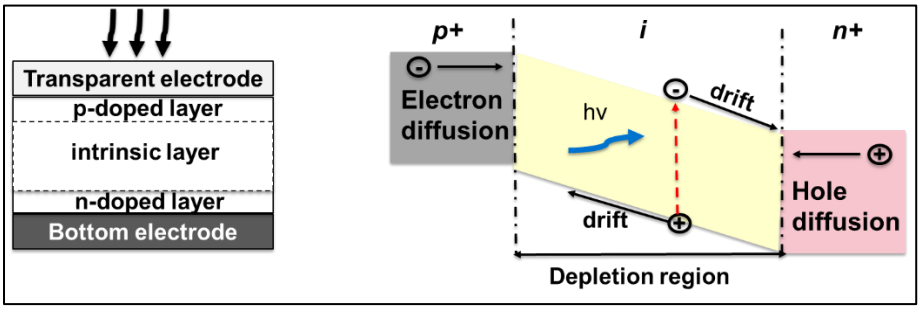

Fig 2.13 Schematic illustration of a *pin* photodiode structure and operation

The photodiode in forward bias can be described by the ideal diode equation given in equation 2.9 where J_0 is the saturation current density, V is the applied voltage, q is the electronic charge, kT is the thermal energy and n is the ideality factor, a measure of how ideal the diode is to an ideal diode.

$$J = J_0 \exp(\frac{qV}{nkT}) \quad 2.9$$

In reverse bias, no current is expected to flow. Even with no incident photon, a small amount of current can still be measured from a reverse biased photodiode. This current is called leakage or dark current and has components from the bulk, doped contacts or device edges [15]. In optimized devices, leakage current is dominated by thermally generated bulk current via mid gap states as given by equation 2.10 [77] where J_{th} is thermal current density, e is the electronic charge, $N(E_F)$ is the density of states at the Fermi Level, kT is the thermal energy, d is the intrinsic layer thickness and τ is the carrier relaxation time.

$$J_{th} = eN(E_F)kT(\frac{d}{\tau}) \quad 2.10$$

Leakage current has an important implication as it determines to a great extent, the photodiode's signal to noise ratio (SNR or ON/OFF ratio). The ON/OFF ratio, given in equation 2.8, determines how well a photodiode effectively detects incident radiation. A high dark current will reduce the signal to noise ratio of the photodiode by reducing the difference between the illuminated current and the non-illuminated case. Typically, photodiodes exhibit very low dark currents in the range of 10^{-10} – 10^{-12} A/cm^2 [15]. Under a reverse bias, flow of charge carriers in a photodiode is suppressed. This suppression of charge carriers give photodiodes the ability to have low dark currents which could be lower than the materials' intrinsic resistance and make them preferable to photoconductors for detector applications. The low dark currents then make them suitable for applications in image sensors [78] and other types of detectors.

The thickness and bandgap of the intrinsic layer of a *p-i-n* diode determines the wavelength of operation of the photodiode. Increasing the intrinsic layer thickness hence is expected to increase its absorption according to Beer Lambert's law given in equation 2.2 and lead to longer wavelength operation. However, as the thickness of the photodiode is increased, the distance required for photo-generated carriers to travel also increases, leading to increasing possibility of carrier recombination due to their short diffusion length. Similar to photoconductors, changing the intrinsic layer or modifying its optical properties will change the sensitivity of the photodiode across the EM spectrum. Employing a-Si:H based 3-D material structure has the potential to engineer infrared sensitivity to photodiodes.

2.3.4 Thin Film Transistors

Thin-film transistors (TFTs) are a type of field-effect transistors (FETs) with three terminals – gate, source and drain – and utilize a thin film as the active conducting channel as schematic shown in Fig 2.14. TFTs have found applications in displays, chemical sensors, and x-ray detectors [79]–[81] where emphasis is on large area coverage. They are switching devices as they can control current flowing between the drain and source (I_D) by varying the voltage at the gate (V_G). They are usually made on amorphous substrates using amorphous, polycrystalline or organic semiconductors. A-Si:H TFTs have intrinsic a-Si:H thin film as the channel layer.

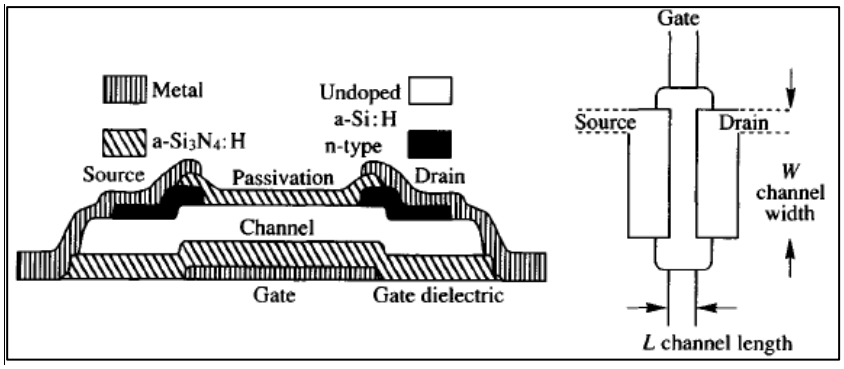

Fig 2.14 Schematic illustration of a TFT and MOSFET [82]

TTFs can be fabricated using a Back Channel Etched (BCE) process or Etch Stop (ES) process. In the BCE process, the gate electrode, dielectric layer, intrinsic layer and doped layer are deposited in that order. A back-channel etch is then used to separate the connected doped layers on the source and drain regions thereby enabling the intrinsic layer as the channel for accumulation of charge to flow from source to drain. In the ES process, an etch stop dielectric layer is included immediately after the intrinsic (channel) layer deposition. The etch stop layer then serves as the etch stop protection for the intrinsic channel layer during the isolation etching of the source and drain doped layers. The presence of an etch stop in the ES process protects the back channel from damage during the isolation etching. This however requires and extra mask for fabrication which makes it a more expensive process. The impact of the back channel damage of the BCE process can be minimized by post annealing.

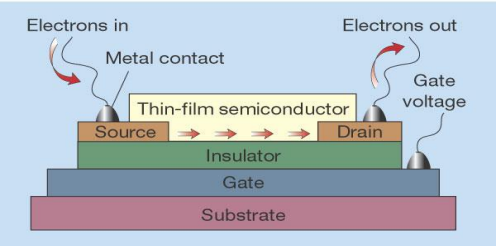

Fig 2.15 Schematic illustration of the operation of a TFT [81]**; (b) Transfer characteristics of a typical a-Si:H TFT. Inset is typical output characteristics**

A-Si:H TFTs are typically n-type accumulation mode devices. The drain current (I_D) from the TFT can be modelled using the gradual channel approximation model given in equation 2.11 where C_{ox} is the capacitance per unit area, μ_{FE} is the field effect mobility, W is the channel width, L is the channel length, V_G is the gate voltage, V_T is the threshold voltage and V_D is the drain voltage. As shown in Fig 2.15 [81], a positive voltage on the gate accumulates electrons to the dielectric/semiconductor interface thereby creating a channel. The accumulation of electrons on the intrinsic channel reduces its resistivity thus enabling the electrons to conduct when a drain voltage is applied. When $V_G > V_T$ (i.e. the gate

voltage reaches a threshold), a large number of charge carriers can flow from source to drain through the high conductive channel layer and the TFT is said to be in the ON state.

$$I_D = C_{ox}\mu_{FE}\frac{W}{L}\left\{(V_G - V_T)V_D - \frac{1}{2}V_D^2\right\} \qquad 2.11$$

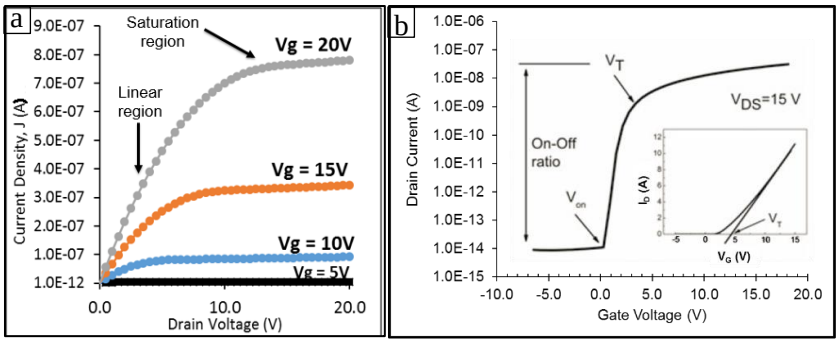

Fig 2.16 Typical (a) Output and (b) Transfer characteristics of a TFT. Inset of (b) is the transfer characteristics on linear scale

I-V characteristics of a TFT can be defined by output and transfer characteristics as shown in Fig 2.16. The output characteristics show the relationship between the drain voltage and drain current at constant gate voltages and provide qualitative information about the device performance such as channel pinch off and contact resistance. The transfer characteristics show the relationship between the gate voltage and drain current and are a measure of the gate control. The ON/OFF ratio, defined as the ratio of the ON current (I_{on}) to the OFF current (I_{off}) (Fig 2.16b), is a measure of the TFTs switching ability and can be obtained from the transfer characteristics in semi-log scale. In linear scale, the threshold voltage can be obtained and is given by the intercept on the voltage axis of a straight line fit to the I_D-V_G curve at low drain voltages.

The ON state of a TFT involves two main regimes – the linear and saturation regions – determined by the drain voltage (V_D) and the threshold voltage (V_T). A TFT is in linear region when $V_D < V_G - V_T$ and is governed by equation 2.11. When $V_D \geq V_G - V_T$, the TFT is in saturation mode and the drain

voltage becomes governed by equation 2.12 where the mobility is then known as the saturation mobility. At saturation condition, drain current becomes constant and independent of drain voltage.

$$I_{Dsat} = \frac{1}{2} C_i \mu_{sat} \frac{W}{L} (V_G - V_T)^2 \qquad 2.12$$

Chapter 3
Materials Development

This chapter presents the development of 3-D materials system comprising of ZnO NW core and conformally coated a-Si:H shell. The synthesis of the ZnO NWs that serve as the backbone of the 3-D materials system is first presented in Section 3.1 while the characterization of the grown ZnO NWs is presented in Section 3.2. Process parameters and their effect on the morphology and properties of the ZnO NW network are discussed in Section 3.3. Conformal coating of the ZnO NWs with a-Si:H is presented in Section 3.4 including the characteristics of the coated films.

3.1 Hydrothermal ZnO NW Synthesis

The hydrothermal set up used here is a simple set up that consists of a hot plate, thermometer and glassware (covered with Al foil for optimum heat distribution) as shown in Fig 3.1. ZnO NWs were synthesized on different substrates such as Si or glass. The substrate was first cleaned using standard RCA-1 cleaning procedure. A seed layer was then deposited on the cleaned substrates. Different seed layers were studied as will be discussed later. The seeded substrates were then immersed into a hydrothermal bath containing solutions of zinc nitrate hexahydrate ($Zn(NO_3)_2 \cdot 6H_2O$, Sigma Aldrich) and hexamethylenetetramine (HMTA) ($C_6H_{12}N_4$, Sigma Aldrich). The growth process is affected by several conditions that include concentrations of the precursor salts, relative volumes of the solution mix, sample orientation, growth temperature, rate of temperature rise, single or multi-stage growth and solution replenishments. After growth, the substrate was washed with de-ionized water and dried with nitrogen.

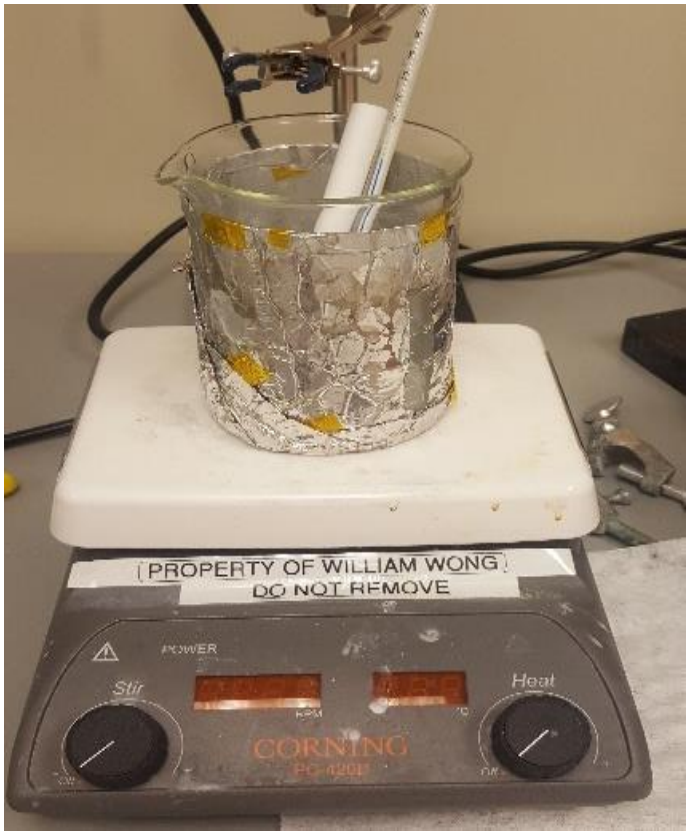

Fig 3.1 Hydrothermal set up for the growth of ZnO NWs

3.2 Zinc Oxide (ZnO) Nanowire (NW) Characterization

The characterization of the zinc oxide nanowires (ZnO NWs) involved scanning electron microscope (SEM) micrographs of several sections of a given sample from where order, uniformity, density, length and diameter of the nanowires can be determined. Order or disorder information were obtained by observing the orientation and spacing of the NWs from the SEM micrograph. Uniformity and density information were calculated from the plan view SEM micrographs of several sections of a given sample where the number of nanowires in a specified area was manually counted and the average number taken as a representative number. The length and diameter information were obtained from the cross-sectional SEM micrographs with the average value also taken as a representative number. The composition of the NWs were obtained from an Energy Dispersive X-ray (EDX) measurement attached to the SEM.

ZnO NWs grown by the hydrothermal technique are disordered as shown in Fig 3.2a. In its original growth technique, the ZnO NWs contained a lot of debris as shown in Fig 3.2b and Fig 3.2c. These debris are a consequence of the concurrent nucleation in the solution of random particles which do not attach to the seed as part of the desired NW. A simple orientation flip (Fig 3.2d) (from growth surface facing upwards to facing downwards) however, eliminated most of these debris as gravity allowed them to fall on the back of the substrates which can be easily wiped off. The grown ZnO NWs were composed mainly of Zn and oxygen (O) as shown by an Energy Dispersive X-ray (EDX) spectra (Fig 3.2e). The Si peak in the EDX spectra is due to the Si substrate on which the ZnO NWs were grown.

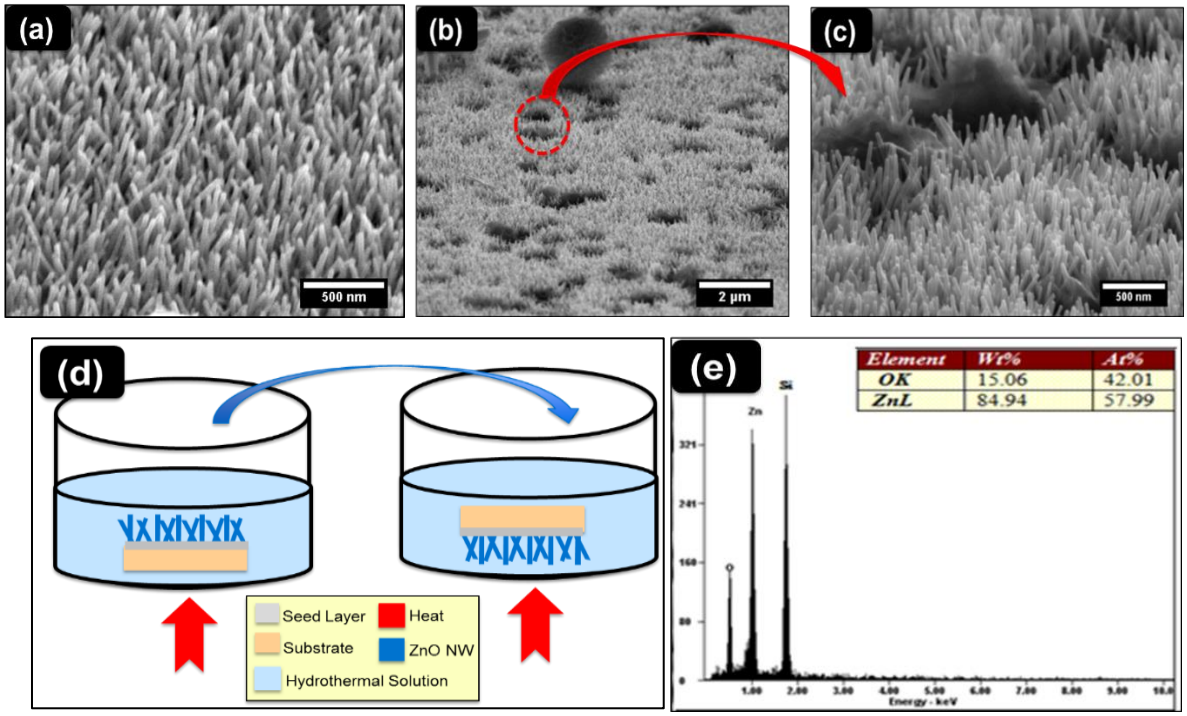

Fig 3.2 (a) Disordered zinc oxide nanowires (ZnO NWs) grown from a hydrothermal solution; (b) Debris concurrently nucleating in the hydrothermal solution with the ZnO NWs; (c) Magnified image of the debris of (b); (d) Schematic illustration of substrate orientation flip to eliminate the debris on ZnO NWs; (e) EDX spectrum of typical ZnO NWs grown on a Si substrate. The Si peak is the contribution of the substrate

3.3 Control of Growth (Nanowire) Parameters

3.3.1 Seed Layer and Density Control

A seed layer is essential to crystallize the nanoparticle formation out of the supersaturated solution and onto the substrate [65], [68], [83]–[85]. In the absence of a seed layer, the nanoparticles would aggregate together within the solution to form micron or millimeter sized particles that would eventually turn the solution cloudy. The choice of the seed layer parameters also has other effects on the nanoparticle growth. For example, to a large extent, it dictates the density of the crystallized nanoparticles [68], the growth rate [84] and in some cases, the diameter and crystallinity [86].

Several seed layers have been reportedly used for hydrothermal growth. These include rf sputtered seed layers [68], [83], [84], [86] and spin coated nanoparticle seed layers [65], [85]. In this thesis, both the spin coated nanoparticle and rf sputtered seed layers were investigated but with focus on the latter.

The nanoparticles used as a seed layer can be dispersed in water or in ethanol. The dispersed nanoparticles are spin coated onto a substrate and annealed to crystallize after which the substrate is then used for hydrothermal growth. While several groups have reported success with spin coated nanoparticle seed layer, this method requires extra diligence for sustained consistency. In the low NW density regime, control is relatively easy. However, for higher NW densities, the control becomes quite difficult. The variables that can affect the NW density from the nanoparticle seed layer process include concentration of the dispersed nanoparticle, the dispersant, the spinning recipe such as speed, acceleration and duration, the crystallization anneal temperature and time, the initial state of seed layer surface and the type of material on the surface, post seed layer handling including method of introduction into the hydrothermal solution [85] among others. Representative SEM micrographs of ZnO NWs grown from nanoparticles in water and ethanol are shown in Fig 3.3.

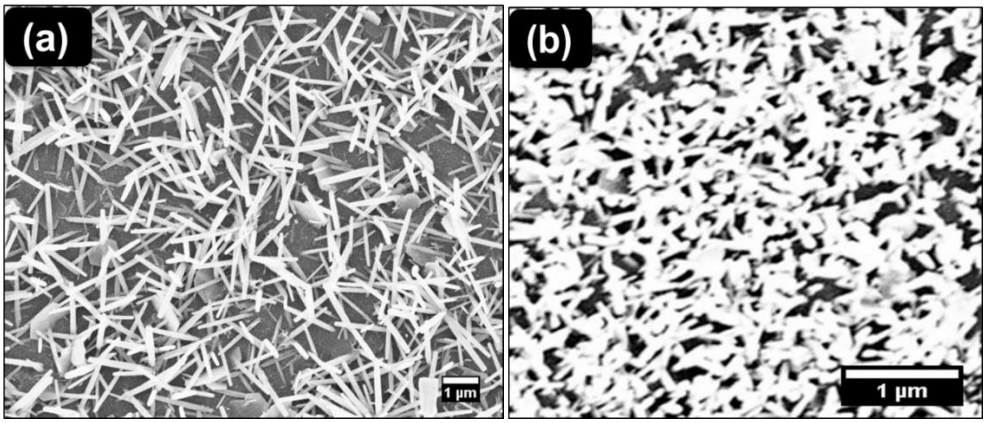

Fig 3.3 ZnO NWs grown from zinc acetate nanoparticles dispersed in (a) water; (b) ethanol

On the other hand, the rf sputtered seed layer can control the NW density based on its thickness [68]. According to Liu *et al.*, slight changes in thickness of the seed layer up to a threshold of 3.5 nm have significant effects on the density of the NWs, above which thickness changes have minimal effect [68]. In addition, according to the Ostwald-Freundlich relation given in equation 2.7, the threshold is a moving number determined by the type of surface the seed layer sits on. For example, under the same conditions, Fig 3.4 shows that different NW configurations were obtained when rf sputtered seed layer was used on prior patterned Cr substrate containing areas with Cr and glass surfaces. In a uniform surface however, changes in the thickness of the seed layer affect the density of the obtained NWs (Fig 3.5) when all other factors are kept constant. In general, rf sputtered seed layers between ~ 0.7 – 1.2 nm were used as the seed layer for the hydrothermally grown NWs presented in this thesis. The seed layer thickness was estimated by extrapolating it down from the thickness of a thick ZnO film based on its growth rate. The growth rate of the seed layer ZnO film was intentionally reduced to 0.07 nm/min in order to better control the process and account for small changes in thickness.

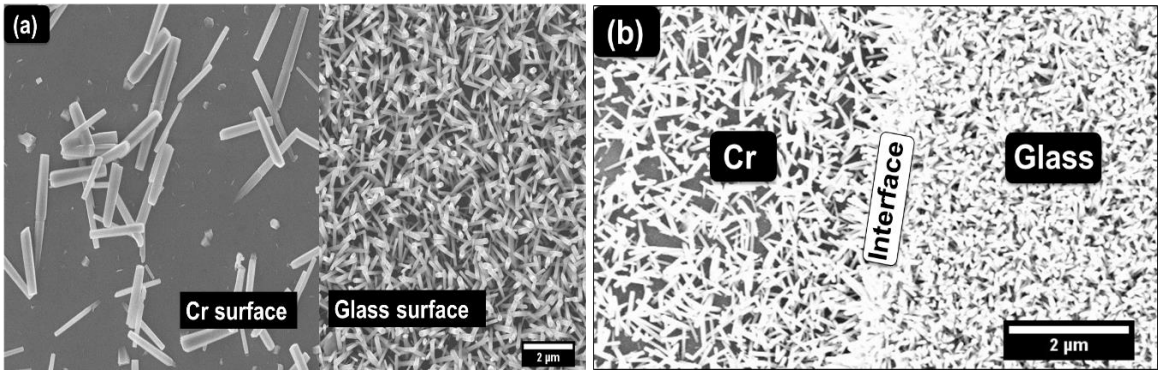

Fig 3.4 ZnO NWs grown on patterned Cr substrates with the same seed layer and hydrothermal conditions applied but with different NW configurations on the Cr and glass sides of the substrate (a)0.81nm seed layer; (b) 0.96nm seed layer

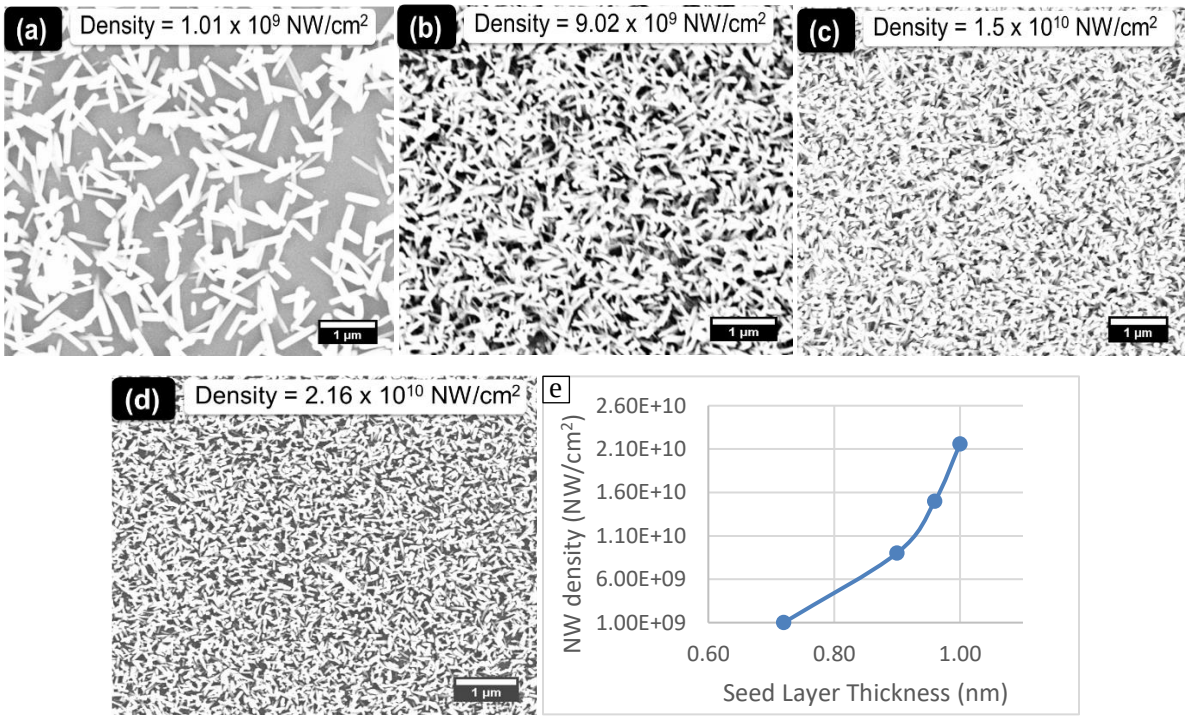

Fig 3.5 Seed Layer effect on density of ZnO NWs on Cr surface grown at 85°C (a) 0.72nm seed layer; (b) 0.90nm seed layer; (c) 0.96nm seed layer; (d) 1.00nm seed layer; (e) plot of seed layer changes against obtained NW density

3.3.2 Growth Temperature Dependence

The temperature of the hydrothermal growth is a very important factor for NW growth [65], [87]. In optimizing the growth temperature of the hydrothermal process used here, a temperature of 80°C was chosen for glass and molybdenum seed layer surfaces and 85°C for chromium seeded surfaces. The reasons for these two temperature sets, was to maintain similar NW density and properties from run to run.

In general, as Fig 3.6 shows, temperatures below 60°C lead to nucleation of random nanostructures in the solution at very slow rates while temperatures above 85°C lead to formation of thick diameter NWs and very fast growth rates. High temperatures lead to higher growth rates by consuming Zn^{2+} ions faster leading to a milky solution very early into the hydrothermal growth and manifests in relatively larger diameter NWs.

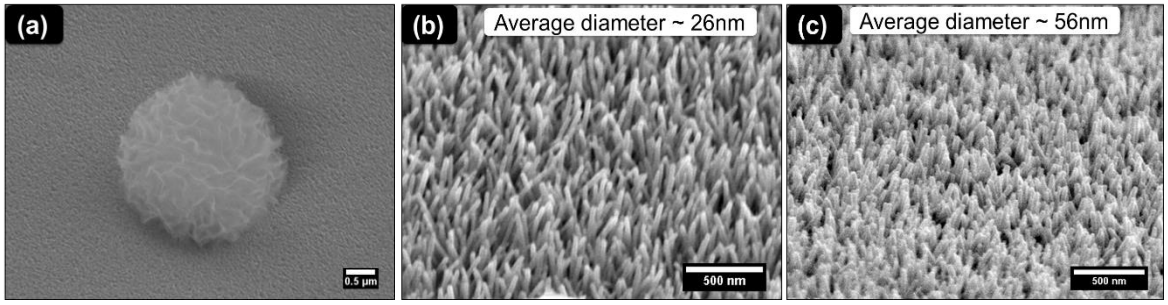

Fig 3.6 ZnO nanostructures obtained at varying temperatures (a) < 60°C; (b) 80°C; (c) 85°C

An implication of the Ostwald-Freundlich equation (equation 2.7) as it relates the hydrothermal process, is that the seed layer and temperature have an inter-relationship. According to Fig 3.7, the same seed layer gave different NW densities when the nanowires were grown at different temperatures. As temperature increases, the nominal crystal size required for NW nucleation reduces thereby leading to higher NW densities as smaller crystal sizes that would otherwise be ineffective become effective in ZnO NW nucleation. This is in agreement with Xu and Gao [65] and can be extended to Fig 3.4. Lithographic patterning of the Cr surface deposited on a glass substrate exposed dissimilar surfaces

comprising of portions of Cr and glass with its attendant different surface properties and energies. The different surfaces (and energies) gave rise to different requirements for the minimum size of seed crystal needed for NW nucleation even though both surfaces were exposed to the same rf sputtering condition and nominal crystal sizes. This dissimilar requirement leads to a distortion in the distribution of effective crystal sizes on the different surfaces where a given nominal seed crystal size leads to higher supersaturation and therefore sufficient for nucleation in some areas (one surface) and lower supersaturation and therefore poorly effective in other areas (other surface). This difference in effective supersaturation under the same nominal crystal size but different surfaces then leads to different NW densities on the glass side and on the Cr side. In order to maintain similar NW density on the different surfaces, different growth temperatures were used with lower temperatures for glass and Mo surfaces while higher temperatures were used when Cr surface is involved.

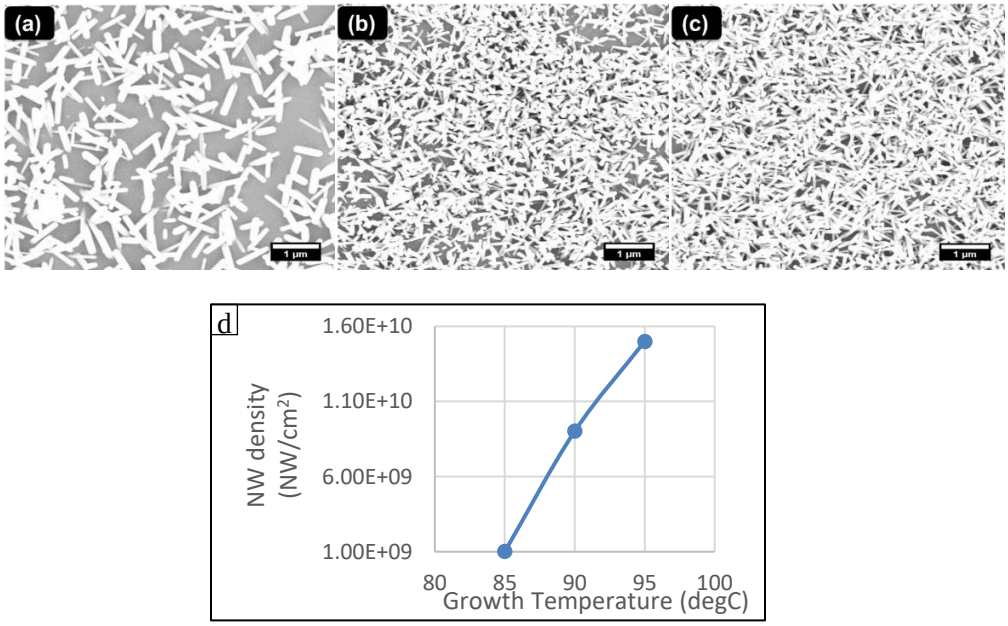

Fig 3.7 SEM micrographs of ZnO NWs grown on 0.72nm seed layer on Cr surface at (a) 85°C; (b) 90°C; (c) 95°C; (d) Plot of temperature effect on NW density

3.3.3 Nanowire Length and Growth Rate

The length of the nanowires depend greatly on the growth rate of the nanowires. The growth rate of the nanowires however depends on several factors such as duration of growth and solution volume. These factors affect the concentration of Zn^{2+} ions available in the solution for nucleation. The decrease in the concentration of Zn^{2+} ions within the first 2 hours of growth [57] implies that growth rate will reduce for longer growth time except the low concentration of Zn^{2+} ions are replenished. When the hydrothermal solution was replaced every 2 hours, the growth rate remained fairly constant. However, growing the nanowires non-stop for longer duration without solution replenishment reduced its overall growth rate and decreased the additional lengths added with time as shown in Table 3.1.

Table 3.1 – Growth rate of ZnO NWs with time and growth mode

Duration	2hr	4hr	4hr	6hr	15hr
Growth Mode	Non-stop	Replenished after 2hr	Non-stop	Non-stop	Non-stop
NW Length	1.5µm	3µm	2µm	2.5µm	4.5µm

In addition to duration of growth, growth mode and solution volume, growth rate of ZnO NWs was also affected by growth temperature and NW density. As discussed in Section 3.3.2, higher temperature leads to a faster consumption of Zn^{2+} ions which in turn leads to faster nucleation and longer nanowires as shown in Table 3.2. Higher NW densities however spreads the available Zn^{2+} ions among the many nucleation points which reduces the overall elongation each NW experiences leading to slower growth.

Table 3.2 – Nanowire lengths obtained after 4hr growth at different temperatures

Growth temperature	80°C	85°C
Nanowire Length	2µm	3.5µm

3.4 Hybrid Materials System

3.4.1 Conformal Coverage Recipe Development

Hydrogenated amorphous silicon (a-Si:H) is typically grown using a CVD type method as was discussed in Section 2.2.4. Here, a PECVD (Fig 3.8) method was used with its unique feature of low temperature processing. The use of a PECVD means the a-Si:H growth has to be optimized for conformal coverage since plasma deposition tends to be intermediate between the CVD and PVD extremes [16]. The process factors that affect the growth and properties of a-Si:H films grown in a PECVD include the gas flow rate, process pressure, rf power and temperature [16], [72] and have significant impact on the conformal coating process. The decomposition of silane (SiH_4) in a PECVD chamber leads to the formation of both stable and unstable radicals and in some cases, ions. For CVD-like conformal growth of a-Si:H film, surface reactions need to occur from the stable species [16], [72].

Fig 3.8 – Multi-chamber PECVD Cluster System

Table 3.3 PECVD Process Variables and Their Effect on Conformal Coating Process

Process Variable	**Range**	**Effect**
Power (W/cm^2)	0.008 – 0.013	Determines growth rate
Pressure (mT)	250 – 1000	Affects growth rate. At very high pressures, film uniformity is impacted. Very high pressures can also affect plasma stability
Temperature (°C)	150 – 260	Affects growth rate. Can help correct uniformity problems associated with high pressure. Affects material quality
Silane (/Hydrogen) (mT)	20 – 50 (/0)	Affects material quality. Determines chamber refresh rate at which fresh silane (SiH_4) molecules are supplied. SiH_4/H_2 ratio also affects hydrogen incorporation and this affects material quality

Table 3.3 shows the varied parameters and a summary of their effects. These effects are consistent with literature documentation [16]. When the rf power density was increased from $0.008W/cm^2$ to $0.013W/cm^2$, the growth rate increased from ~ 3 nm/min to ~ 9 nm/min. This increase in growth rate is due increased dissociation of SiH_4 molecules by the increased energy supplied by the increased rf power. Similarly, when the pressure was increased from 750 mT to 900 mT, the growth rate reduced from ~ 8 nm/min to ~ 3 nm/min. This reduction in growth rate with increasing pressure is due to the reduction in the mean free path between collisions. The low mean free path reduces the reactions at the growing surface due to the reduced average distance the stable radicals are able to travel. At very high pressures, film uniformity is affected and plasma becomes more unstable. The temperature of the growing surface also affects film growth. When the temperature was increased from 150°C to 220°C, growth rate increased from ~ 7 nm/min to ~ 9 nm/min. This increase in growth rate is due to the increase in surface energy of the growing surface thereby enabling more chemical reactions at the growing surface which then leads to higher growth rate. The higher surface energy of the growing surface also impacts the surface mobility of the growing species thereby improving film uniformity. In very high

pressure growth conditions, increasing the growth temperature corrected the uniformity problems created by the high-pressure environment. The precursor gas flow rate determines the residence time of gas species and dissociated radicals, and impacts the chamber refresh rate. These affect the quality of material produced by determining the rate of supply of fresh precursors into the chamber to replace dissociated and unstable radicals thereby preventing them from getting incorporated into the growing film. Addition of hydrogen gas improved the quality of the film and reduced the density of states by an order of magnitude (this will be further discussed in Chapter 4).

The development of a conformal coating process was based on the need to slow down the rate of growth and give the species that will eventually get to the growing surface sufficient time to migrate around the surface and sidewalls of the 3-D morphology.

The eventual a-Si:H conformal deposition recipe incorporated the following key effects:

- A moderate power that is high enough to dissociate SiH_4 molecules but significantly low to maintain a low growth rate and stable plasma
- Moderately high gas flow and high chamber pressure to keep growth rate low and maintain high collision between radicals. The high collision between radicals is needed to lower the mean free path of the growing radicals and thus reduce the growth rate of the film while also refreshing the gas precursors and supplying fresh set of stable radicals for growth. This enables unstable radicals to be pumped out of the chamber before they can be incorporated into the growing film.

The rationale behind this lies in the creation of a high gas refresh – high collision condition to engineer competition between the precursor radicals such that only the stable ones emerge with desirable properties such as high surface migration and low sticking coefficient to effectively coat the

sidewalls. The result is a conformally coated film on the NWs which preserved the 3-D morphology of the underlying NW network.

This technique was also used to develop conformally coated doped a-Si:H, silicon nitride (a-SiN_x) and silicon oxide (a-SiO_x) films on the ZnO NWs. Table 3.4 shows the final parameters used for the a-Si:H coating recipe.

Table 3.4 Parameters Used for CVD Conformal Deposition of a-Si:H

Process Parameter	**Process Value**
Power	0.013 W/cm^2
Pressure	750mT
Temperature	150°C
Silane	50sccm
Hydrogen	0

3.4.2 Film Coating

The conformal coating characteristics of the coated films were evaluated by two main techniques. The first method involves determining the etch selectivity of the underlying ZnO NWs. Given that ZnO materials readily etch in hydrochloric acid (HCl), uncoated or poorly coated ZnO NWs will etch readily in HCl compared to conformally coated NWs. Uncoated, poorly coated and conformally coated samples were subjected to a 2 % HCl etch test. The uncoated samples etched completely within a few seconds of immersion into the wet etchant. The poorly coated samples experienced undercutting of the underlying ZnO NWs which led to a collapse of the top film and manifested in peel offs observed floating in the HCl solution. This peel off occurred because the coated film had no adhesion to the substrate but to the top of the ZnO NWs that etched through the gaps in the coating, releasing the films. The conformally coated samples showed no signs of etching well over 7 minutes of immersion in the HCl etchant.

The second test for the conformal coating was done using a scanning electron microscope (SEM). Fig 3.9 shows typical SEM micrographs of uncoated, poorly coated and conformally coated samples and their cross sections. For the conformally coated sample (Fig 3.9c), the figures show that the conformal coating was done through the length of the NWs with similar final diameters for the NWs both at the base and along its length. In addition, a closer look at the edge of the coated samples (Fig 3.9d) shows that the hexagonal structure of the underlying ZnO NW was preserved. The poorly coated samples show a textured-like surface instead of the original 3-D morphology (Fig 3.9b). A closer look at the cross sectional SEM image reveals voids from which the HCl solution could attack the ZnO material leading to undercutting.

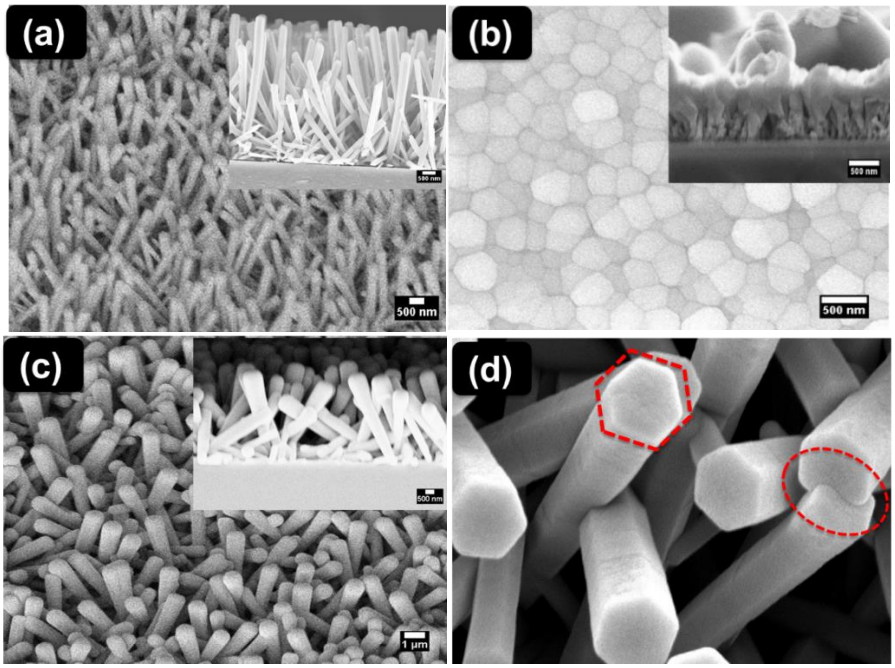

Fig 3.9 - SEM micrographs of (a) Uncoated ZnO NW sample. Inset is the cross sectional SEM image; (b) Poorly a-Si:H coated ZnO NW sample (inset is the cross sectional SEM image); (c) Conformal a-Si:H coated ZnO NW sample (inset is the cross sectional SEM image showing the uniform diameter of the coated NWs across its length); (d) Zoomed SEM micrograph of conformal a-Si:H coated ZnO NW. The hexagonal edges of the ZnO NW is preserved even with the coating and NW intersections and graciously coated. Scale bars of insets are 500nm

An important consideration in developing and preserving the conformal coating process is the NW length vs film thickness (NvF) factor (Fig 3.10). For a given NW density, there is a limit to how much film that can be added before the 3-D morphology gets consumed. This consideration relates the NW density to the conformal coating process. Thus, the maximum thickness of a film that can be conformally coated on a NW network is less than or equal to half of the average separation between the NWs. Above that thickness, there will be no free space for lateral growth of additional film and all additional film growth will occur at the top surface. This argument can also be applied to the starting NW density. If the starting NW density is too high such that the spacing between the NWs is too small, this will provide less room for subsequent a-Si:H film to grow on the NW sidewalls and good conformal coverage will be hard to achieve. At very low NW densities, special attention to recipe optimization becomes less critical.

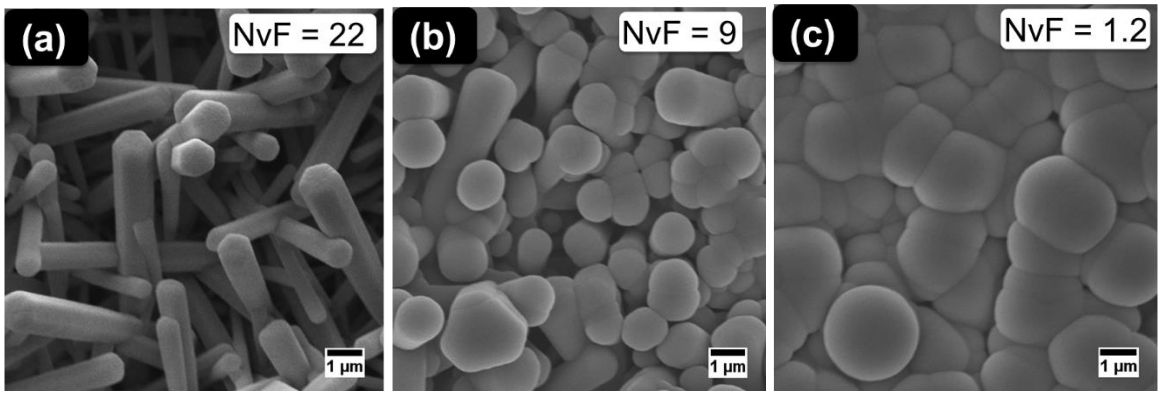

Fig 3.10 SEM micrograph of different NvF factors and their impact on the conformal 3-D morphology (a) NvF=22; (b) NvF=9; (c)NvF=1.2

3.5 Summary

This chapter presented the set-up and demonstration of the hydrothermal technique for the growth of ZnO NWs. The various process conditions and how they affect the NWs obtained have also been studied and presented. At seed layers between 0.72 nm – 1.0 nm and temperatures between 80°C to

95°C (depending on seed layer surface used), NW densities of between 1.01 x 10^9 and 2.1 x 10^{10} NWs/cm^2 were obtained. Conformal coating of the NWs with a-Si:H has also been demonstrated. Cross sectional SEM micrographs show the films are coated from the base of the NWs and etch selectivity experiments did not indicate any etching of the underlying ZnO NWs.

Chapter 4
Optical Properties of Hybrid NW – a-Si:H Core Shell Structures

This chapter presents a discussion on the optical properties of 3-D material systems made up of a-Si:H shell coated on ZnO NW cores. Section 4.1 presents the optical results from UV-Vis-IR measurements and in Section 4.2, the relative contribution of the constituent materials in the 3-D material system to infrared absorption is explored. The effects of several processing steps that have the capacity to influence the material properties are evaluated. Electrical results are also included as additional proof. Section 4.3 focuses on the contribution of defects in a-Si:H to the observed infrared properties. This section also includes results and discussion of the several variations of a-Si:H defect concentration and their correlation to infrared response and concludes with results of doped a-Si:H experiments.

4.1 3-D Material Optical Results

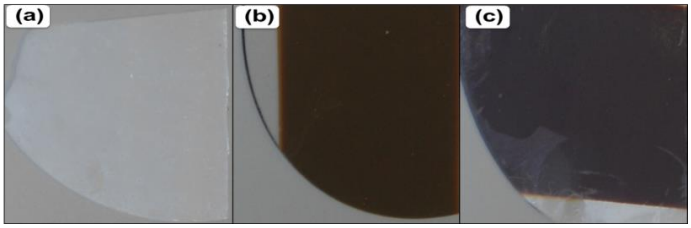

Fig 4.1 Visual Inspection of (a) Uncoated ZnO NWs on glass substrate; (b) Planar a-Si:H film on glass; (c) a-Si:H coated ZnO NWs on glass

By visual inspection, 3-D hybrid ZnO NW – a-Si:H structures appear dark with a diffuse matte appearance while planar a-Si:H film looks glossy as shown in Fig 4.1. This dark appearance is expected to translate into better optical absorption properties due to enhanced light scattering of the NW array.

Optical absorption measurements were made using a Perkin Elma Lambda 5000 UV-Vis-NIR spectrophotometer equipped with an integrating sphere. The absorption spectra *(A)* was obtained from

the measurement of the sample's total reflectance *(R)* and total transmission *(T)* across the wavelength range from 300 nm to 2.5 µm using the relation

$$A + R + T = 100 \qquad 4.1$$

Fig 4.2a shows a representative absorption spectra of bare ZnO NW, planar a-Si:H and a-Si:H coated ZnO NW. The transmission and reflection spectra of planar a-Si:H and a-Si:H coated ZnO NW is also shown in (b) and (c).

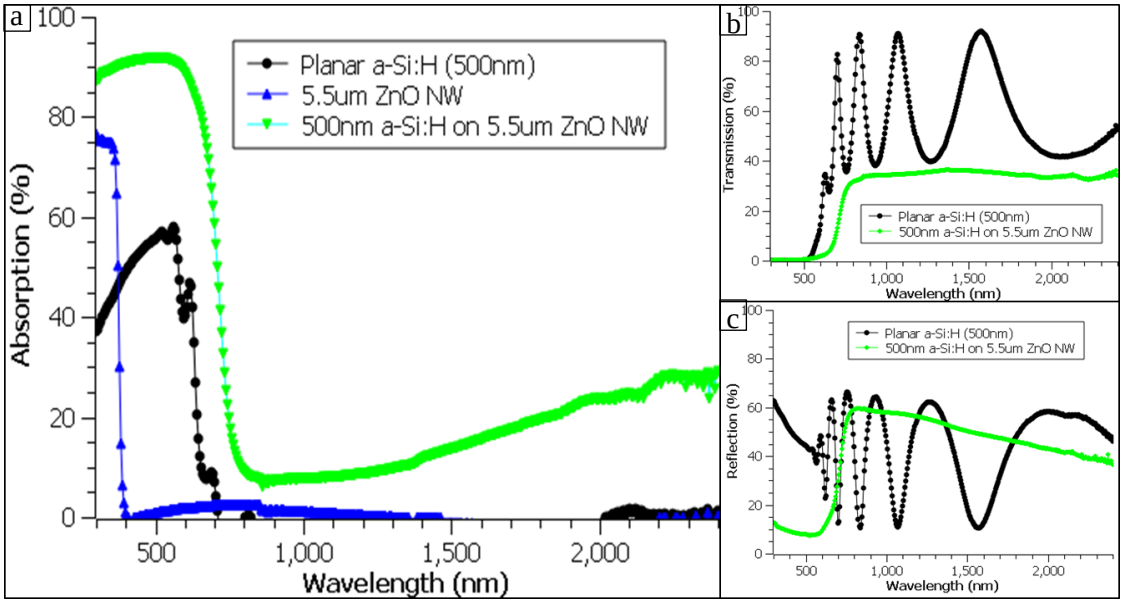

Fig 4.2 (a) Absorption spectra of 500nm planar a-Si:H, 5.5µm ZnO NWs and 500nm a-Si:H coated on 5.5µm ZnO NWs; (b) Reflection and (c) Transmission spectra of spectra of 500nm planar a-Si:H and 500nm a-Si:H coated on 5.5µm ZnO NWs

Across all wavelengths measured, absorption was enhanced for the 3-D material relative to the planar a-Si:H. This enhancement can be seen both in intensity of absorption spectra at any given wavelength and in its broadband characteristics extending beyond the ~ 700 nm cut off wavelength for planar a-Si:H material. The absorption spectra of the 3-D material structure shows a red shift relative to the planar morphology. This observed red shift will further be discussed in section 4.3.

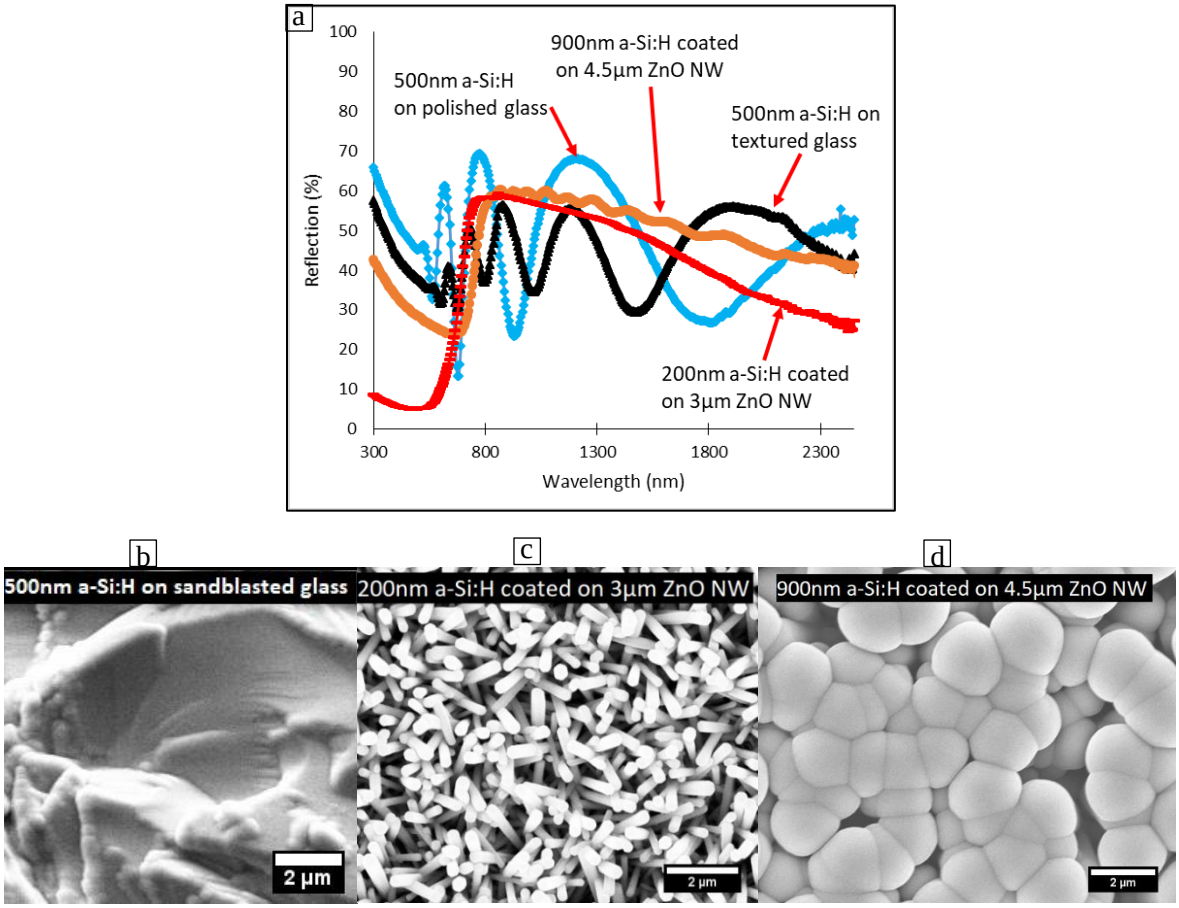

Fig 4.3 (a) Reflection spectra of a-Si:H films on different surfaces from smooth to 3-D structure; (b) SEM micrographs of a-Si:H films on rough (sandblasted) substrate; (c) 3-D nanowire structure and (d) 3-D nanowire structure showing how increasing a-Si:H thickness affects the morphology with a graduate change from 3-D to texture-like

The transmission and reflection spectra of Fig 4.2b and c shows that while the planar film showed Fabry-Perot oscillations, the oscillations are absent in the 3-D structured materials. The absence of the Fabry-Perot oscillations is a consequence of the scattering induced by the 3-D morphology. This effect can further be seen in the reflection spectra of Fig 4.3. Fig 4.3a shows the reflectivity results of 4 additional samples with a gradual change in surface morphology from planar to a rough substrate with corresponding SEM micrographs. A reduction in the Fabry-Perot oscillations in the reflection spectra can be seen as the film roughness increases, first with the sandblasted sample (sandblasted glass

substrate prior a-Si:H deposition) (Fig 4.3b) until it is completely eliminated in the 3-D sample (200 nm a-Si:H on 3 μm ZnO NWs) (Fig 4.3c). Further increasing the thickness of the a-Si:H coating on the ZnO NWs without a commensurate increase in the NW length results in a surface morphology that begins to mimic a textured film (Fig 4.3d) showing a gradual return of the Fabry-Perot oscillations. This gradual return of the Fabry-Perot oscillations has a relationship with the shell coating process as captured by the NvF Factor introduced in section 3.4.2 (Fig 3.10) and has implications for the infrared response of the hybrid material structure as is further discussed in section 4.3 (Fig 4.12).

Optical absorption reports of 3-D materials show that materials with 3-D morphology generally absorb more than their 2-D counterparts. For Si NW materials, these absorption enhancements are reportedly from strong light trapping [17], increased scattering resulting in reduced reflectivity [18], [45], defect state absorption [88], and excitation of resonance modes [45]. For a-Si:H 3-D structures, modelling results presented in section 2.2.1 revealed increased effective thickness and red light response.

4.2 Relative Absorption Contribution from ZnO and a-Si:H

The observed absorption at infrared wavelengths seen in Fig 4.2 could be due to the ZnO NWs or the a-Si:H coating or a combination of both. The conformal coating process for fabricating these 3-D material structures could impact the properties of either material. For instance, the process of coating a-Si:H on the ZnO NWs subjects the NWs to vacuum pumping, thermal annealing and plasma treatment. Similarly, the coating of a-Si:H on ZnO NWs subjects the a-Si:H coating process to different surfaces which might affect the surface reactions leading to different material properties. The investigation of the contribution or relative contribution of each material type is hence necessary for complete understanding of this phenomenon.

While undoped ZnO materials show no absorption in both visible and infrared regions, metal doped ZnO materials absorb light in the infrared wavelength region [89]–[91]. This absorption is usually attributed to free carriers and plasmonic oscillations from carriers generated by the presence of the metallic dopants [89], [90]. Hydrogen plasma treatment has also been shown to increase the conductivity of ZnO materials by introducing shallow donor states and interstitial hydrogen [92]. This increased conductivity in the absence of metal dopants however have not been shown to translate into infrared absorption [92].

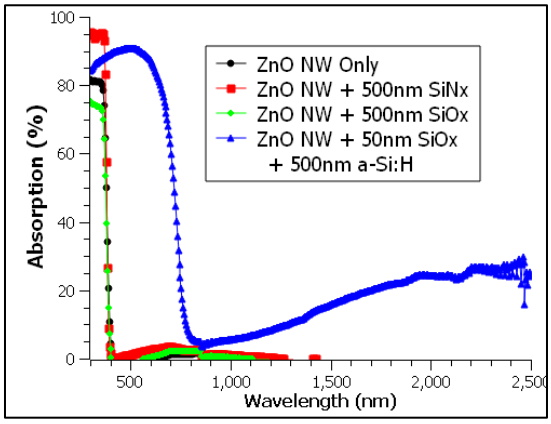

Fig 4.4 Absorption spectra of Uncoated ZnO NWs and SiOx, SiNx and dual SiOx and a-Si:H coated ZnO NWs

Fig 4.4 shows the absorption spectra of uncoated ZnO NWs and ZnO NWs conformally coated with silicon nitride (SiN_x) and silicon oxide (SiO_x) materials. As expected, the undoped ZnO NWs do not show absorption in the infrared region. Also, the figure shows that both the SiO_x and the SiN_x coated ZnO NW samples do not show any noticeable absorption both in the visible and infrared regions. The absorption in the ultraviolet region for all the samples is due to ZnO, with a band gap of 3.3 eV which corresponds to 375 nm wavelength. The absence of absorption with both SiO_x and SiN_x coated samples in the visible and infrared regions implies that the infrared absorption is not primarily due to the ZnO

NW or the ZnO NW interface with SiO_x or SiN_x. The addition of a-Si:H coating on top of SiO_x coated ZnO NW sample and its attendant absorption shows the dependence of this absorption primarily on the a-Si:H material. As seen, the absorption of the ZnO NW/SiO_x/a-Si:H material system of Fig 4.4 is similar to that of ZnO NW/a-Si:H material system of Fig 4.2a. The infrared absorption of the ZnO NW/SiO_x/a-Si:H material system of Fig 4.4 also indicates that the absorption of ZnO NW/a-Si:H material system of Fig 4.2a is not be dependent on the ZnO NW/a-Si:H interface. The inclusion of SiO_x between the ZnO NW and a-Si:H interface distorts any unique properties the ZnO NW/a-Si:H interface may have and would suppress the infrared absorption if such absorption is dependent on the ZnO NW/a-Si:H interface. The correlation of infrared absorption to the only sample with a-Si:H material suggests that a-Si:H material is the primary driver for infrared absorption in this structure.

As stated earlier, H plasma treatment has been shown to increase the conductivity of ZnO materials. Conformal coating of a-Si:H, SiO_x and SiN_x requires the decomposition of SiH_4 precursor gas. This decomposition among other radicals, releases H atoms and molecules which could interact with the ZnO NWs. However as Fig 4.4 shows, the interaction of these H radicals from SiH_4 decomposition with ZnO NWs had no impact during the SiN_x and SiO_x conformal coating process. The H radicals available during the subsequent conformal coating of a-Si:H film will have no impact on the ZnO NWs as the ZnO NW/SiO_x materials system is already conformally coated with SiO_x which shields the underlying ZnO NWs from the plasma H.

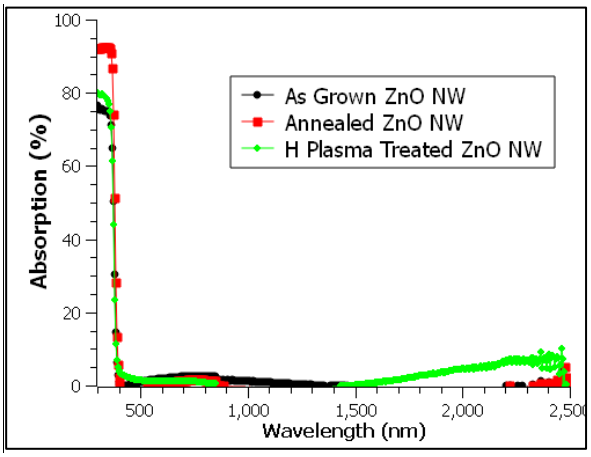

Fig 4.5 Absorption spectra of as-grown ZnO NWs, annealed ZnO NWs and hydrogen plasma treated ZnO NWs

To further evaluate the impact of various treatments (H plasma and annealing) on ZnO NWs as they relate to the infrared absorption of the 3-D materials, Fig 4.5 shows the absorption spectra of as grown ZnO NWs and ZnO NWs subjected to H plasma (250°C, 60 minutes) and annealing (360°C, 60 minutes) treatments while Table 4.1 shows the conductivity changes of ZnO films with these treatments. The results show that these treatments had minimal effect on the infrared absorption of ZnO NWs. While 60 minutes H plasma treatment had ~ 10 orders of magnitude effect on the conductivity of ZnO film (Table 4.1), the H plasma treatment result shows that in the absence of a-Si:H material, ZnO NWs do not significantly absorb infrared even with focused H plasma treatment (Fig 4.5). Despite the high number of free carriers created by the H plasma treatment as signified by its conductivity change, the optical absorption is only 6.9 % at 2.3 µm wavelength. This further confirms that the H radicals generated during SiH_4 decomposition had little impact on the infrared absorption of ZnO NW/a-Si:H materials system. Annealing treatments up to 360°C also had no significant impact on both the conductivity of the ZnO film and the optical absorption of the ZnO NW.

Table 4.1 ZnO Conductivity Changes with Annealing and Hydrogen Plasma Treatments

ZnO Treatment	Conductivity $(\Omega cm)^{-1}$	Absorption @ 2.3μm (%)
ZnO (as dep)	3.0×10^{-11}	0.2
ZnO + 360°C Vacuum Anneal	3.1×10^{-11}	0.5
ZnO + 30 minutes H Plasma Treatment	6.7×10^{-2}	-
ZnO + 60 minutes H Plasma Treatment	1.5×10^{-1}	6.9

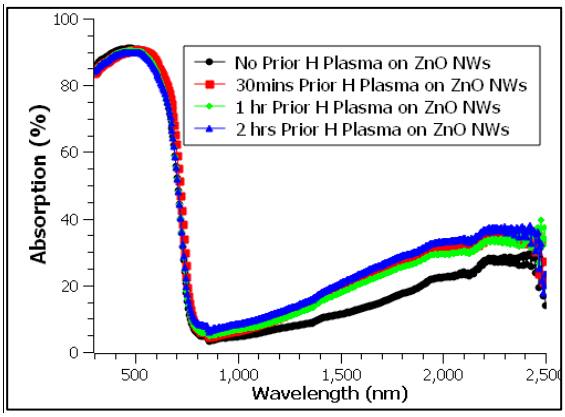

Fig 4.6 Absorption spectra of 350nm a-Si:H coated ZnO NWs subjected to different durations of hydrogen plasma before a-Si:H coating

To additionally eliminate the effect of H plasma on ZnO NWs and further assess the relative contribution of ZnO NWs on the infrared absorption of the 3-D ZnO NW – a-Si:H structure, Fig 4.6 shows absorption spectra of ZnO NWs subjected to different durations of hydrogen plasma treatment prior to conformal a-Si:H coating. As shown in Table 4.1, the conductivity of ZnO film increases rapidly during the first 30 minutes of H plasma treatment and then slows down. This trend is followed in Fig 4.6 where the H plasma treatment caused a 6.5 % change in infrared absorption at 2.3 μm wavelength of a-Si:H coated sample after 30 minutes of prior H plasma treatment relative to the sample with no H plasma treatment. Beyond 30 minutes, the change in infrared absorption saturates and shows no further increase as the duration of prior H plasma treatment increases. This observation suggests that the additional increase in free carriers generated by prolonged exposure to hydrogen plasma had little effect on infrared absorption afterwards. The 6.5 % increase in infrared absorption with prior H plasma

treatment of ZnO NWs signifies the maximum contribution of ZnO NWs to the infrared absorption and is in line with the change observed in Fig 4.5. With no additional H plasma treatment, 25 nm a-Si:H coating is achieved within 4 minutes of coating thus implying the ZnO NWs are exposed to the SiH_4 plasma for less than 4 minutes before they are fully covered and shielded.

Table 4.2 Change in Infrared Absorption for Prior H plasma Treated a-Si:H coated NWs

Material	Absorption at 2.3μm (%)	Change in Absorption (%)
ZnO NW + 500nm a-Si:H coating	28.4	0
ZnO NW + 30min H plasma treatment + 500nm a-Si:H coating	34.9	6.5
ZnO NW + 60min H plasma treatment + 500nm a-Si:H coating	33.9	5.5

Furthermore, electrical photoconductivity measurements were made to isolate the dominant optical-absorption material. Fig 4.7 shows the schematic structure of planar and 3-D photoconductors and their infrared response. An intentional 5 μm gap was created in the 3-D photoconductor between the edge of the ZnO NWs and the contacts to isolate the ZnO NWs from the contacts such that currents measured will be due to the a-Si:H only. In this structure, the ZnO NW will enable the 3-D morphology while also isolated from the contacts and therefore make no contribution to measured infrared response. Additional isolation can be realized with a thin conformal silicon nitride (SiN_x) before the a-Si:H coating. The addition of SiN_x before a-Si:H coating has no effect on device performance since SiN_x can be conformally coated over the ZnO NWs, and the contacts are only deposited after the a-Si:H coating. An infrared LED of 1.55 μm wavelength was used as the infrared source to excite the photoconductors in addition to white light from the probe station. The results show two orders of magnitude difference between the dark current density and infrared-generated current density in the 3-D photoconductor while the planar photoconductor has a more subdued difference. The presence of the gap between the contacts and the ZnO NWs isolates the ZnO NW contribution and confirms that infrared absorption is

primarily from the a-Si:H coating. In addition, the presence of some infrared response from the planar a-Si:H photoconductor shows a-Si:H could absorb infrared if properly tuned, and eliminates the ZnO NWs as the primary contributor of the infrared absorption. However, such absorption in a-Si:H can significantly be increased in a 3-D morphology that enables thicker effective film and lower reflection as demonstrated by the 3-D photoconductor results.

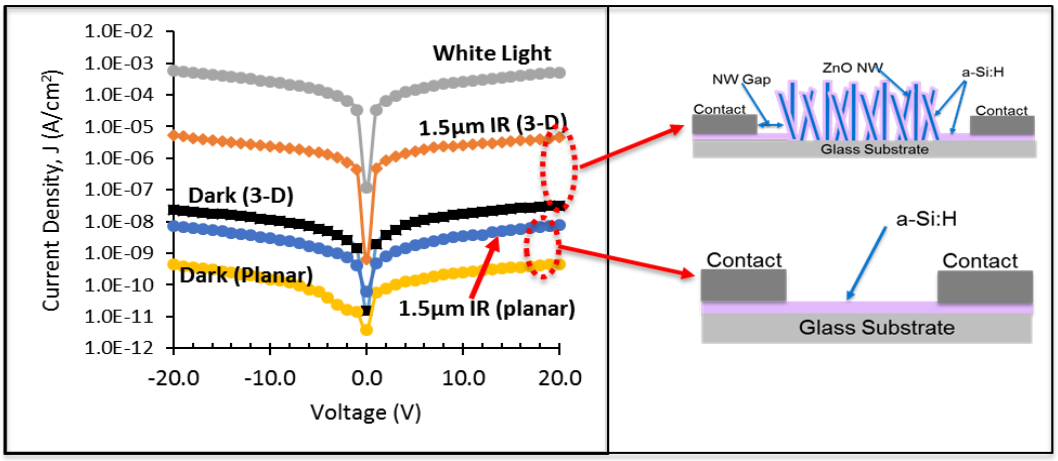

Fig 4.7 Photoconductivity results of planar and 3-D photoconductors with incorporated NW gap for isolating the contribution of ZnO NWs

4.3 Defect Mediated Absorption

In the previous section, it was established that a-Si:H is the dominant absorber material contributing to the infrared absorption. This proposition does not negate the role of ZnO NWs in providing the 3-D morphology that has enabled the infrared absorption. In this section, the phenomena driving the absorption in a-Si:H is explored.

Defects in a-Si:H has huge implications on its material properties, which affect device performance and stability. The control of defects in a-Si:H is therefore very important for device application. Numerical modelling shows that sub-band-gap optical photoconductivity in a-Si:H is related to mid-gap states density and distribution [93]. Yahya *et al.* showed that mid-gap defect density increases with

decrease in H concentration in the a-Si:H film [94]. It has also been shown that a-Si:H grown from pure SiH_4 with less H dilution produces a material containing higher concentration of the defective $Si\text{-}H_2$ bonds than those grown with H dilution [95].

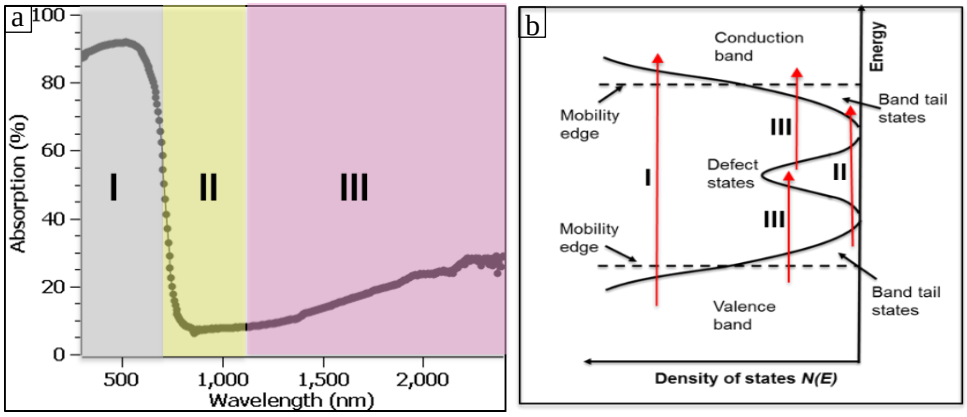

Fig 4.8 Typical absorption spectrum of a-Si:H coated ZnO NW divided into three distinct regions; (b)Density of states diagram of a-Si:H material showing possible transitions.

Infrared absorption in the a-Si:H shell of the 3-D material system could be primarily defect mediated. Defect states within the tail states and mid gap provide low-energy secondary states that enable infrared absorption. This concept can be understood with the aid of Fig 4.8. Here the absorption profile is divided into 3 Regions. Region I corresponds to band-to-band transitions and is the dominant mechanism for high energy ($\lambda \leq 750$ nm) absorption within the visible spectrum. Region II corresponds to transitions between the tail states as shown in the density of states diagram. The concentration of states within the valence and conduction band tail states or the amount of light interaction with these states thus dictate the extent of transitions within this region. Therefore, increasing or decreasing the concentration of the tail states of the coated a-Si:H shell would increase or decrease the absorption in this region accordingly thereby changing the slope at the boundary of Regions I and II or within Region II. Region III corresponds to transitions through the mid-gap states. The implication of this mid-gap

mediated transition is that more defective a-Si:H shell containing elevated concentration of mid-gap states will lead to higher absorption in Region III.

Defect mediated absorption in conjunction with scattering and effective thickness enhancement could be responsible for the red shift observed between the planar a-Si:H and hybrid ZnO NW – a-Si:H core-shell structures of Fig 4.2a. In this case, the red shift can be categorized into Region II absorption and primarily influenced by the tail states within the planar and coated a-Si:H films. In contrast to the 3-D morphology, the short interaction length of the planar surface is not sufficient to enable these tail states to become optically active. Increasing the interaction length of light with the tail states as the material transforms to a 3-D structure leads to a red shift in its absorption spectra due to increase in transition of between valence band tail states to conduction band tail states (Fig 4.9a).

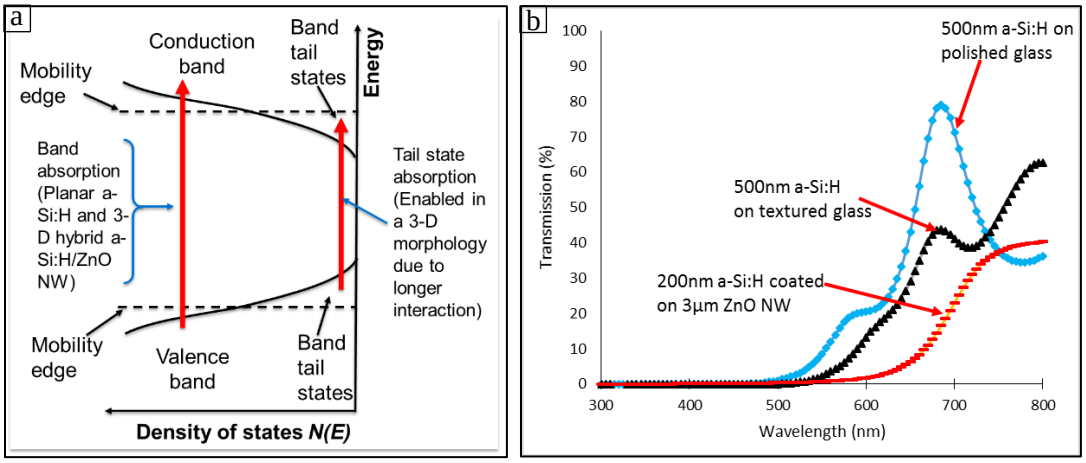

Fig 4.9 (a) Schematic illustration of the origin of the red shift between planar and 3-D a-Si:H structures; (b) Transmission spectra of a-Si:H film on different surface morphologies

This transition is supported by the transmission spectra of the samples with varying morphology (Fig 4.3b-c) as shown in Fig 4.9b. The zero-transmission edge can be used to correlate the absorption edge and red shift as it also represents the region where the optical absorption is highest (and reflection remains relatively constant). As the surface transforms from a smooth surface to 3-D morphology, this

edge red shifts by ~ 30 nm (80 meV) for the textured surface and ~ 130 nm (290 meV) for the 3-D surface. For the 3-D morphology, this corresponds to absorption from states that are ~ 145 meV from the a-Si:H mobility edges and is within ~ 400 meV and 200 meV of typical valence and conduction band tails of a-Si:H films, respectively [16].

4.3.1 Amorphous Silicon Material and Defect Characterization

In order to further investigate the defect mediated hypothesis, materials with varying defect concentrations are needed. In Chapter 2, it was observed that density of defects in a-Si:H can be varied by H passivation. To further this, two a-Si:H thin films were investigated. Recipe A was grown with pure SiH_4 gas while recipe B was grown with H_2 diluted SiH_4 at a SiH_4/H_2 ratio of 1/5. The microstructure of the a-Si:H films was investigated using FTIR. Here, two typical peaks investigated are 2000 cm^{-1} corresponding to typical Si-H bond and 2100 cm^{-1} corresponding to defective bonds of $Si-H_2$.

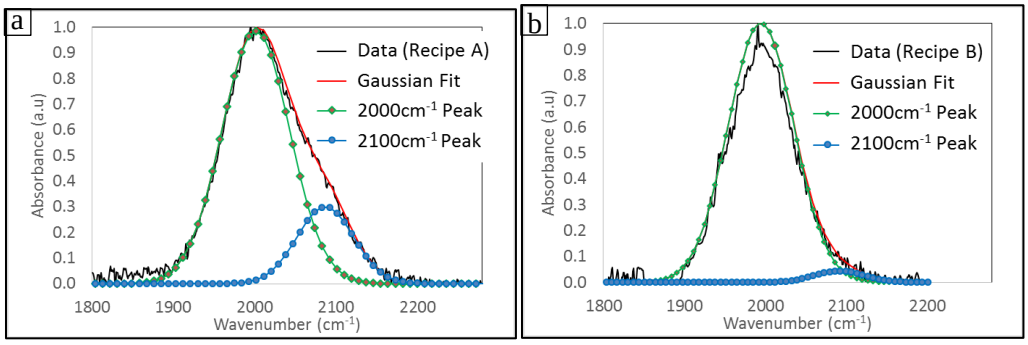

Fig 4.10 FTIR Gaussian fit and de-convoluted peaks of (a) recipe A; (b) recipe B

The FTIR peaks are shown in Fig 4.10 while Table 4.3 gives their microstructure parameter values (or ratio of the 2000 cm^{-1}/2100 cm^{-1} peaks). For these a-Si:H recipes, the film microstructure parameter corresponds to 3.3 for recipe A and 36 for recipe B. Expectedly, it was found that H_2 dilution in SiH_4 gas mix during the deposition process suppressed the formation of defective $Si-H_2$ bonds in the a-Si:H microstructure of recipe B leading to a factor of 10× better film quality (less defective) than recipe A.

In addition, transient measurements (additional details on the transient measurements are given in sections 6.5.2 and 6.5.3) of a fabricated *p-i-n* diode using both recipes as the intrinsic layer confirmed recipe A is more defective with density of states at the Fermi level calculated as 2.53×10^{17} cm^{-3} while that of recipe B was found to be 5.54×10^{16} cm^{-3}.

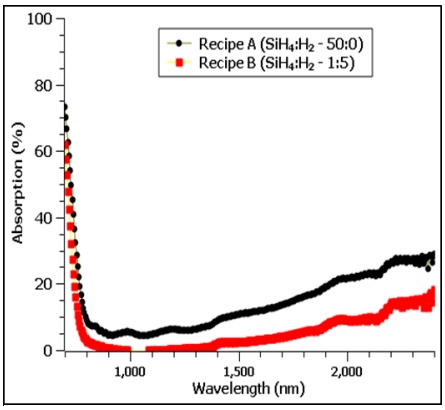

Fig 4.11 Absorption spectra of coated ZnO NWs using a-Si:H coating recipes with different hydrogen dilution showing increased IR absorption in Region III

Absorption spectra of recipe A and recipe B coated ZnO NWs are shown in Fig 4.11 while the table summarizing their parameters is shown in Table 4.3. It is obvious from Fig 4.11 that recipe A corresponding to the more defective a-Si:H material absorbs more than recipe B. At a wavelength of 2.3 µm, the difference in absorption is ~ 83%. This difference in absorption is also mostly in Region III. The increase in defect density between both materials is mostly within the band gap (Fig 4.11) thus contributing more towards Region III infrared absorption.

Table 4.3 FTIR Microstructure parameter of a-Si:H recipes

	Recipe A	**Recipe B**
SiH_4:H_2 ratio	50:0	1:5
FTIR Microstructure	3.3	36
Density of states ($N(E_F)$) (cm^{-3})	2.53×10^{17}	5.46×10^{16}
Absorption at 2.3µm (%)	27.5	10

The defect mediated infrared absorption is further supported by the optical absorption results shown in Fig 4.12. The results show that within a strong scattering regime, changes in a-Si:H thickness and ZnO NW length greatly affect the intensity of absorbed infrared radiation.

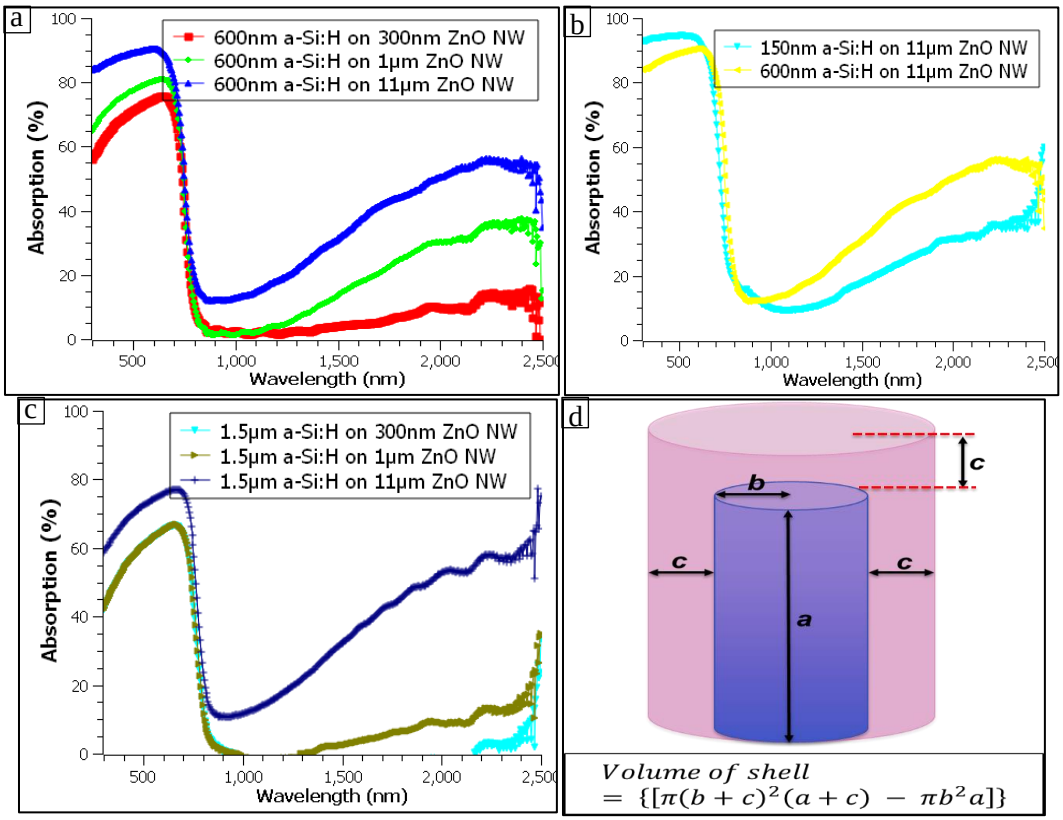

Fig 4.12 Absorption spectra (a) Varying ZnO NW length; (b) Varying a-Si:H thickness; (c) Showing the limits of increasing a-Si:H thickness on shorter ZnO NWs; (d) Schematic illustration of changing shell volume with (a) or (b)

For the same a-Si:H recipe with its characteristic density of defect states determined by the its H dilution, increasing the thickness of coated a-Si:H film or the aspect ratio on which the film is coated increased the number of defects in the resulting material system. In Fig 4.12a with a uniform thickness for the a-Si:H shell of 600 nm, increasing the length of the ZnO NWs from 300 nm to 11 µm led to an increase in the volume of the shell coated from ~ 1.38 x 10^{-12} cm^3 to 1.75 x 10^{-11} cm^3. This one order of

magnitude increase in volume of coated a-Si:H shell translates to a similar increase in the number of defects. Similarly, increasing the thickness of the a-Si:H shell (Fig 4.12b) from 150 nm to 600 nm while keeping the NW length constant at 11 μm also led to increase in the volume of a-Si:H coated from ~ 1.84 x 10^{-12} cm^3 to 1.75 x 10^{-11} cm^3. This order of magnitude increase in a-Si:H volume also translates to a similar increase in the number of defects. These increase in the number of available defects impacts the infrared absorption. The increase in both techniques follows from the same effect they have on the number of available defects and is in agreement with the model presented in Fig 2.6.

Fig 4.12c is an optical verification of Fig 3.10 where it was established that the NvF factor plays a role in both the enhancement in effective length and 3-D morphology. Regardless of the number of available defects due to the increased thickness of a-Si:H, the degradation of the 3-D morphology by such increased a-Si:H thickness without a commensurate increase in ZnO NW length will reduce the scattering from the structure and dampen the infrared absorption.

4.3.2 Hydrogen Evolution

For a-Si:H, hydrogen can be evolved from a combination of trapped molecular hydrogen [96] and broken Si-H bonds [16] by thermal annealing. The anneal temperature provides the energy required to break these bonds and release the hydrogen. Due to the considerable binding energy of interstitial hydrogen, energies lower than the bond energies of Si-H bonds are often sufficient to release hydrogen from a Si-H bond into an interstitial site [16]. The interstitial atomic hydrogen could then combine with other released atomic hydrogen and evolve as molecular hydrogen.

In addition to hydrogen evolution, annealing a-Si:H materials also leads to a redistribution of hydrogen within the material [16]. The anneal leaves the material more defective. FTIR microstructure analysis of annealed a-Si:H samples shown in Table 4.4 shows the correlation between annealing temperature and a-Si:H microstructure. This is anticipated as higher annealing temperatures lead to

higher out-diffusion of hydrogen due to more thermal energy available to break weak Si and H containing bonds. Defect creation by annealing causes more mid-gap states to be formed as more dangling bonds are exposed thus making the material more defective (Table 4.4) and leading to more absorption expected in Region III.

Table 4.4 FTIR Microstructure Parameters of a-Si:H Degradation with 9 Hours Annealing

	150°C (as dep)	220°C	300°C	380°C
FTIR Microstructure Parameter	3.3	2.7	2.0	1.5

When subjected to varying vacuum annealing temperatures for ~ 9 hours, a-Si:H coated materials show an increase in infrared absorption with increase in annealing temperature as shown in Fig 4.13a. This increase in absorption occurs mostly in Region III in agreement with the initial hypothesis and results, and is caused mainly by increase in mid-gap defect concentration due to the annealing. The absorption enhancement factor (β) (defined as difference between the measured absorption intensity of a post-processed sample and the initial as-dep absorption intensity at the wavelength of interest) calculated at 2.3 μm tracks the degradation as obtained from the FTIR microstructure parameter until it saturates at 300°C (Fig 4.13c). At 300°C, the infrared absorption intensity at 73 % is already high and the limitation to further absorption greatly shifts to the 3-D structure's reflectivity as can be deduced from its transmission result (Fig 4.13b). The transmitted intensities of the as-deposited sample and sample annealed at a temperature of 220°C showed higher transmission at infrared wavelengths above 2 μm. The higher transmission of the as-deposited and 220°C annealed samples indicate there is still room for further absorption as some incident photons are passing through the material unabsorbed. This is in contrast to transmitted intensities of the 300°C and 380°C annealed samples which compares with the machine noise level indicating saturation of absorption (Fig 4.13b). This result also indicates no

further absorption is possible since no significant photons can be detected passing through the sample unabsorbed.

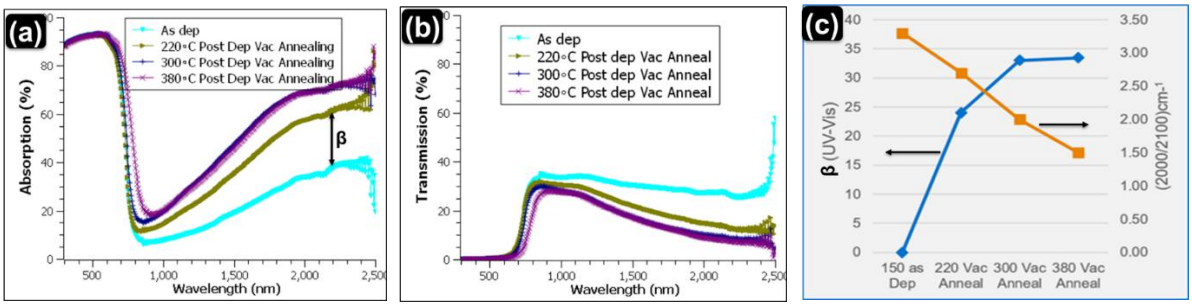

Fig 4.13 Effect of annealing on defect concentration and annealing of 3-D a-Si:H coated ZnO NW samples. (a) Absorption spectra of as dep, 220°C, 300°C and 380°C post annealed samples; (b) Transmission spectra of (a); (c) Absorption enhancement factor (β) at 2.3µm wavelength and FTIR microstructure parameter showing strong correlation of materials' defect profile

4.3.3 Doped Amorphous Silicon

Varying the number of defects in the manners described in previous sections however maintains the distribution of the defects leading to a preservation of the general shape of the absorption curve. Doping a-Si:H materials however creates additional defects and changes its defect distribution [16], [97], and would lead to a change in the shape of the absorption curve. The addition of dopants to the a-Si:H matrix increases the density of states in the bandgap and is distributed as shown in Fig 4.14 [16]. The density of states distribution shows the presence of a significant amount of tail states. This increased density of tail states which is induced by doping and distributed according to the type of dopant involved, also causes increased levels of gap states as a consequence of the modified 8 – N rule [16], [77]. Using deep level transient spectroscopy (DLTS), Yongchang *et al.* found that the tail states of phosphorus doped a-Si:H materials extends by ~ 0.45eV into the band gap from the conduction band edge [97]. Similarly, for boron doped samples, the tail states extend towards the band gap from the valence band edge by a similar energy [16]. The increased density of tail states will then impact the

absorption in Region II of Fig 4.11 which will eventually lead to a change in the slope at the Region I and II boundary. In addition to increased density of tail states, the energy range over which these additional states are distributed will lead to a reduction in the minimum energy required for such tail-state – to – tail-state transition. This will then enable tail-state – to – tail-state transitions or tail-state – to – conduction-band transitions in the energy range between 0.7 eV to 1.5 eV corresponding to 800 nm – 1.7 μm.

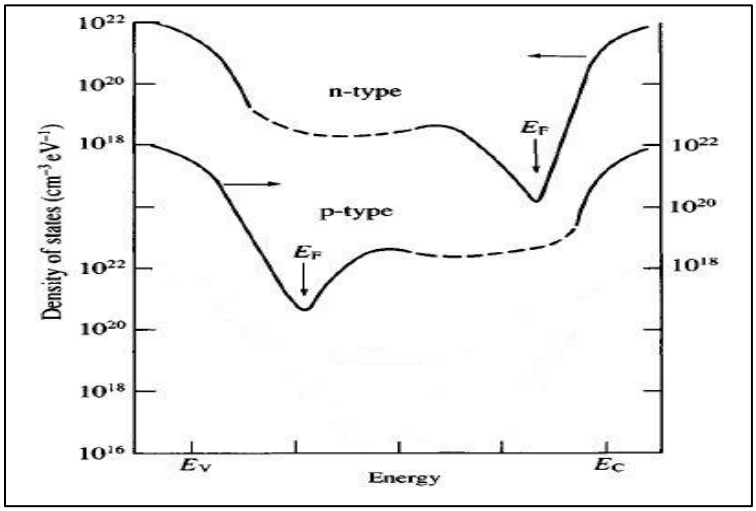

Fig 4.14 Density of states distribution of doped a-Si:H [16]

To verify this, different boron doped a-Si:H materials were developed by varying the diborane (B_2H_6) flow rate. As shown in Table 4.5, adding dopant gas (B_2H_6 for p^+) to SiH_4 gas flow leads to varying conductivity of the doped a-Si:H film. Carrier concentration of such films can be estimated as a correlation of its tail state defects. The relationship between conductivity and carrier concentration is given by equation 4.2 where σ is the material conductivity, n is the carrier concentration, e is the electronic charge and μ is the drift mobility. Conductivity results of the boron doped a-Si:H films as given in Table 4.5, show about one order of magnitude increase in the conductivity of the doped samples with increasing B_2H_6 flow and 10^3-10^4 difference with the undoped a-Si:H material. The increase in

conductivity of the doped samples as B_2H_6 concentration increases indicates increase in doping which leads to increase in tail state defect concentration.

$$\sigma = ne\mu \qquad 4.2$$

To further verify this, the dopant concentration, which is a measure of the density of defect states of the doped material was calculated. The variation of defect density with doping level in doped a-Si:H materials is given by equation 4.3 where N_D is the defect density of states or dopant concentration and C_g is molecular concentration of the dopant in the gas phase [16]. The dopant concentration given in Table 4.5 shows a clear increase in the defect concentration of the boron doped a-Si:H films as the flow rate of B_2H_6 is increased.

$$N_D = 3 \times 10^{19} C_g^{1/2} \qquad 4.3$$

Table 4.5 Electronic and Defect Properties of Boron Doped a-Si:H Films

Material	**Dopant Flow (sccm)**	**Conductivity $(\Omega cm)^{-1}$**	**Estimated Carrier Concentration (cm^{-3})**	**Dopant Concentration (cm^{-3})**
a-Si:H	B_2H_6/PH_3 - 0	1.72×10^{-9}	2.66×10^{10}	-
p+ a-Si:H	B_2H_6 - 10	4.76×10^{-6}	7.43×10^{13}	8.32×10^{17}
	B_2H_6 – 30	8.33×10^{-6}	1.35×10^{14}	1.34×10^{18}
	B_2H_6 - 50	1.64×10^{-5}	2.55×10^{14}	1.63×10^{18}

When ZnO NWs were coated with boron doped a-Si:H thin film, infrared absorption increases, further confirming the defect mediated absorption with changing defect density. Absorption spectra of ZnO NWs coated with the various boron doped a-Si:H shell is shown in Fig 4.15. From the figure, it can be seen that as boron doping increases (Table 4.5), Region II absorption increases. This increase in absorption between 800 nm – 1.7 μm leads to a softening of the falling slope and shifts the minimum

absorption from a wavelength of around 800 nm for the undoped a-Si:H shell corresponding to the energy difference of the valence and conduction band tails, to wavelengths around 1.5 µm, 1.6 µm and 1.7 µm for recipes with B_2H_6 flow rates of 10, 30 and 50 sccm respectively, corresponding to the lowering energy difference between the valence and conduction band tail states of the doped samples. This lowering of the energy difference between the valence and conduction band tail states is due to the broadening of the tail states by the addition of more states in the band tails through doping (Fig 4.15b).

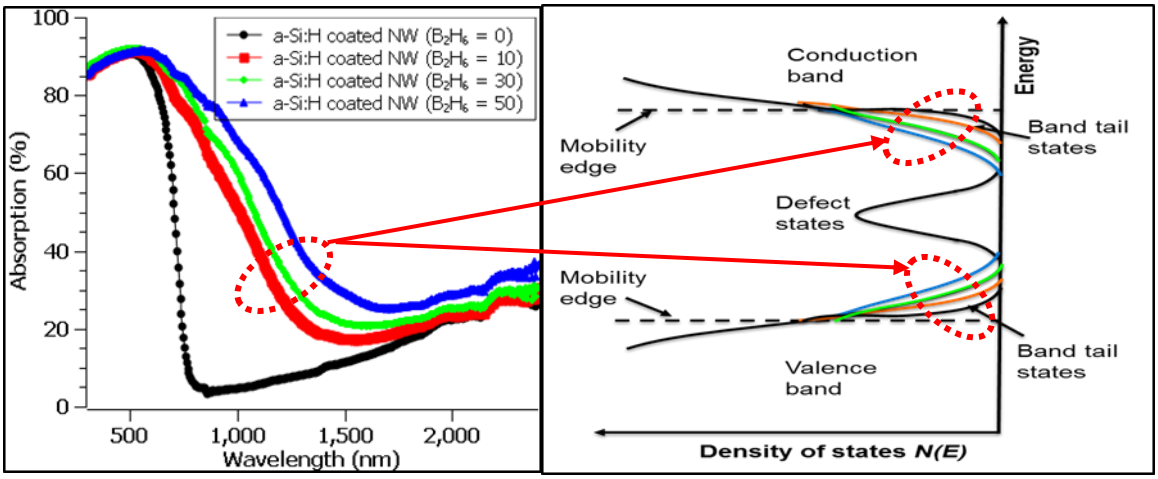

Fig 4.15 Absorption spectra of various boron doped a-Si:H coated ZnO NWs with a representation of their changing tail state distribution

4.4 Summary

This chapter studied the optical properties of hybrid 3-D structures comprising of ZnO NW core and a-Si:H shell. The optical absorption results of this type of 3-D structure show that the material morphology greatly increases the effective thickness of the coated shell thereby leading to interesting optical characteristics. In the case of a-Si:H coated ZnO NWs, infrared absorption was observed. The origin of the infrared absorption was also studied. The infrared absorption in this material system was found to be largely driven by defects within the a-Si:H coating. Control of the infrared absorption has

been achieved by hydrogen dilution, annealing and doping which all target and change the defect concentration and distribution of the a-Si:H coating. While annealing and doping increased the defect concentration and distribution leading to increased infrared absorption, hydrogen dilution reduced the defect concentration of the amorphous silicon material leading to reduced infrared absorption. In addition to these, the NvF ratio was also found to be an important control parameter that can be used to control the infrared absorption from the 3-D material structures by increasing or suppressing the scattering obtainable which directly affects the enhanced effective thickness of the material. This could either increase the amount of defect available or decrease it which will in turn impact on the intensity of infrared absorbed.

Chapter 5
Infrared Photoconductor

In Chapter 4, the optical properties of 3-D material systems were presented. This chapter introduces an approach to exploit the 3-D enabled infrared absorption of a-Si:H based materials system into a photodetector. The infrared photoconductor (also called co-planar infrared detector) presented here is simple to fabricate and stable in ambient environments over extended periods. Results and optimizations of the infrared photoconductor will be presented.

5.1 Mask Design and Development

To fabricate an infrared photoconductor, masks are needed. These masks consist of a set of 3 masks/layers required for the ZnO NW pattern, a-Si:H island pattern and contact metal pattern. A screenshot of the mask is shown in Fig 5.1. A gap was intentionally included in the photoconductor between the NW edge and the contacts.

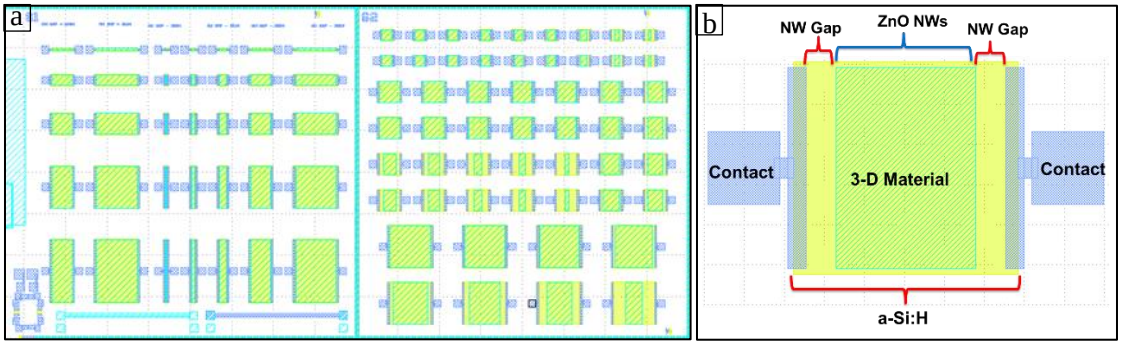

Fig 5.1 Screenshots of the (a) mask set needed for infrared photoconductor fabrication and (b) Zoomed image of a photoconductor showing the NW Gaps

5.2 Infrared Photoconductor Fabrication

To fabricate the infrared photoconductor, rf sputtered ZnO seed layer was deposited on RCA-1 cleaned glass substrate. The seeded substrate was then immersed into a hydrothermal bath containing

25 mM aqueous solutions of zinc nitrate hexahydrate ($Zn(NO_3)_2 \cdot 6H_2O$, Sigma Aldrich) and hexamethylenetetramine (HMTA) ($C_6H_{12}N_4$, Sigma Aldrich) maintained at an average temperature of about ~85°C as described in Chapter 3. The grown ZnO NWs were cleaned, dried and then lithographically patterned and etched with HCl to create the NW islands. Next, the NW etched sample was placed in a 13.56 MHz PECVD system for the deposition of conformal a-Si:H film at 150°C. The sample was then unloaded from the PECVD system and loaded into a sputtering system for the deposition of 150 nm aluminum contact. The use of Al as the contact instead of a TCO is obvious from the design of the device where the contacts do not interfere or block radiation onto the absorber. The Al metal was then patterned and etched. Schematic and optical micrographs of the completed devices are shown in Fig 5.2

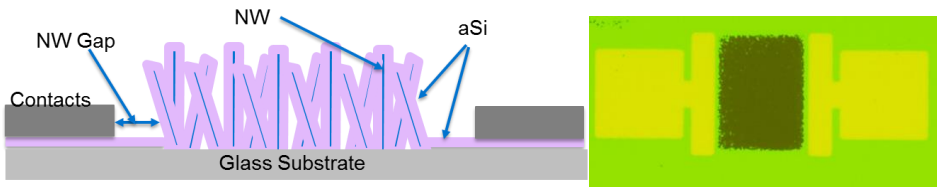

Fig 5.2 Schematic and optical micrograph of a completed 3-D infrared photoconductor

5.3 3-D Infrared Photoconductor Results

5.3.1 Dark Current Optimization

As given in Section 2.3, dark current of photoconductors play an important role in determining its signal to noise ratio otherwise called ON/OFF ratio. As shown in Table 4.1, exposure to hydrogen plasma increases the conductivity of ZnO material by ~ 10 orders of magnitude. The deposition of a-Si:H coating on ZnO NWs will expose the underlying ZnO NWs to hydrogen plasma from SiH_4 decomposition which will increase its conductivity. A high ZnO conductivity will impact the dark current of the eventual photoconductor as the ZnO NWs will create an alternate path for current flow from the injection contact to the collection contact thereby degrading its ON/OFF ratio. Initial devices

fabricated with a shadow mask confirmed this phenomenon as the devices had very high dark currents after fabrication.

The 3-D photoconductor can be divided into an equivalent circuit showing 2 resistance regimes in parallel as shown in Fig 5.3a. In a disordered NW network such as those obtained from hydrothermal synthesis, there is a high probability that the network of NWs could connect to each other and form a conducting path when exposed to hydrogen plasma prior to a-Si:H coating. This increase in conductivity (or reduction in resistance) reduces the equivalent resistance of the NW/a-Si:H stack and leads to high current conduction.

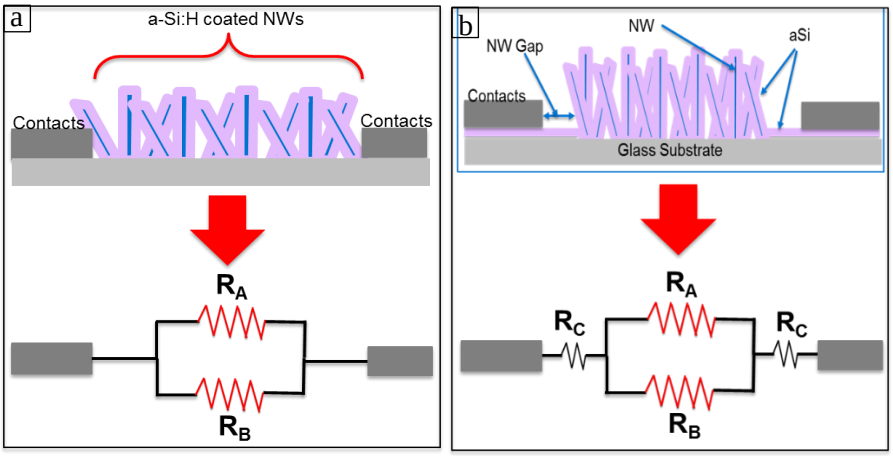

Fig 5.3 (a) Equivalent resistance of 3-D photoconductors; (b) Equivalent resistance of 3-D photoconductors with an intentional gap between contacts and NW edge

Unlike photodiodes, photoconductors lack a reverse biased suppression of dark current. They work by current injection and current flowing through the semiconductor depends on its resistivity. Therefore to overcome this problem, an intentional gap was created between the ZnO NWs and contact edge as shown in Fig 5.3b. This gap creates a limiting resistance to current flow from all possible conducting channels. It also isolates the contribution from ZnO from being measured such that the measured

electrical response will primarily be due to the a-Si:H coating. This latter function serves as additional proof that the observed infrared response is primarily due to the a-Si:H material (see section 4.2).

Fig 5.4a shows the dark current density of planar and 3-D photoconductors. Both devices have dimensions of 250 µm x 250 µm with the 3-D photoconductor incorporating 25 µm gap at its ends. The figure shows that dark current of 3-D photoconductors is only one order of magnitude higher than those of planar photoconductors. The relatively low dark currents of the 3-D photoconductors are due to the deliberate gap created between the NWs and contacts. Fig 5.4b shows the dependence of dark current on the size of the NW gap. As shown, the longer the gap, the lower the dark current arising from the higher resistance such increased gap will add to the overall equivalent resistance of the device. However, increasing the gap while maintaining the same outside device dimensions leads to reduced NW coverage and its attendant reduced infrared absorption. In addition, increasing the gap leading to increased equivalent resistance also leads to higher resistance to flow of infrared generated current especially at the gap area whose resistance does not similarly change due to its poorer infrared response without a NW backbone.

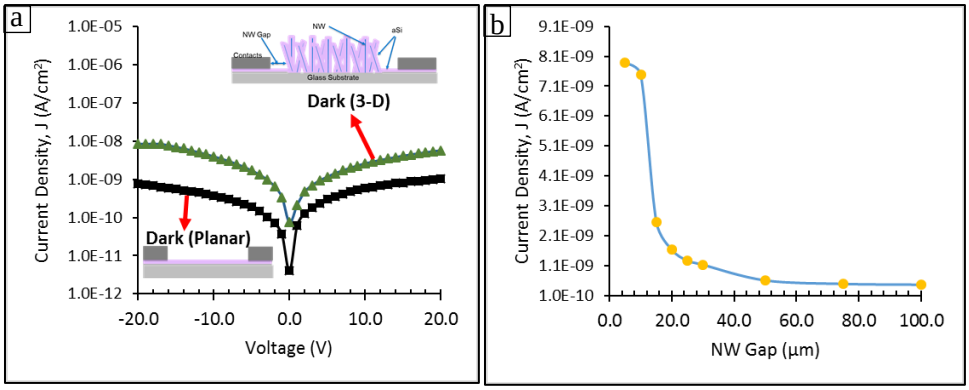

Fig 5.4 (a) Dark current density of planar and 3-D photoconductor; (b) Dark current density change with NW gap at 2V bias for 250µm x 250µm 3-D photoconductor

5.3.2 Infrared Detection Results

Infrared response of the 3-D infrared photoconductor was primarily obtained using a 1.55 µm IR LED source and occasionally using a commercially available 50W heat lamp. The current controlled IR LED has a center frequency at 1.55 µm and was locally made for communication signal research. The absence of a power meter sensitive at such wavelength means quantitative power data from the LED cannot be obtained. The current bias however can effectively be used to maintain uniform power irradiation across devices. An infrared sensitive card further confirms infrared output and is used to help with focusing the LED onto the sample. The heat lamp on the other hand is a commercially available infrared light source used in pet houses and poultry farms. The spectra of the heat lamp shown in Fig 5.5 shows the heat lamp has a peak intensity in the visible which tails off into the infrared region. A combination of 2 crystalline silicon substrates and a boron doped a-Si:H film served as a visible light filter to block visible light frequencies from the heat lamp from reaching the device under test and ensured only the infrared components of the spectrum irradiates the device under test. For the 3-D photoconductor, infrared results were primarily obtained using the 1.55 µm IR LED. Unless otherwise stated, the results reported here are from the 1.55 µm IR LED source.

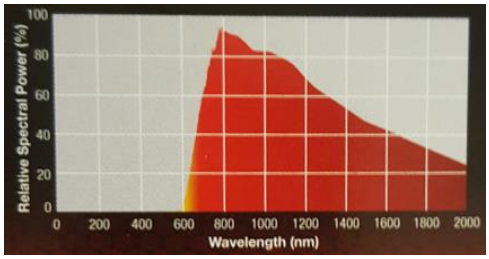

Fig 5.5 Heat lamp spectra used for infrared irradiation [98]

Fig 5.6a shows infrared response measured from a 250 µm x 250 µm 3-D photoconductor using a 1.55 µm LED illumination. As shown in the figure, 3.2 x 10^2 ON/OFF ratio were obtained with infrared radiation. Fig 5.6b shows the photoconductor's response as the infrared LED source is pulsed by turning its supply power ON and OFF. The switching action of the source LED is clearly translated into a

similar switching action of the current. This demonstrated the effectiveness of 3-D hybrid photoconductors of a-Si:H coated ZnO NW in detecting infrared radiation. A comparison of the infrared response of planar and 3-D photoconductors with 1.55 µm illumination is shown in Fig 5.6c for 500 µm x 250 µm device. As the length of the device increased from 250 µm (Fig 5.6a) to 500 µm (Fig 5.6c) while keeping the width constant at 250 µm, dark current decreased slightly as is characteristic of photoconductors. This response also caused a slight decrease in infrared current due to longer channel resistance to current collection. This result implies photoconductors with longer width would be preferred. The planar photoconductors also show some infrared response albeit lower. The planar device results indicates the defective a-Si:H material absorbs some infrared radiation but is not as sensitive compared to 3-D diodes.

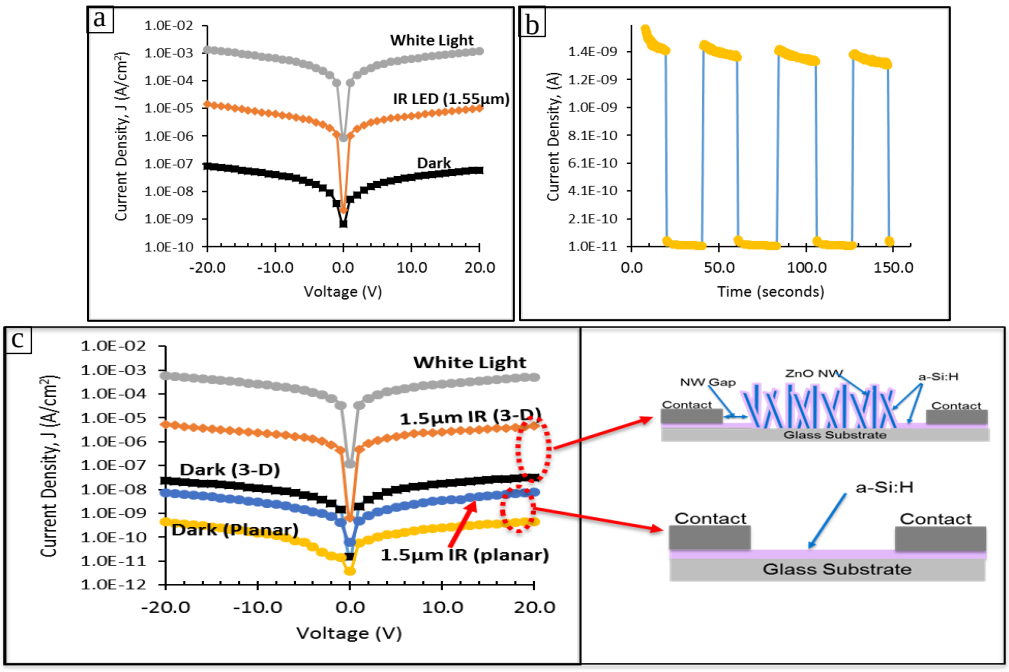

Fig 5.6 (a) IV characteristics of 3-D infrared photoconductor clearly showing 2 orders of magnitude ON/OFF ratio with infrared illumination; (b) Pulsed current response of 3-D photoconductor with time in response to pulsed infrared LED irradiation at 10V bias; (c) Infrared response of planar and 3-D photoconductors

The response of 250 µm x 250 µm planar and 3-D photoconductors under heat lamp illumination is shown in Fig 5.7. As seen from the figure, the 3-D photoconductor shows 2 – 3 orders of magnitude of ON/OFF ratio while the planar device shows less than one order difference in agreement with results from the 1.55 µm IR LED shown in Fig 5.6c. The current due to heat lamp on the planar device overlap with the dark current of the 3-D device. Despite this relatively high dark current, significant increase in illuminated current is still observed with heat lamp radiation.

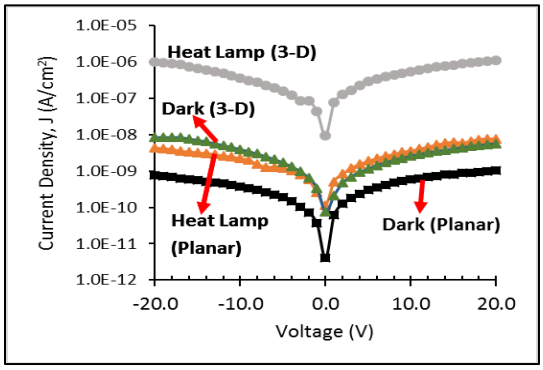

Fig 5.7 IV characteristics of planar and 3-D photoconductors in response to heat lamp radiation

5.4 Summary

This chapter demonstrated an approach to exploiting the infrared absorption properties of 3-D materials systems made up of ZnO NW core and a-Si:H shell. To do that, the mask design and process development of the proposed 3-D photoconductor device were carried out. Fabrication and optimization of 3-D infrared photoconductors were developed and presented. The dark currents of the photoconductors were reduced by the addition of a NW gap to increase the effective resistance of the channel and isolate the ZnO NWs whose conductivity was increased by hydrogen plasma during a-Si:H coating process. Infrared absorption using the 3-D photoconductors were also presented and the effect of the introduced NW gap was evaluated. ON/OFF ratio of 3.2 x 10^2 were achieved using a 1.55 µm LED whose center wavelength falls around the least sensitive region of the 3-D material system implying that a higher response is achievable at longer wavelengths.

Chapter 6
Infrared Photodiodes

In this chapter, application of 3-D material system to fabricate *p-i-n* photodiodes for infrared detection is developed as a second approach to exploiting the infrared properties of 3-D a-Si:H coated ZnO NWs. Discussion on mask design and process development is presented in Section 6.1 while Section 6.2 presents the 3-D diode fabrication process. I-V results are presented in Section 6.3 where reasons for the observed infrared response are presented. Section 6.4 presents results and discussion of TCO absorption, and optimizations carried out to minimize its impact. Analysis of the dark currents of 3-D photodiodes are presented in Section 6.5. The discussion in this section includes systematic experimental design to understand and isolate the main factors contributing to high dark currents in 3-D photodiodes and to develop methods to minimize their impact. Section 6.6 presents results of infrared measurements done using a 1.55 µm IR LED and a 50W commercially available heat lamp while in Section 6.7, external quantum measurements and analysis are presented.

6.1 Mask Design and Process Development

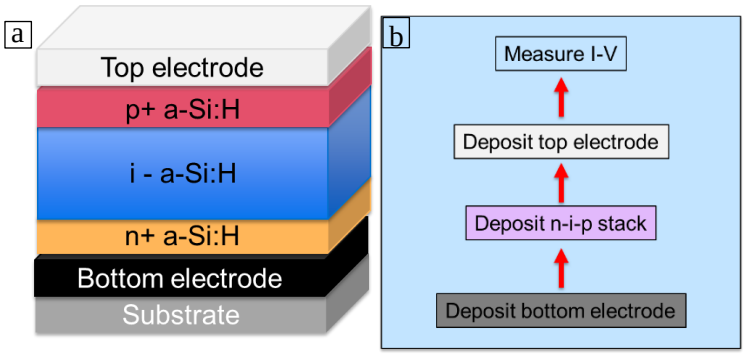

Fig 6.1 (a) Schematic cross section of a typical photodiode; (b) Typical fabrication flow process flow for this photodiode

A simple schematic cross section of a typical photodiode is shown in Fig 6.1a while the typical process flow for this photodiode fabrication is given in Fig 6.1b. This initial device was realized with

a shadow mask for depositing the top contact while the underlying layers are left connected. Such simple structures could help with initial process diagnostics and experimentation, and provide useful feedback for the mask design process.

To design a set of masks for the photodiode fabrication, acceptable fabrication process flow has to be conceived. The conception of this process will take account of the intended substrates, the materials that will be needed, the growth conditions of these materials such vacuum, solution and temperature requirements, the post-growth processes for these materials such as etching type (dry or wet), etching solutions and selectivity, connected or standalone diode layouts or any unique device structures needed. These considerations will inform the deployment of specific etch stop layers in the mask(s) or the sequence of growth, among others things, which will be important input parameters for mask design. Using the simple schematic fabrication process flow shown in Fig 6.1b as a test, the tentative processes could be tested for consistency and specific process variations such as full or partial mesa etching could be examined. Geometry independent optimizations such as doped layer thickness variations and other optimizations such as post growth processing, etch selectivity and impact of material growth technique could also tested. While not exhaustive, the results of these tests could then serve as input parameter to the photodiode mask design process.

Photodiode masks designed for 3-D infrared diode fabrication is shown in Fig 6.2. The set of 5 masks/layers was designed to realize different device structures employing 3 – 6 process steps. Table 6.1 gives the lithographic steps and mask sequence for the fabrication of the different device structures. The substrate floor planning and process summaries are provided in Appendix A and Appendix B respectively. For all process variations, planar and 3-D photodiodes can be fabricated on the same substrate in a single process run. This configuration enables side by side comparison since both types of devices will be exposed to the same conditions.

The photodiode fabrication masks were designed using K-Layout Editor and printed with emulsion on mylar substrates. The transparent mylar substrate was eventually glued unto a transparent glass holder for ease of handling. Device structures included in the mask include unpassivated photodiodes, passivated photodiodes, horizontal structured photodiodes, and SiN_x isolated photodiodes.

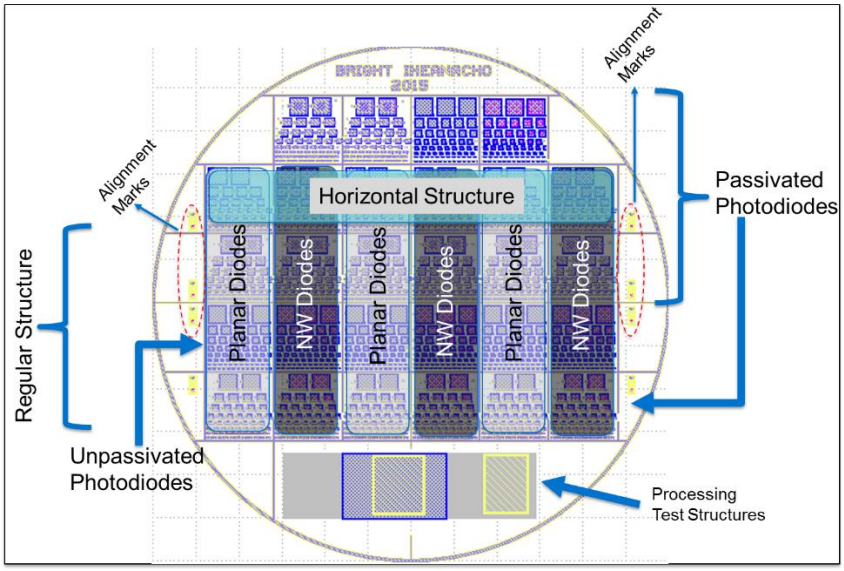

Fig 6.2 Photodiode Mask Set

Table 6.1 – Sequence of Masks for the Different Photodiode Device Structures

Process	Unpassivated Photodiode	Passivated Photodiode	SiN_x Isolated Photodiode	Horizontal Isolation Photodiode
Mask 1	Bottom Contact	Bottom Contact	NW Etch	Bottom Contact
Mask 2	NW Etch	NW Etch	Bottom Contact	NW Etch
Mask 3	Mesa	Mesa	Mesa	Mesa
Mask 4	-	Via	Via	Mesa
Mask 5	-	Metallization	Metallization	Via
Mask 6	-	-	-	Metallization

6.2 IR Photodiode Fabrication

As discussed in Chapter 4, infrared response was observed with 3-D materials comprising of ZnO NWs which serve as the enabling backbone for the 3-D structure and a-Si:H which is the main absorber material. Thus, infrared photodiodes hereafter will be referred to as hybrid 3-D diodes using ZnO NW core and a-Si:H shell layers.

As given in Table 6.1, the different photodiode structures require different levels of fabrication complexity from the simplest 3 mask 'unpassivated photodiode' to the most complex 6 mask 'horizontal isolated photodiode'. The different levels of complication also mirror the challenges that were encountered. Here, the fabrication and results of unpassivated photodiodes are given as a representation of the process and characteristics of 3-D infrared diodes. The other structures will be introduced as needed during the discussion on dark current optimization.

As stated in section 6.1, the fabrication processed developed is the same for both planar diodes and 3-D diodes and ensured both types of diodes are present in the same substrate at a single process run. The fabrication process flow is shown in Fig 6.3. Following the deposition of the bottom electrode on RCA-1 cleaned glass substrates, photolithographic patterning and etching was carried out. Next, rf sputtered ZnO seed layer was deposited on the bottom electrode. The seeded substrate was then immersed into a hydrothermal bath containing 25 mM aqueous solutions of zinc nitrate hexahydrate ($Zn(NO_3)_2{\cdot}6H_2O$, Sigma Aldrich) and hexamethylenetetramine (HMTA) ($C_6H_{12}N_4$, Sigma Aldrich) maintained at an average temperature of about ~85°C. Details of the NW growth and optimization process had earlier been given in Chapter 3. Following the hydrothermal process, the grown ZnO NWs were cleaned, dried and then lithographically patterned. The patterned sample was etched with HCl.

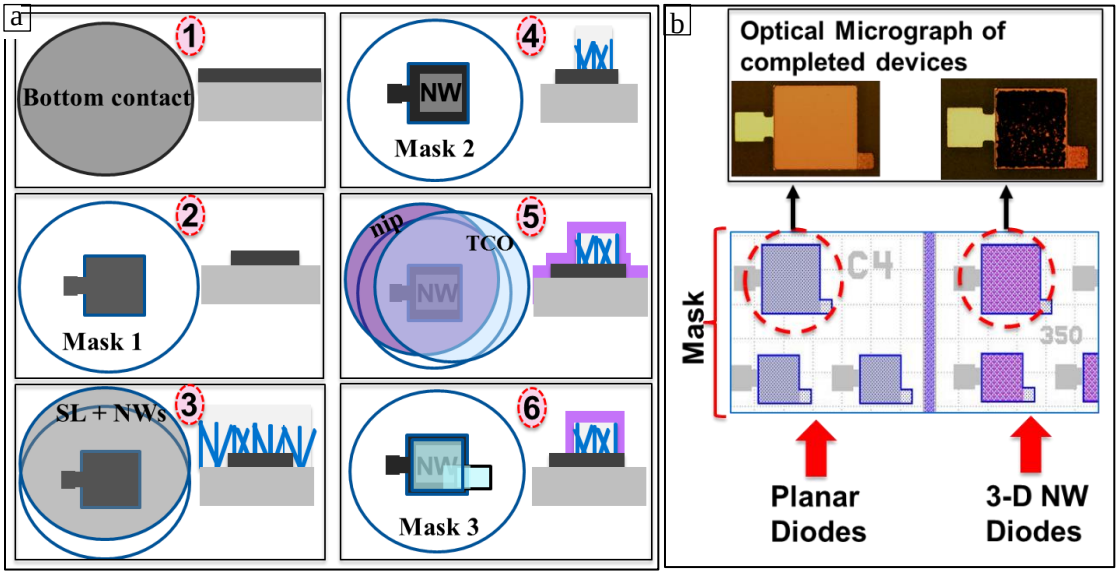

Fig 6.3 (a) Schematic process flow for the fabrication of (unpassivated) 3-D infrared diodes; (b) Snapshot of the photodiode mask layout and optical micrograph of completed diodes

ZnO NWs were grown on the entire seeded substrate. To ensure both planar and 3-D diodes are obtained on the same substrate, the NW etch mask was designed to protect NWs on the 3-D diode areas and etch NWs on the planar section (Fig 6.3b).

Next, the sample was placed in a 13.56 MHz PECVD cluster system for the deposition of the *n-i-p* stack. 25 nm n^+ a-Si:H, 500 nm intrinsic a-Si:H and 25 nm p^+ a-Si:H were deposited without breaking vacuum at a temperature of 150°C. The eventual sample was unloaded from the PECVD system into a sputtering system for the deposition of 150 nm Aluminum-doped ZnO (AZO) as the top transparent conductive oxide (TCO). Lithography and etching of the AZO were done and the same patterns were used as a mask for a mesa etch down to the bottom contact to isolate each individual device. The schematic and SEM micrographs of the completed devices are shown in Fig 6.4.

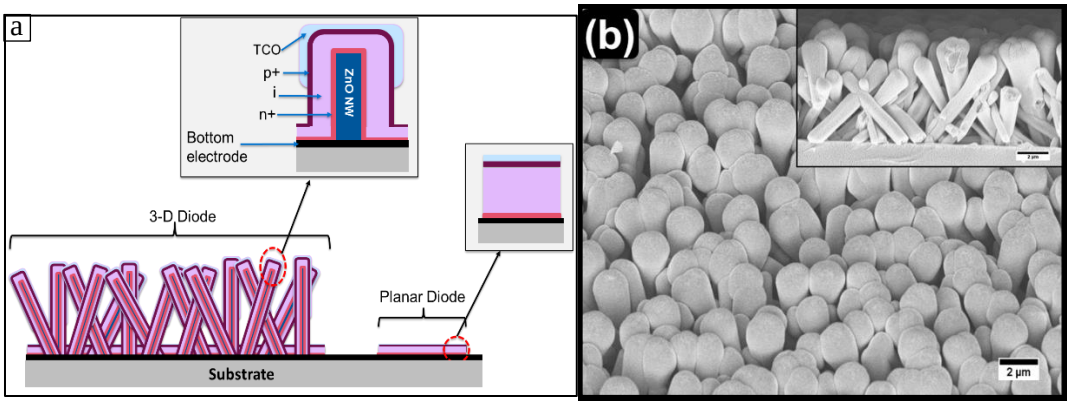

Fig 6.4 (a) Schematic illustration of a typically processed photodiode substrate showing 3-D infrared diodes and planar diodes and the different layers used; (b) SEM micrograph of a completed 3-D infrared diode (inset is a cross sectional SEM micrograph of (b))

6.3 Photodiode Results

I-V measurements of the fabricated diodes were done using a Keithley 4200 SCS Semiconductor Characterization System. Dark, light and infrared irradiated measurements were taken. Results of the infrared measurement will be presented in section 6.6.

Fig 6.5 shows the dark I-V characteristics of 350 µm x 350 µm unpassivated photodiodes fabricated on chromium (Cr) bottom electrodes. Further discussion on the choice of a bottom electrode will be presented in section 6.5.1. The 3-D diode fabricated alongside the planar diode showed good diode switching properties even though its dark current density is higher than its planar counterpart. The dark current density of the 3-D diodes show a higher reverse bias voltage dependence increasing over 3 orders of magnitude at higher reverse bias values of 5V than the planar diodes. In addition, the planar diode fabricated on a planar-diode-only-bottom-electrode (i.e no prior NWs were grown and no 3-D diodes exist alongside the planar diodes on the same substrate) and the one fabricated alongside 3-D diodes in a combined process as describe in section 6.2 mirror each other. I-V results of the planar only and combined dual process as developed in section 6.1 is shown in Fig 6.5.

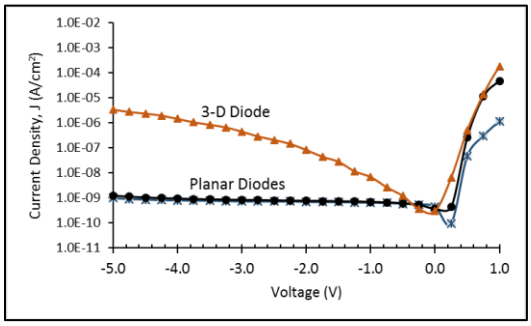

Fig 6.5 Dark Current Density (J, A/cm^2) of a planar diode from all-planar diode substrate (cross hair markers), planar diode from a combined planar and 3-D diode substrate (black circular markers) and 3-D diode from same combined planar and 3-D diode substrate (triangular markers)

Table 6.2 Summary of diode properties shown in Fig 6.5

	Planar Diode (Planar Only Substrate)	Planar Diode (On Combined Substrate	3-D Diode (On Combined Substrate)
Dark Current Density @ -2V (A/cm^2)	6.9 x 10^{-10}	7.8 x 10^{-10}	8.2 x 10^{-8}
IR (1.55µm) Current Density @ -2V (A/cm^2)	-	8.2 x 10^{-10}	1.0 x 10^{-7}
ON/OFF Ratio	-	1.1	1.3
Ideality Factor, n	1.67	1.97	2.61
Saturation Current Density, J_0 (A/cm^2)	2.0 x 10^{-13}	4.0 x 10^{-12}	2.0 x 10^{-10}

Table 6.2 shows the properties of the diodes extracted from their IV measurements. The ideality factor for the planar diodes are less than 2.0 while it is 2.61 for the 3-D diodes. The high ideality factor suggests a high carrier recombination especially in the 3-D diodes which could impact its shunt resistance (R_{shunt}) leading to high dark currents. The dark current density at -2V reverse bias of both planar diodes are identical at 6.9 x 10^{-10} A/cm^2 and 7.8 x 10^{-10} A/cm^2 respectively while it is 2 orders of magnitude higher for the 3-D diodes at 8.2 x 10^{-8} A/cm^2. This portends a serious issue since the

signal to noise ratio of any potential infrared gain could be reduced by ~ 2 orders of magnitude regardless of infrared intensity. An infrared radiation from a 1.55 μm LED shows ON/OFF ratios of 1.1 and 1.3 respectively for the planar and 3-D diodes. The low ON/OFF ratio obtained from the 3-D diode indicates its high dark current may be limiting the ON/OFF, and suggests higher gain could be achieved if the dark current is further reduced.

Also, equally important is the impact of the TCO in minimizing the amount of infrared radiation that actually interacts with the absorber layer. Minimizing the absorption of infrared in the TCO which will ensure maximum incident radiation reaches the absorber layer.

6.4 TCO Absorption and Alternative Contact

Aluminum doped Zinc Oxide (AZO) is a popular Transparent Conducting Oxide (TCO) currently used for silicon based photonic devices. Its appeal is its high conductivity and high transparency in the visible.

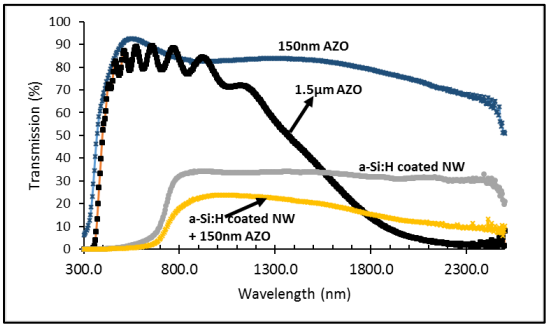

Fig 6.6 Transmission results of AZO films in the infrared region

While AZO is transparent in the visible, it absorbs in the infrared due to free carrier absorption. Fig 6.6 shows the transmission results of different AZO materials. As shown in the figure, transmission of AZO decreases with infrared radiation. At a thickness of 150 nm, AZO transmission reduced by 20 % from an average of 85 % in the visible to 68 % at 2.3 μm infrared wavelength, and reduced further by 98 % to 1.7 % when AZO thickness is increased to 1.5μm. When AZO was coated on a 3-D a-Si:H

coated ZnO NW, its transmission decreased by 69 % from 30.4 % to 9.3 % at a wavelength of 2.3 µm. These show AZO absorbs infrared radiation and will significantly decrease the amount of infrared radiation passing through it to the IR absorber material.

To minimize the effect of AZO absorption, several approaches could be used. For example, top AZO could be thinned down since absorption is dependent on thickness. Fig 6.7a shows the transmission results of thin AZO films. As the thickness of AZO is reduced from 150nm to 50nm, transmission increases from 62 % to 84 % at 2.3 µm wavelength. However, etching thin AZO is a challenge because the thin material etches very fast thus limiting control of the etching process. In addition, the thin AZO provides no visual guide which could lead to under etching or over etching. More so, with a discontinuous TCO deposition process (as a result of its PVD deposition nature), thin AZO will create top contact connectivity problems and will be ineffective for the 3-D diodes. Planar diodes fabricated with thin AZO films had a poor yield due to the problems of processing very thin AZO films.

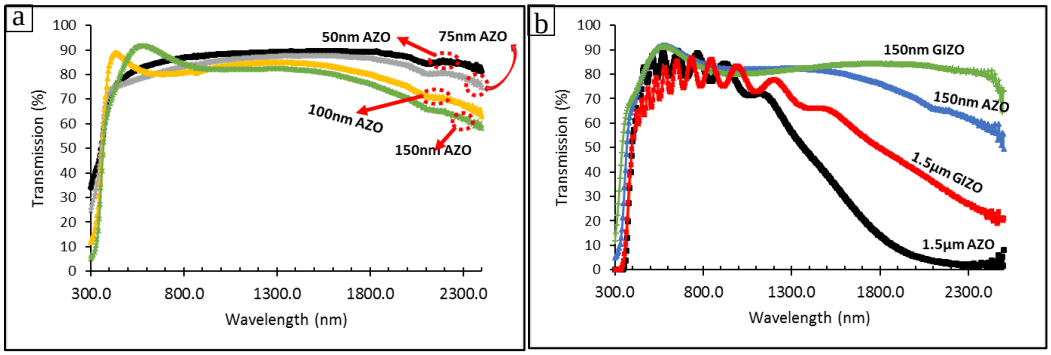

Fig 6.7 (a) Transmission results of thin AZO films – 50nm, 75nm, 100nm and 150nm; (b) Transmission results of 150nm and 1.5µm AZO and GIZO films

Alternatively, a different TCO material could be employed such as Indium Gallium Zinc Oxide (IGZO usually referred to as GIZO). The transmission result of such conductive GIZO material is shown in Fig 6.7b. Similar to AZO, GIZO absorbs infrared radiation with increasing thickness but at a slower rate compared to AZO. However, at 150 nm thickness, GIZO transmission is almost flat from

visible to infrared frequencies. On the positive side, the optimized GIZO material is slightly more conductive than the optimized AZO material as shown in Table 6.3. Absorption results of GIZO on ZnO NWs shown in Fig 6.8a show a reduction in absorption at 2.3 µm infrared wavelength from 49.47 % for AZO on NW sample to 28.11 % for GIZO on NW sample. Depositing GIZO on a-Si:H on ZnO NW sample showed no difference in absorption. Photodiode samples with GIZO as TCO showed good contact resistance and had diode properties including dark currents similar to AZO samples.

Table 6.3 Diode and Material Properties of AZO and GIZO TCO

TCO	AZO	GIZO
Dark current at -2V (A/cm^2)	1.5 x 10^{-9}	2.3 x 10^{-9}
Ideality factor, n	1.79	1.68
Diode series resistance (Ω-cm^2)	1.39	1.10
Sheet resistance (Ω/□)	500	361

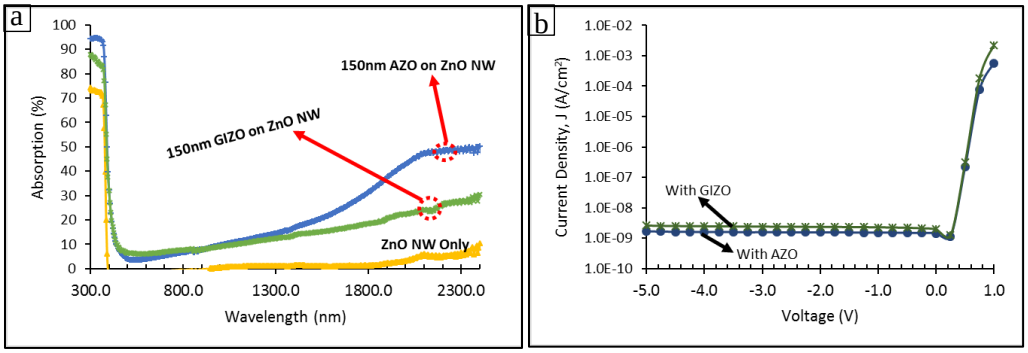

Fig 6.8 (a) Absorption results of ZnO NW and TCO coated ZnO NWs showing impact of the TCOs as window layer for infrared devices; (b) Dark current IV characteristics of planar diodes fabricated with 150nm GIZO and AZO as TCOs.

While infrared absorption from the TCO can be reduced by switching from AZO to GIZO, absorption from p$^+$ a-Si:H layer as shown in Section 4.3.3, also attenuates the radiation transmitted to the absorber. When combined with GIZO, infrared absorption from p$^+$ a-Si:H and GIZO TCO becomes significant.

Fig 6.9 shows the transmission spectra of 25 nm p^+ a-Si:H coated on 2.75 µm ZnO NWs and 100 nm GIZO TCO deposited on 25 nm p^+ a-Si:H also coated on 2.75 µm ZnO NWs as typically used on the illumination window of the photodiodes. The figure shows that the combination of these materials reduced infrared transmission by up to 20 %. The reduced transmission means the infrared radiation available for absorption by the absorber layer of the 3-D diode is reduced which will impact the infrared photo-generated carriers and ON/OFF ratio. However, the combination of 25 nm p^+ a-Si:H and GIZO as TCO represents the best compromise between the desire for low window layer infrared absorption and the need for a conductive top contact for photodiode operation.

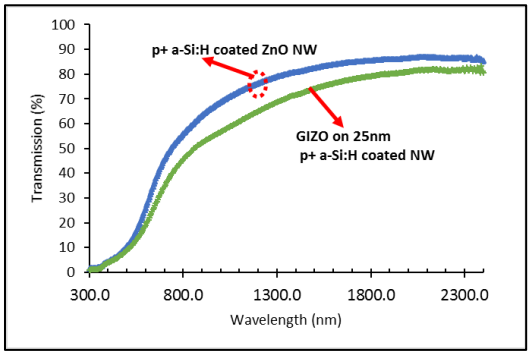

Fig 6.9 Transmission spectra of 100 nm GIZO deposited on 25 nm p^+ a-Si:H film coated on ZnO NWs, and absorption spectra of a-Si:H coated ZnO NW showing the effect of infrared absorption by the p^+ a-Si:H and GIZO coatings

6.5 Dark Current Analysis and Optimization

As stated in Section 6.3, ON/OFF ratio of 3-D infrared photodiodes were impacted by the absorption in the TCO and high dark currents. In Section 6.4, an alternative TCO was developed with lower infrared absorption compared to AZO. In this section, analysis and optimization of the different possible factors responsible for the high dark current is presented.

Dark or leakage currents in 3-D photodiodes could be due to process variables or techniques. The high aspect ratio of a 3-D device places extra requirements on its processing including issues such as

conformal coverage, uniformity and lithography which could have medium to high impact on device performance.

In addition to processing techniques, leakage currents could also be due to device structure or material properties. These in general, could arise from one or combination of several factors such as contact injection, thermal generation or recombination in surface and/or interface states.

Contact injection (or tunneling) is the injection of electrons through the *p-i* interface by tunneling through the potential barrier [76], [99]. This mechanism is strongly bias dependent and leads to an exponential increase of dark current with voltage. As described in section 2.3.3, a reverse bias creates a potential barrier to minority carrier injection and leads to a reverse bias suppression of dark current. This reverse bias suppression of dark current gives photodiodes the ability to realize low dark currents which are lower than the material's intrinsic resistance. In contact injection limited diodes, carriers injected from the contacts are able to overcome this potential barrier and tunnel across the diode thereby increasing its dark current. As the applied reverse bias increases, injected carriers are energized and readily tunnel across the potential barrier leading to its strong bias dependence. The significance of contact injection on tunneling mechanism implies that a reduction in the barrier height by reducing the depletion layer width will significantly increase the resultant dark current. Similarly, the effect of a reduced barrier height can also be observed with increasing field at the *p-i* interface. With an applied reverse bias across the diode's junctions, the depletion layer widens and charges within the i-layer are depleted. This depletion of charge from the i-layer causes the field at the *p-i* interface to increase. When the applied reverse bias is held steady, such as in a transient measurement, the deep states in the i-layer are depleted with time leading to an increase in the field at the p-i interface which in turn leads to increase in contact injection. Steady state current is reached when the i-layer is fully depleted which implies a steady field is maintained at the p-i interface. Typical results and schematic representation of contact injection is shown in Fig 6.10a and b [99].

Thermal generation current arises when carriers are excited from deep states to the band edges and then collected by the field in the depletion region as illustrated by Fig 6.10b-d [100]. It is described by the Shockley-Read-Hall formalism [99] and largely depends on the defect density of the material as given in equation 2.10. Ignoring contribution from edge and surface states, this implies that thermal generation increases as the density of states in deep states (band gap) increases (Fig 6.10c). In other words, diodes that employ more defective i-layer will be more susceptible to thermal generation currents. When a reverse bias is applied, charges within the i-layer are depleted. The dependence of thermal generation current on the depletion layer charge means it is less susceptible to bias voltage variations but more dependent on the depletion state of the i-layer. Another significant implication of its depletion charge dependence is that in a transient measurement set up where the voltage is held steady with time, the depletion of charges from the depletion layer will lead to a decrease in dark current until full depletion when a steady state current is obtained. Therefore, the typical current – time characteristic of a thermal generation current limited diode is as shown in Fig 6.10d. In theory, thermal generation model has no voltage dependence, however, small voltage dependence can be seen in measurements which has been attributed to field-enhanced emission, which increases current due to lowering of the effective excitation energy [99]. This variation with voltage could also be due to the spatial dependence of defect density which becomes prominent as the thermal generation zone expands into regions with high defect density due to a reverse bias [101].

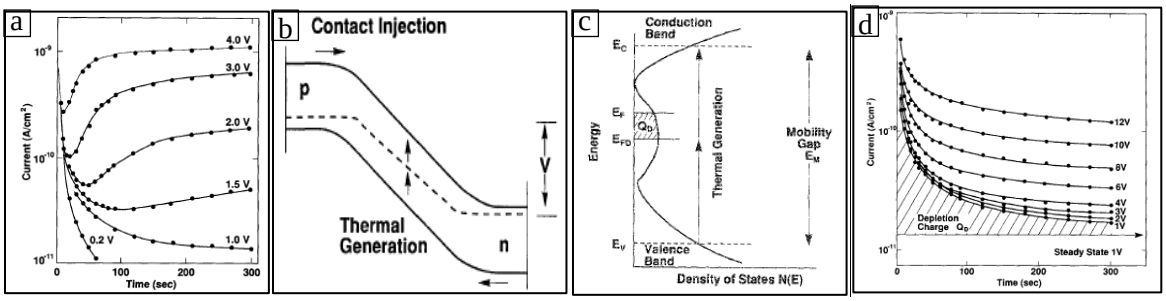

Fig 6.10 (a) Typical transient results a diode dominated by contact injection [99]**; (b) Reverse biased p-i-n diode illustration contact injection and thermal generation mechanisms** [99]**; (c) Density of states diagram showing the depletion charge, Q_D, and the origin of thermal generation charges through the gap states** [100]**; (d) Typical transient result of a diode dominated by thermal generation current** [100]

Similar to thermal generation currents, dark current due to surface/interface recombination is defect mediated. This defect generated current is due to the presence of dangling bond defects and other forms of electronic active states on the surface/interfaces of the materials within the photodiode. The energy of these states could span across the band gap [102], [103]. The exponential increase in surface/interface states in 3-D diodes makes this source of dark current of significant importance.

Examination of the dark currents in photodiodes could indicate the dominant mechanism responsible for its dark current. For example, an exponential increase in dark current with voltage suggests contact injection could be dominant although spatial defect distribution leading to thermal generation current can also show voltage dependency. Definite measurements such as transient measurements could help identify contact injection or thermal generation current where the density of states at the Fermi level could be estimated. Identifying the impact of surface/interface state to the dark current involves changing its density through multiple devices either by changing the device dimension or by applying other types of surface/interface state modification.

Dark I-V characteristics of a typical un-optimized planar and 3-D diode is shown in Fig 6.11. Dark current density of the un-optimized planar device is ~ 10^3 – 10^4 lower than that of the 3-D diode. This,

in general implies the mechanisms responsible for the high leakage currents in the 3-D diodes are those mechanism that get magnified by the 3-D morphology or presence of ZnO NWs.

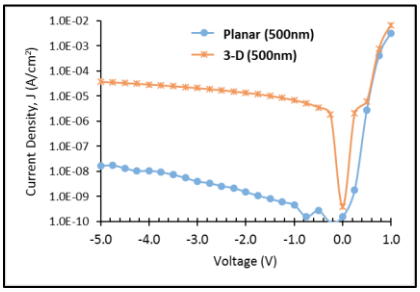

Fig 6.11 Dark IV characteristics of un-optimized planar and 3-D diodes

6.5.1 Scum on Patterned Bottom Contact

The choice of Cr as a bottom electrode for 3-D diodes was reinforced by the availability of Cr sputtering systems in the lab and its resilience to most chemical etchants thereby making it a good choice when multiple processes are required. Unfortunately, patterning and etching Cr with a photoresist (PR) leaves behind scum or some form of surface modification that is difficult to remove or eliminate. This scum is not visible to available microscopes and is resistant to descum processes. However, when such surface is subjected to a hydrothermal growth solution, the scum grows and embeds the NWs as shown in Fig 6.12. Blanket Cr surface (without any patterning) (Fig 6.12a) and glass substrate (Fig 6.12b) show the individual NWs and no haze can be seen embedded. For the photoresist patterned Cr surfaces of Fig 6.12c and Fig 6.12d however, a haze can be seen embedded in the NWs on the Cr side. The lithographic interface can be clearly seen on the dotted lines and the glass section of the image shows individual NWs without any haze. This scum induced haze grows with exposure to the hydrothermal growth solution and for very long exposure (above 20 hours), the haze completely covers the NWs.

The effect of this haze on the photodiodes can be seen with Fig 6.13 and Table 6.4. For the planar diodes, minimum impact was observed. The planar-diode-blanket-Cr electrode with no exposure to both photoresist and the hydrothermal solution and the planar diode with prior exposure to photoresist

and hydrothermal solution had similar dark currents at low reverse bias voltages. With 3-D diodes however, patterning the Cr bottom electrode with photoresist degraded the dark current by an order of magnitude, the saturation current density by 2 orders of magnitude and the ideality factor by 55 %.

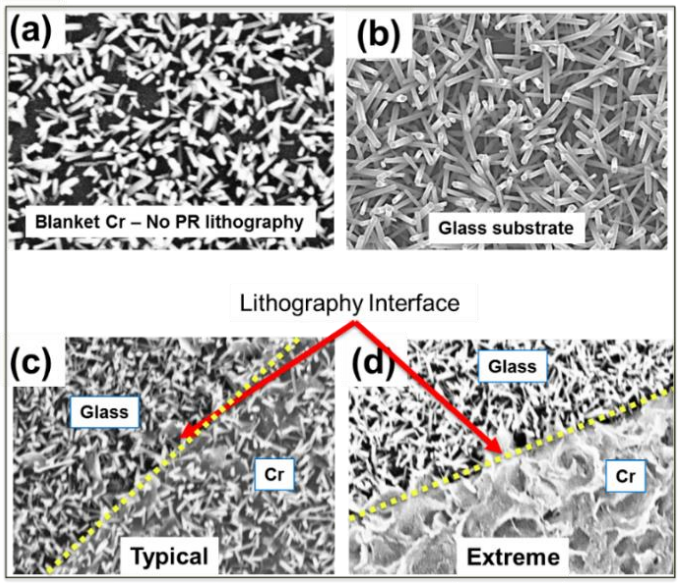

Fig 6.12 Effect of photoresist patterning on NW network on Cr electrodes (a) No exposure to photoresist and lithography; (b) Glass substrate; (c) Patterned Cr electrodes on glass substrate. Photoresist was used to create patterns on the Cr electrodes; (d) Extreme case of (c) as substrate is exposed to long growth times (~ 20 hours)

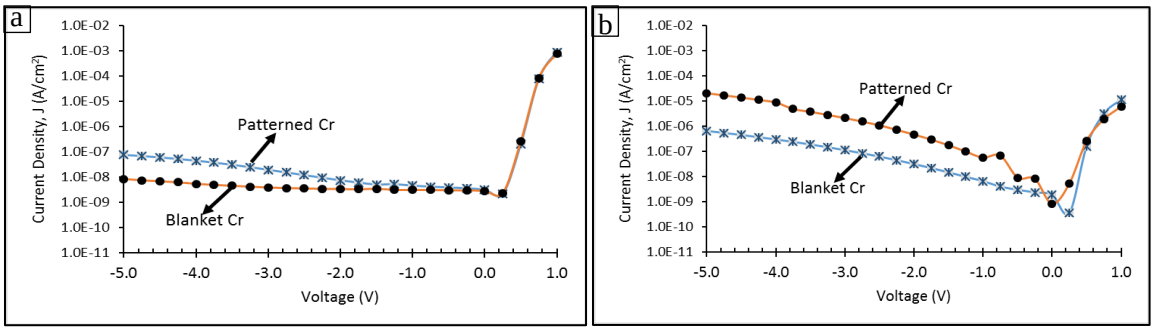

Fig 6.13 Dark IV characteristics of (a) planar diodes on blanket Cr electrodes and patterned Cr electrodes; (b) 3-D diodes on blanket Cr electrodes and patterned Cr electrodes

Table 6.4 IV characteristics of planar and 3-D diodes based on photoresist surface treatment

	Planar Diode		3-D Diode	
	Blanket Cr electrode	Patterned Cr electrode	Blanket Cr electrode	Patterned Cr electrode
Dark current density, J @ -2V (A/cm^2)	7.3×10^{-9}	3.3×10^{-9}	3.1×10^{-8}	4.6×10^{-7}
Ideality factor, n	1.90	1.91	2.20	3.41
Saturation current density, J_0 (A/cm^2)	9.0×10^{-12}	1.0×10^{-11}	6.0×10^{-12}	4.0×10^{-10}

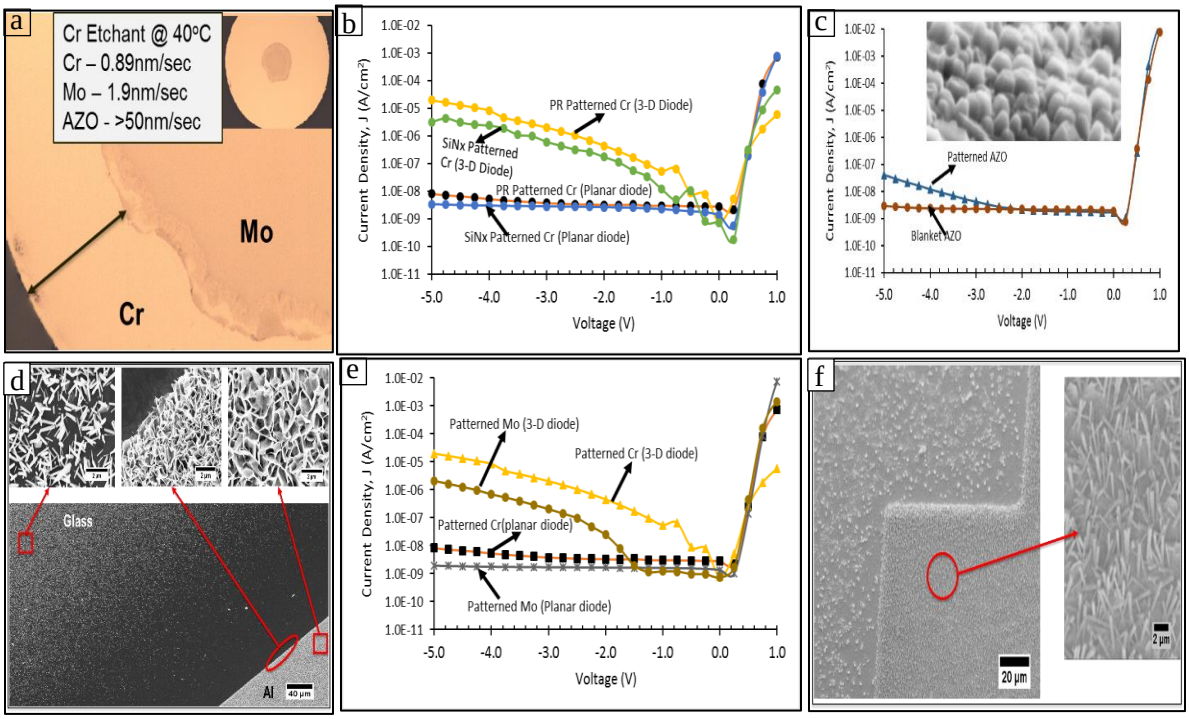

Fig 6.14 (a) Effect of etch rate differences on bi-layer Cr-Mo; (b) Dark IV characteristics of planar and 3-D diodes from SiNx hard mask patterned Cr bottom electrodes; (c) Dark IV characteristics of a planar diode on AZO bottom electrode (Inset is SEM micrograph of dense ZnO NWs grown on 100nm AZO film). (d) SEM micrograph of ZnO NW growth on 100nm Al; (e) Dark IV characteristics of planar and 3-D diodes on patterned Cr and Mo electrodes; (f) SEM micrographs of ZnO NWs on patterned Mo electrode

To eliminate this scum and associated foreign growth when subjected to hydrothermal growth, several approaches could be employed. These approaches include modifying Cr surface before lithography by employing a bi-layer metal, eliminating photoresist contact with Cr by using SiNx film as a hard mask for Cr patterning or replacing Cr with another metal.

Aside the unnecessary duplication, using a bi-layer metal technique as shown in Fig 6.14a will lead to a layered bottom electrode with different layer areas and uneven edges. This is because of the ability of Cr etchant to etch most available metals faster than Cr. The effect of using a sacrificial SiNx as a hard mask is a better alternative (Fig 6.14b). This however adds to the process steps. Replacing Cr with another available electrode is the most effective alternative. As a replacement electrode, suitably thick AZO serves as a seed layer leading to very dense NWs (Fig 6.14c); Al dissolves in the hydrothermal solution transforming from a shiny substrate to almost transparent in addition to nucleating dense and interconnected plates (Fig 6.14d). Molybdenum forms an effective electrode (Fig 6.14e) and shows good growth of NWs (Fig 6.14f).

6.5.2 Contact Injection

As stated earlier, contact injection responds mostly to changes in barrier height either by sweeping the applied reverse bias voltage or by changing the depletion layer width through i-layer thickness variations. The dark IV curves shown in Fig 6.13b shows some bias dependence indicating possible contact injection. To further investigate this phenomena, Fig 6.15 shows the dark I-V characteristics of diodes with different i-layer thicknesses. The underlying ZnO NWs in the 3-D diodes have an average length of 6.5 μm and density of 3.0×10^7 NW/cm^2. As expected, the figure shows that dark current of planar diodes is less sensitive to i-layer thickness variations and not dependent on reverse bias voltages. The planar structure of the planar diodes implies that the entire diode area is uniformly separated by the same i-layer thickness with similar quality of *p-i* interface. At 500 nm, thickness of the i-layer is already significant and poses a significant barrier to tunneling. On the other hand, the dark current of

the 3-D diode show some reverse voltage dependence especially at low i-layer thicknesses. The reduction of dark current as thickness increases especially at higher reverse bias voltages indicates the presence of a weak contact injection mechanism which reduces as i-layer thickness is increased. This contact injection is reduced as i-layer thickness is increased. As given in Section 3.4.2, the maximum thickness of a-Si:H that can be conformally coated on ZnO NWs is equal to or less than half the average separation between the NWs. Thus, a trade-off is required between having a conformal 3-D coated i-layer and lower dark current due to increasing i-layer thickness. Regardless of this trade-off, the potential width created by the 2 µm i-layer thickness is significant and would reduce the tunneling probability of injected carriers to tunnel across the diode. Transient results of 3-D diodes with 500 nm thick i-layer shown in Fig 6.17b shows steady dark current with time up to 55 seconds. As explain in section 6.5, a characteristic of contact injection limited diodes is an increase in transient current at a given reverse bias voltage as the i-layer charge is depleted. The observation of a steady state rather than an increasing current in Fig 6.17b indicates contact injection is only weakly responsible for the dark.

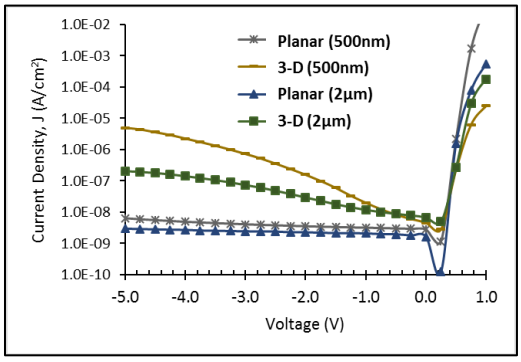

Fig 6.15 Dark IV characteristics of planar and 3-D diodes with 500nm and 2µm i-layer thicknesses

6.5.3 Thermal Generation Current

The impact of thermal generation current on diodes is an increase in recombination of charge carriers leading to an increase in dark current. Recombination of charge carriers in diodes largely depend on

the absorber's defect density and can is associated with the diode ideality factor introduced in section 2.3.3. High ideality factor of 2.6 for the 3-D photo-diode compared to 1.7 of the planar diode as given in Table 6.2 suggest higher recombination in the 3-D diodes which has a significant effect in its dark current. To evaluate the impact of this mechanism on the leakage current of 3-D photodiodes, dark I-V characteristics of 500 µm x 500 µm planar diodes using two different absorber materials were investigated (Fig 6.16a). Consistent with its presentation in Chapter 4, recipe A was developed with only SiH_4 and has no H dilution while recipe B has SiH_4/H_2 ratio of 1:5. FTIR microstructure measurements as presented in Table 6.5 indicate that recipe A is more defective and hence should have higher thermal generation effect. As expected, dark current density of the diode with recipe B is lower than that from recipe A and approaches the noise level of the measuring unit. At 2V reverse bias, dark current density of recipe B is about 35 % lower than recipe A. The higher dark current density of recipe A and its greater defect density as given by FTIR measurements show it is more susceptible to thermal generation current effect than recipe B. Regardless of the relative impact of thermal generation currents, both diodes show low dark currents comparable to reported values in literature [76], which indicates the thermal generation current effect is minimal in both cases. This result is further verified by the transient results shown in Fig 6.16b. The transient results show stable currents up to 200 seconds from both diodes. It also confirms the dark currents independence with bias voltage as stated in Section 6.5.2. Density of states extracted from the transient results as described by Street *et al*. [99] is given in Table 6.5 and shows that recipe A is about one order of magnitude more defective than recipe B in line with the FTIR results.

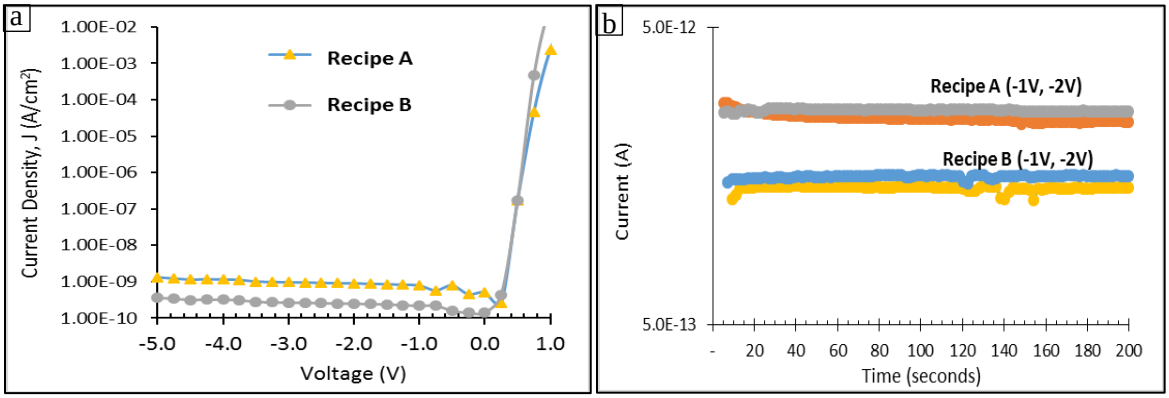

Fig 6.16 (a) Dark IV characteristics of planar diodes fabricated with absorber (i-layer) from two different recipes (A and B); (b) Transient current results from both diodes

Table 6.5 Material and Diode Properties of Recipe A and B

	Recipe A	Recipe B
SiH_4/H_2 ratio	50:0	1:5
FTIR Microstructure	3.3	36
Dark current at -2V (A/cm^2)	9.0×10^{-10}	5.9×10^{-10}
$N(E_F)$ (cm^{-3})	2.53×10^{17}	5.54×10^{16}

Fig 6.17a shows dark I-V characteristics of 500 µm x 500 µm planar and 3-D diodes using the defective recipe A. The underlying ZnO NWs for the 3-D diodes have an average length of 5 µm and density of 5.7×10^8 NW/cm^2. While the planar diode shows stable dark current density with reverse bias voltage, 3-D diode show a voltage dependent dark current density. The significance of using the same recipe is to translate material dependent phenomena from one type of device to another. That implies that the thermal generation behavior as established in the planar diode should be applicable to the 3-D diode. This behavior is further verified by transient currents from the 3-D diode shown in Fig

6.17b. The stable currents as reverse bias voltages are increased up to 5V over one minute measurement time show the minimal impact of thermal generation current.

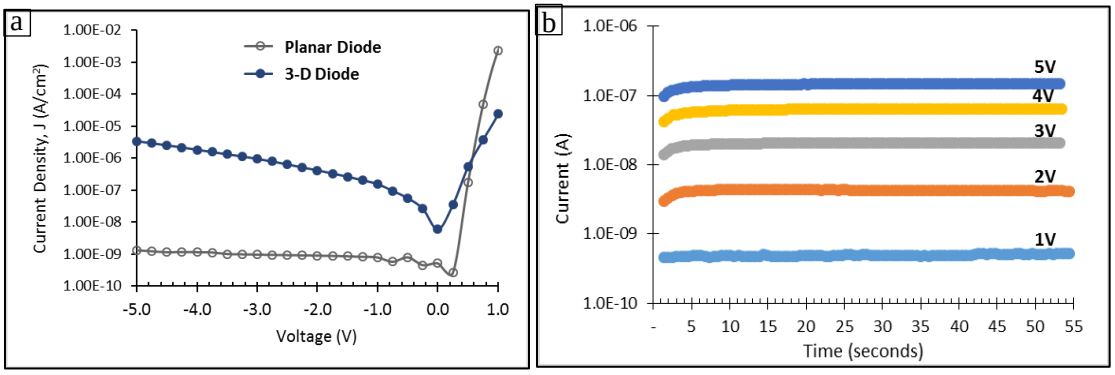

Fig 6.17 (a) Dark IV characteristics of planar and 3-D diodes using recipe A; (b) Transient results of 3-D diodes at varying reverse bias voltages.

While defective a-Si:H shell is important for infrared absorption as shown in Chapter 4, the use of such a defective material in a photodiode seems counter intuitive. However, the foregoing has shown that the additional defects in the a-Si:H shell have minimal impact on the performance of the diodes. It is also obvious from the results that using the same materials, 3-D diodes perform poorer than planar diodes and have dark currents densities between ~ 1 – 3 orders of magnitude higher. These results imply that the dominant mechanism contributing to their high currents depends on their structure rather than the materials used.

6.5.4 Effect of 3-D Structure - Surface/Interface State Analysis

The high ideality factor of the 3-D diode suggests a higher recombination of charge carriers. However, the discussion in the previous section shows that such recombination is not significantly dependent on the properties of the absorber material. Thermal generation current described in the previous section narrowly focused on thermally generated carriers due to defects in the intrinsic absorber material. The dark current may also include thermally generated current from defect states across the diode at the

junction surface/interfaces. The 3-D structure of the 3-D diodes however has a significant impact on the surface/interface state density and thus requires a systematic investigation.

Surfaces and interfaces of materials are important due to their potential electronic active states. Exposed dangling bonds and unpassivated interfaces could have active electronic states that lie in the band gap. These defective states could then become recombination centers and contribute to leakage current in devices such as diodes. In 3-D materials and other high aspect ratio structures, the total effective surface area increases exponentially, thereby increasing the potential amount of active surface and interface states. The increase in effective surface area of 3-D diodes compared to planar diodes occur on both sides of the diode - the ZnO/n^+ interface and the p^+/TCO interface. The exponential increase of the surface area of these interfaces implies that their electronic condition could have a big impact on the device performance especially the dark current. The p^+/TCO interface is an Ohmic junction due to the degenerate nature of the TCO. The ZnO NW/n^+ interface can however be Ohmic or Schottky in which case the junction could exist in an accumulated, depleted or inverted state. Fitzgerald and Grove reported that the leakage current in diodes depends on the total number of Shockley-Read-Hall (SRH) centers included in its depletion region [103]. They also demonstrated that surface states (or SRH states on the surface) are uniformly distributed in energy over the band gap and showed that the number of SRH centers included in the depletion region depend on the SRH states within the metallurgical junction in addition to such SRH states from field induced junctions created at depletion or inversion conditions between the semiconductor and an adjoining surface [103]. DiLello *et al.* has in addition showed that dark current is highest in Ge diodes when the interface between Ge and n^+ contact is depleted [13]. Chen *et al.* reported that native defects on the surface of ZnO NWs act as adsorption sites which depletes the surface, creates a space charge region and leads to surface band bending [104]. Thus in the absence of any treatment, ZnO/n^+ interface could exist in a depleted mode.

Minimizing or eliminating the depletion condition at the ZnO/n^+ interface is a challenge. One approach is to dope the ZnO NWs into accumulation state (DiLello *et al*. used this approach [13]) or to reduce the density of native defects on the surface by annealing (Chen *et al* used the annealing approach to reduce the ZnO NW depletion condition [104]). Both approaches require changing the electronic state on the surface of the ZnO NWs. It is generally believed that hydrothermal growth process is a dirty process relative to vacuum deposition processes thus ZnO NWs obtained from hydrothermal process are expected to have a high concentration of surface defects. The high concentration of surface defects could thus raise the threshold of surface treatment needed to make an impact. Fig 6.18 shows the dark I-V characteristics of two identical 3-D diodes with 2 μm i-layer thickness. ZnO NWs on one diode was first annealed at 200°C for 8 hours before the diode fabrication process while the annealing step was omitted in the other diode. While annealing could help reduce the concentration of surface band bending thus reducing its depleted condition [104], prior annealing for 8 hours in this case had no noticeable impact. The threshold of the surface treatment that will be required to make a noticeable impact on the surface states at the ZnO/n^+ interface is high and may require a more extensive surface treatment procedure. A different approach such as changing the total number of included SHR centers by geometry may be necessary.

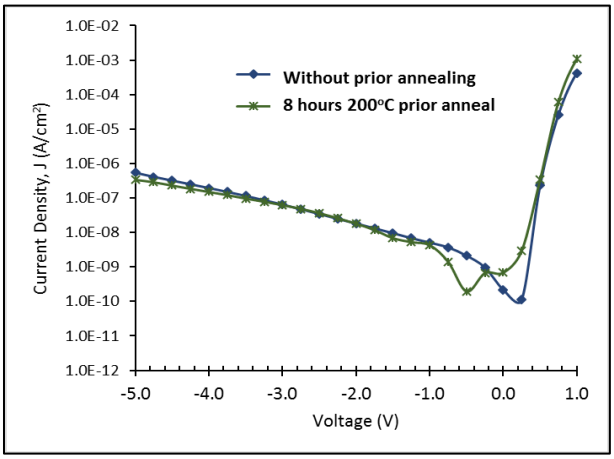

Fig 6.18 – Dark IV characteristics of 3-D diodes with and without pre-annealing process of the ZnO NWs

Like the defect states embedded within a material, surface and interface states act similarly and provide recombination centers that lead to higher leakage current. These states increase with increase in surface area which can be provided by the introduction of NWs, increasing its density or length. Fig 6.19a shows dark I-V characteristics of two un-optimized 500 nm thick i-layer 3-D diodes with different NW densities while Fig 6.19b is for 2 µm thick i-layer 3-D diodes with different NW lengths. It can be seen that as ZnO NW density increases from 5.9 x 10^7 NW/cm^2 to 2.1 x 10^9 NW/cm^2 in Fig 6.19a, or NW length increases from 3 µm to 8 µm in Fig 6.19b, dark current increases. These differences imply an increase in surface and interface states as the NW density or length increase which in turn degrades the dark current.

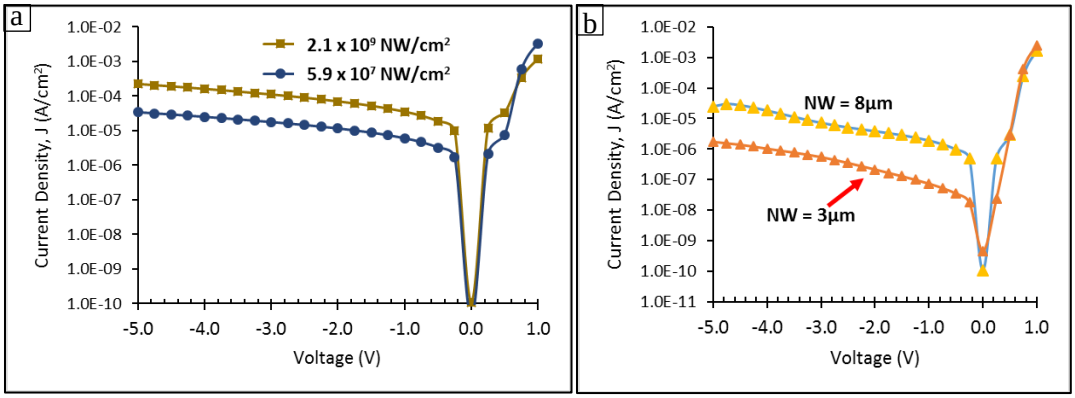

Fig 6.19 Dark IV characteristics of 3-D diodes based on different NW (a) densities; (b) lengths

To further verify the contribution of surface/interface states to the 3-D diode dark current, Fig 6.20a shows the top view of a 3-D diode indicating the presence of an intentionally created 'NW gap' between the edge of the *n-i-p* stack and the NW area. The screenshot of the mask shows the variation of the NW gap such that while the outside dimensions of the diodes are the same, the dimensions of the area containing the embedded NWs vary from one diode to another. The variation in the area of the NW coverage leads to changes in the number of enclosed NWs which in turn can be correlated to the additional surface area created by the 3-D materials system. This method of varying the surface/interface area ensures a uniform density of NWs are maintained and also ensures each diode is subjected to exactly the same conditions such that run to run variations or process variations due to changing NW density or length are eliminated. Fig 6.20b shows the dark I-V characteristics of different 3-D diodes with the same dimensions but containing varying percentages of enclosed NWs. The diodes have an i-layer thickness of 500 nm while the underlying ZnO NWs in the 3-D diodes have an average length of 6.2 µm and a density of 1.5 x 10^8 NW/cm^2.

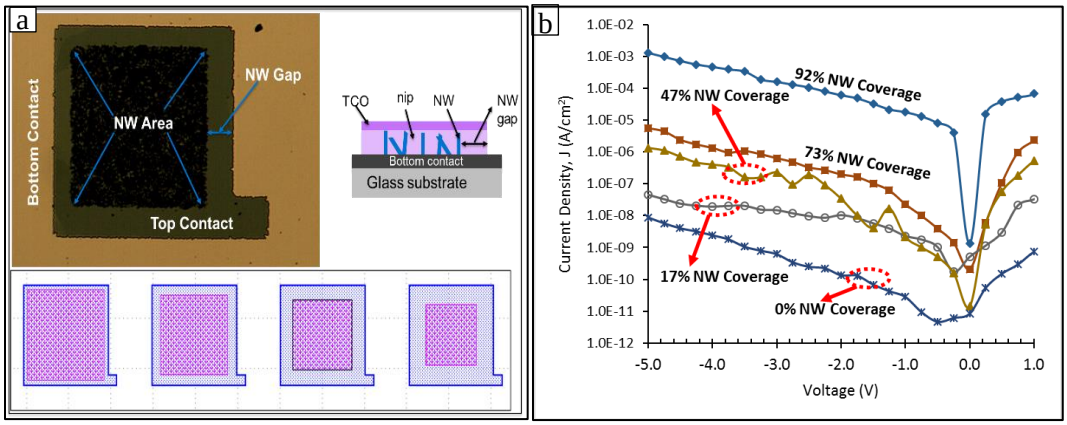

Fig 6.20 (a) Structure of the 3-D diode showing the presence of a NW gap used to vary the NW coverage area and number of embedded NWs; (b) Dark IV characteristics of 3-D diodes on the same substrate but with different NW coverage areas as a percentage of the diode area dimensions

Table 6.6 Properties of different 3-D diodes of the same area dimensions but different percentage of NW coverage

	Planar	3-D Diode 1	3-D Diode 2	3-D Diode 3	3-D Diode 4
Diode Area (cm^2)	1.3×10^{-3}	1.3×10^{-3}	1.3×10^{-3}	1.3×10^{-3}	1.3×10^{-3}
NW Coverage (cm^2)	-	2.3×10^{-4}	6.3×10^{-4}	9.6×10^{-4}	1.2×10^{-3}
NW Coverage (cm^2)	-	17	47	73	92
NW Surface Area (cm^2)	-	3.3×10^{-3}	9.1×10^{-3}	1.4×10^{-2}	1.79×10^{-2}
Total Surface Area (cm^2)	1.3×10^{-3}	4.6×10^{-3}	1.1×10^{-2}	1.5×10^{-2}	1.9×10^{-2}
Change in Surface Area (%)	0	2.5×10^{2}	6.9×10^{2}	1.1×10^{3}	1.4×10^{3}
Dark Current Density @ -2V (A/cm^2)	1.3×10^{-10}	3.4×10^{-8}	1.0×10^{-8}	2.7×10^{-7}	6.0×10^{-5}
Recalculated Dark Current Density @ -2V (A/cm^2)	1.3×10^{-10}	9.9×10^{-9}	1.3×10^{-9}	1.7×10^{-8}	4.1×10^{-6}

Table 6.6 shows the properties of the different diodes shown in Fig 6.20b. The diode area was determined from the mask (planar) dimensions of the diode while the total surface area included the additional surface area due to the NWs enclosed. The additional surface area due to the number of NWs enclosed was calculated from the NW coverage, length and density information. The nanowire

coverage was determined from the lithographic masks using the planar dimensions of the nanowire coverage area for the different diodes. The NW length and density information was calculated from the plan-view SEM micrographs as described in section 3.2. The number of NWs in the sample as determined by the density characterization ranged from 1.1×10^8 NW/cm^2 to 2.1×10^8 NW/cm^2 with an average NW density of 1.5×10^8 NW/cm^2 and an standard deviation of 0.4×10^8 NW/cm^2 which gives about 25% variation between the upper and lower limits. The impact of such variation on the surface area of the 3-D diodes 1 – 3 is smaller than the difference between the effective NW surface area due to the dimensions of the NW coverage. This implies such variation is negligible and the surface area calculated from the average NW density can be adopted as representative. In addition, at the scale of ~10^8 NW/cm^2, variations between 3-D structures produce relatively smaller effect compared to similar variations occurring between planar and 3-D morphologies. The uniformity of the length and density of the nanowires was determined from several SEM micrographs taken of the sample at different locations across the 3-inch glass substrate as presented in Table 6.7.

Table 6.7 Calculated density of Nanowires for sample in Fig 6.20

S/N	Number of NWs (No ± 3)	Measured Area			Estimated Density (NW/cm^2)
		Length (nm)	Width (nm)	Area (cm^2)	
1	39	4730	4000	1.9×10^{-7}	2.1×10^8
2	39	5170	3780	2.0×10^{-7}	2.0×10^8
3	105	10710	8800	9.4×10^{-7}	1.1×10^8
4	109	11310	8730	9.9×10^{-7}	1.0×10^8
5	113	10580	7820	8.3×10^{-7}	1.4×10^8
6	108	9860	7200	7.1×10^{-7}	1.5×10^8
Average Density:					1.5×10^8
Standard deviation:					0.4×10^8

From the Table 6.6, it can be seen that the inclusion of NWs to the diodes increases their surface area by ~ 1 – 3 orders of magnitude. This ~ 1 – 3 orders of magnitude increase in the effective surface area of the diode in turn degrades their dark current by ~ 2-5 orders of magnitude from 1.3 x 10^{-10} A/cm^2 in the planar case to 6.0 x 10^{-5} A/cm^2 at 2V reverse bias when 92% of the diode area is covered with NWs. This increase in effective surface area also unevenly scales the forward bias current density due to differences in the geometrical area and effective surface area of the diode. Using the total surface area (which accounts for the additional surface area from the NWs), recalculated dark current densities compare closely with values obtained for planar samples and recalculated forward bias current density (0 – 1V bias on the I-V curve) for the diodes mostly overlap each other. The recalculated current density treats the 3-D diodes like a very big planar diode by mapping the total effective surface area onto a planar-type device structure. By mapping the 3-D diodes unto planar-type diode structure and obtaining similar results, it becomes obvious that the biggest contribution to the high dark current is the exponential increase in surface area and its attendant surface states caused by the introduction of ZnO NWs.

This conclusion is further supported by the mobility lifetime product ($\mu\tau$) of the diodes extracted from the Hecht model by fitting theoretical plots to experimental results as shown in Fig 6.21. Mobility lifetime product is a measure of carrier recombination in a device where lower numbers imply that carriers recombine very fast due to availability of many recombination centers. The mobility lifetime product of the planar diode with recipe B was found to be 5.5 x 10^{-9} cm^2/V and is comparable to published reports [76]. The planar diode with a more defective recipe A has a comparable but slightly smaller mobility lifetime product of 5.3 x 10^{-9} cm^2/V. In line with the results of Section 6.5.3, the increased defect density of recipe A had minimal impact on both the dark current density and thermal generation current in the planar configuration. In the 3-D configuration however, the mobility lifetime

product reduces by 34% to 3.5 x 10^{-9} cm^2/V which is can be related to the additional surface/interfaces created.

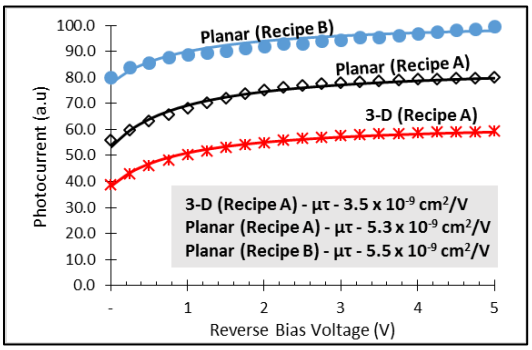

Fig 6.21 Photocurrent results fitted onto the Hecht model to extract the mobility lifetime product. Solid lines are fittings while markers are experimental results. The photocurrents were measured in Amperes but has been scaled differently to prevent overlapping curves and provide better visibility to the fits

6.6 Infrared Measurements

Optical results as shown in Chapter 4 indicates that 3-D diodes are good infrared absorbers. The implication is that 3-D diodes are expected to have higher output currents in response to infrared illumination under reverse bias. However, ON/OFF ratio given in Table 6.2 showed no significant infrared gain. This result was attributed to absorption in the TCO which reduced the infrared radiation reaching the absorber and relatively high dark currents which raised the noise level and impacted its ON/OFF ratio. By employing some of the optimizations described in previous sections, TCO absorption has been reduced to ~ 20 % of the incident infrared radiation and dark current densities have been reduced by ~ 3 orders of magnitude from around 3.6 x 10^{-5} A/cm^2 (Fig 6.11) to ~ 1.0 x 10^{-8} A/cm^2 (Table 6.6) at 2V reverse bias. Here, results of infrared measurements of these improved devices are presented. Infrared sources used include the previously described 1.55 μm LED source and the commercially available heat lamp (Section 5.3).

Fig 6.22a shows infrared response of a 3-D diode comprising of 2 µm i-layer coated over 3 µm long NWs illuminated with the 1.55 µm LED while Fig 6.22b shows the same device irradiated with the heat lamp. The diode shows over 2 orders of magnitude dynamic ratio at a reverse bias of 1V using the 1.55 µm LED while the infrared gain is about one order of magnitude using the heat lamp. Examination of the optical results shown in Chapter 4 indicates that the developed 3-D material system is not most sensitive at 1.55 µm wavelength. The poor sensitivity at this region notwithstanding, the 3-D structure shows promising infrared gain. In the absence of an optical bench or optical focusing set up, the narrow radiation angle of the LED makes it difficult to focus the infrared radiation on the diodes. In contrast, the heat lamp with its wide radiation angle is easier to use thereby making the heat lamp the preferred source. All other infrared response and ON/OFF ratios presented hereafter were taken with the heat lamp.

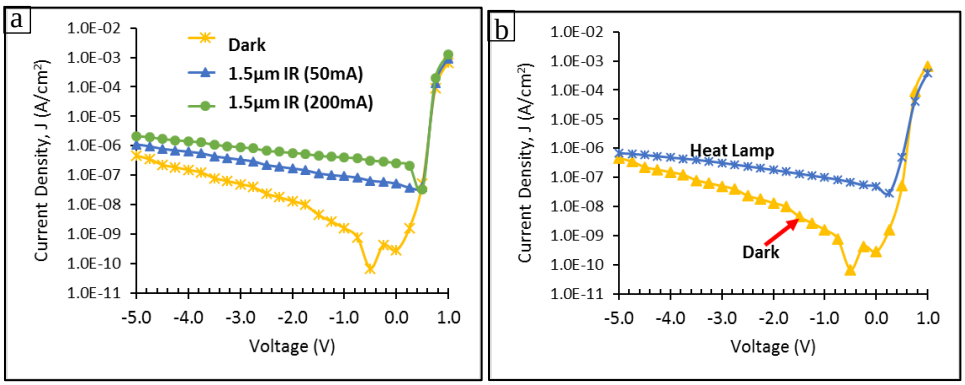

Fig 6.22 (a) 1.55µm IR response of 3-D diodes with 2µm i-layer on 3µm ZnO NWs

The importance of low dark currents for 3-D diodes for infrared absorption is obvious from Fig 6.22. At 1V reverse bias, the dark current density is 1.6 x 10^{-9} A/cm^2. The infrared photo current density at the same reverse bias voltage is 4.0 x 10^{-7} A/cm^2 for 1.55 µm LED irradiation and 9.9 x 10^{-8} A/cm^2 for the heat lamp irradiation. Under the same illumination, diodes with high dark current density will have their ON/OFF ratio greatly degraded. Fig 6.23 shows a plot of ON/OFF ratios of several diodes with their measured dark current density at 2V reverse bias under the heat lamp illumination. This in addition

to Fig 6.22 shows the ON/OFF ratio entering double digits as dark current density reduces to below 1 x 10^{-8} A/cm^2.

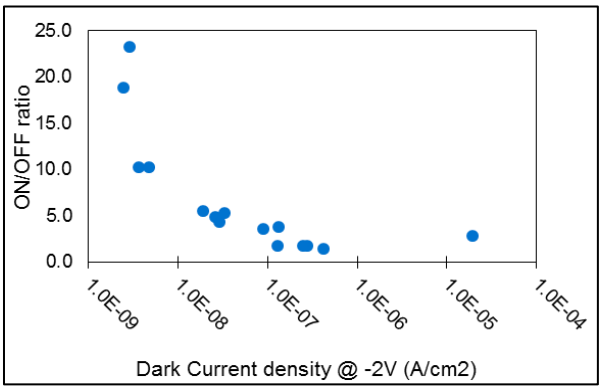

Fig 6.23 Plot of ON/OFF ratios with respect of dark current of infrared diodes at -2V bias.

While increasing the NW length increases the scattering (Chapter 4), such increase also increases the dark currents to levels where the ON/OFF ratio from infrared photo generated current may be consumed. A trade-off is hence required to ensure low dark currents while also maintaining a decent level of scattering in order to absorb infrared radiation. Ultimately, lower dark current for high dense NW network of very long NWs will be the best condition. NvF factor defined in Section 3.4.2 as the ratio between NW length and coated film thickness can be a useful parameter to evaluate the relationship between NW length and film thickness with their dark current and ON/OFF ratios. Table 6.8 gives the parameters of 5 different diode samples while Fig 6.24 shows SEM micrographs of their representative morphology as a correlation of their NvF factors. Diode 5 with the highest NvF factor is expected to have the highest amount of scattering and thus the highest infrared ON/OFF ratio. However, the dark current density of diode 5 is in the ~ 1 x 10^{-6} A/cm^2 range as shown in Fig 6.25. This high dark current reduces the ON/OFF ratio obtained from the diode to single digits thus making the planar 'diode 1' more infrared responsive. This is expected because of the disproportionate effect long NWs have on both optical absorption and dark currents. According to Fig 4.12, increasing the NW length from 1 µm

to 11 μm for 600 nm a-Si:H coating corresponding to NvF factor increase from 1.7 to 18.3 increases the infrared absorption at a wavelength of 2.3 μm from 35.6 % to 55.5 % corresponding to a 1.6 factor increase. However, as Table 6.8 shows, increasing the NvF factor from 1.7 to 7.2 has a disproportionate increase in dark current from 5.0 x 10^{-9} A/cm^2 to 5.6 x 10^{-6} A/cm^2 at reverse bias voltage of 1V corresponding to a ~ 10^3 factor increase. This emphasizes the need for optimum NW conditions to maximize the effect of both.

Table 6.8 Properties of Diodes with Different NvF Factors

Device	Diode 1	Diode 2	Diode 3	Diode 4	Diode 5
NW Length (μm)	0.0	3.0	3.4	6.0	3.6
i-layer thickness (nm)	2000	2000	2000	2000	500
NvF Factor	0.0	1.5	1.7	3.0	7.2
Morphology (SEM)	Planar	Textured/3-D	3-D	3-D	3-D
Dark Current (Relative)	Low	Low	Low	Medium	High
Dark Current @ -1V (A/cm^2)	3.8 x 10^{-9}	1.6 x 10^{-9}	4.9 x 10^{-9}	4.5 x 10^{-9}	5.6 x 10^{-6}
IR Response (Relative)	Low	High	High	Medium	Low

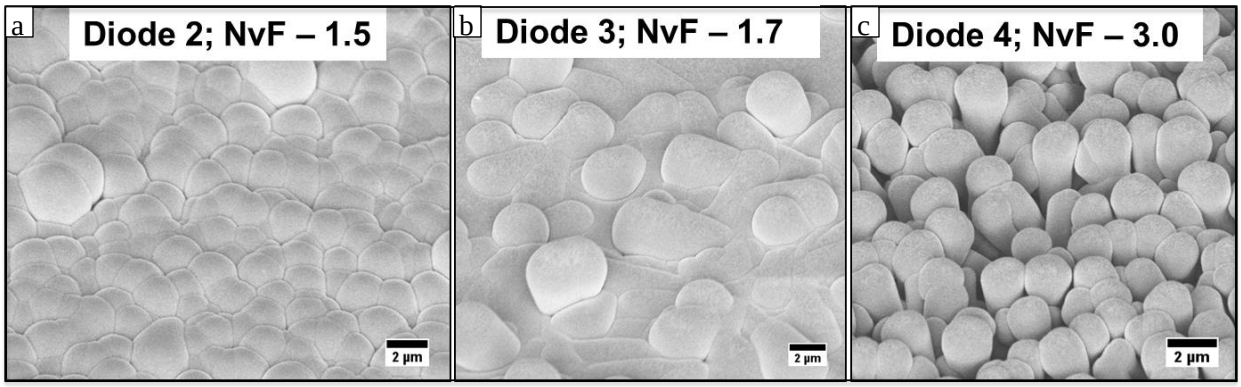

Fig 6.24 SEM micrographs of 3-D PIN Diodes 2, 3 and 4

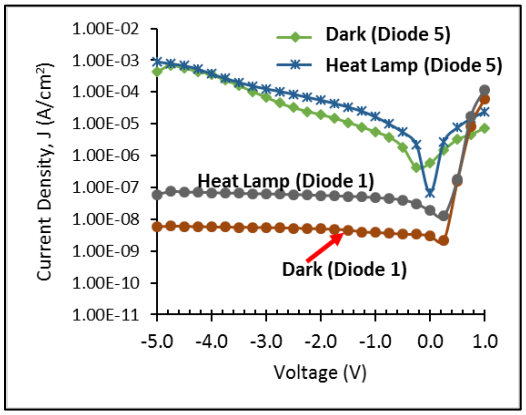

Fig 6.25 – Infrared Response of Diodes 1 and 5 under a heat lamp illumination

A plot of the ON/OFF ratios of diodes with different NvF factors with respect to the percentage of NW coverage is shown in Fig 6.26. As shown from the figure, the exponential increase in the dark current density of diode 5 as NW coverage increases results in the opposite effect on the ON/OFF ratio. The optimum NvF factor for increased infrared response is at 1.7 while NW coverage of around 60% of the diode area produces the highest response. These optimum values agree with the discussions from earlier sections and balances the need for low dark current with the importance of having a 3-D structure for infrared absorption.

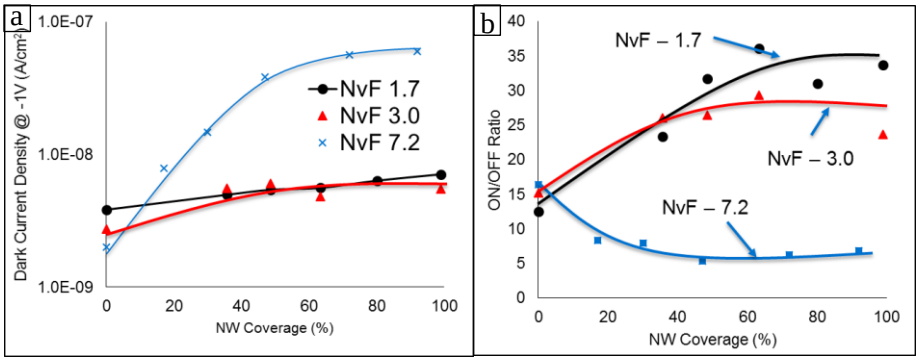

Fig 6.26 (a) Dark current as a function of NW coverage for diodes 3, 4 and 5 corresponding to NvF factors 1.7, 3.0 and 7.2; (b) ON/OFF ratio diodes 3, 4 and 5 corresponding to NvF factors 1.7, 3.0 and 7.2 as a function of NW coverage

6.6.1 3-D Photoconductor vs Photodiode

Both photoconductors and photodiodes as forms of photodetectors have been fabricated for infrared detection. The table below outlines the major differences between both devices as infrared detectors.

Table 6.9 Comparison of 3-D Photodetectors for Infrared Detection

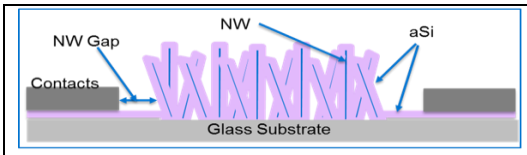	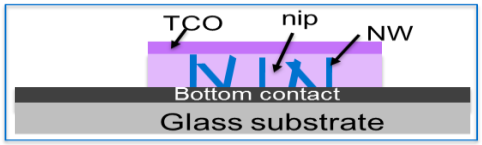
3-D Photoconductor	**3-D Photodiode**
Current injection device	Operates based on carriers generated within the depletion width
Horizontal current flow	Vertical current flow
Horizontal current ensures gaps can be created between NWs and contacts	Vertical structure forecloses that possibility. Horizontal structure might be modified to create such gap but may come at the expense of contact resistance
Dark current scales with channel and gap length	Dark current scale with i-layer thickness
Channel and gap can be a few hundred micrometers	Impractical to have such lengths in a-Si:H coating
Device area can be increased without sacrificing dark current	Larger device area increases dark current
Nothing hinders IR absorption	Contacts reduce IR absorption by ~20%
Can accommodate higher bias voltages	Reverse bias is limited by breakdown considerations
Structure makes interface states irrelevant	Structure magnifies interface state effects

6.7 External Quantum Efficiency

The foregoing has established the validity of 3-D diodes to absorb infrared radiation. Infrared results were however obtained with a 1.55 µm IR LED with unknown power profile due to the unavailability of a power meter capable of calibrating the IR LED at such wavelength. Similarly, the infrared power

output of the 50W heat lamp source was also unknown. This makes it necessary to source external assistance for External Quantum Efficiency (EQE) measurements.

For EQE evaluation, two typical planar and 3-D photodiodes with dimensions of 1 mm x 1 mm were measured with the 3-D photodiode having 63 % NW coverage. Both devices have 2 µm intrinsic layer with an underlying ~ 6 µm long ZnO NWs for the 3-D diode. The size of the devices in relation to the smaller beam size caused the samples to be under-filled leading to an under-estimated spectral response of about ~ 30 % however, relative comparisons can be made from the results. The EQE measurement set up consists of a xenon (Xe) light source connected through a monochromator, chopper and lock-in amplifier system. The monochromator has a maximum filtering capability of ~ 1800nm and the Xe source has a wavelength dependent power profile. Above 1000nm, optical power output from the monochromator is less than 1 µW and decreases with wavelength in relation to 100 mW/cm^2 (AM1.5G) standard EQE system power output in the visible region. Zero and reverse biased measurements were carried out. Normalized EQE results from the measurements are shown in Fig 6.27.

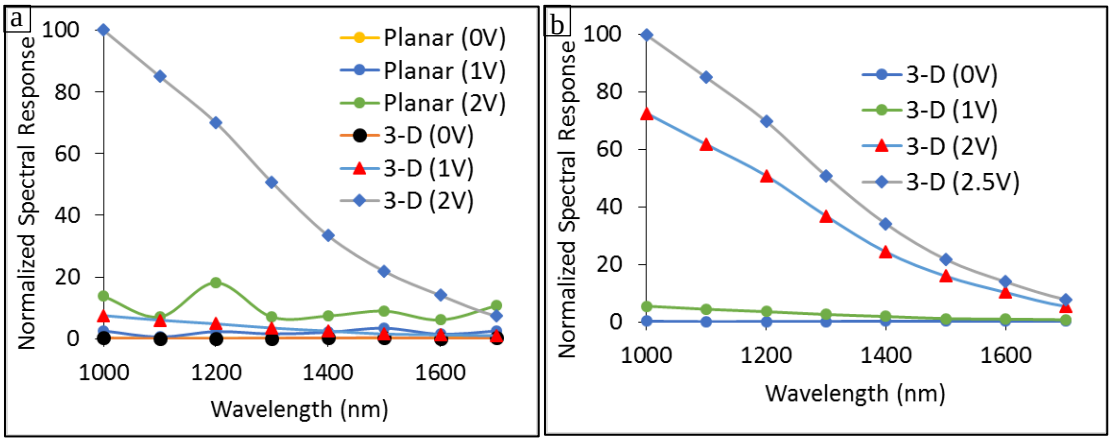

Fig 6.27 Normalized EQE results of (a) planar and 3-D diodes at 0, 1 and 2V reverse bias voltages and (b) 3-D diodes at 0, 1, 2 and 2.5V reverse bias voltages

As expected, the spectral response of the planar diode was low and remained flat across the wavelength from 1000 nm to 1700 nm. It was also less sensitive to reverse bias voltages. This was due

to its poor infrared absorption as previously discussed. The poor infrared absorption was further worsened by the increased recombination due to its 2 μm intrinsic layer.

In contrast to the absorption spectra shown in Fig 4.2, the spectral response of the 3-D diode show a downward trend between 1000nm and 1700nm and never increased above 1500nm as would be expected. This could be due to the optical power profile of the Xe lamp source which decreases with wavelength above 1000 nm wavelength. While EQE measurements are supposed to be independent of the light source, non-linear photoconductivity of several semiconducting absorber materials means they have to be calibrated. This becomes more important in the very low infrared optical power regime (< 1μW) supplied by the Xe lamp. A consequence of the defect mediated absorption phenomena as established in Chapter 4 is its non-linear absorption mode which could lead to threshold conditions required for infrared absorption. Such threshold conditions would be missing when very low infrared optical energies are applied as is the case with increasing wavelength.

Irrespective of the sub-optimal infrared conditions, the spectral response of the 3-D diode shown in Fig 6.27b shows increasing spectral response above 2V reverse bias voltage. The absence of an infrared response at 0V bias indicates a high level of carrier recombination as most infrared generated carriers recombine. This is further confirmed by the infrared spectral response seen at 2V and 2.5V reverse bias voltages. Under the same optical power indicating the same infrared absorption, spectral response at 2.5V reverse bias is higher than that at 2V reverse bias. This shows a high level of carrier recombination which the infrared generated carriers experience thereby requiring a higher reverse bias potential to pull them to the contacts for collection. This is in agreement with the findings of section 6.5.4 which shows that the presence of a large number of surface/interface state impacts the performance of 3-D diodes.

6.8 Summary

This chapter presented the design, development, fabrication and optimization of 3-D infrared photodiodes. The dark currents of the diodes were analyzed and extensive optimizations embarked upon to reduce them. Such optimization techniques such as length, density and percentage coverage of NWs have been applied to reduce the dark current densities of 3-D diodes by 10^3-10^4. Infrared absorption using the developed 3-D diodes was also presented. Despite the reduction of available infrared radiation reaching the absorber by the window layers and relative higher dark currents with respect to the planar diodes, ON/OFF ratios of 3.6×10^1 has been achieved using a heat lamp infrared radiation and 2.5×10^2 using a 1.55 µm LED. As Fig 6.22 shows, the 1.55 µm LED infrared source gives a higher response than the heat lamp. Hence, the responses presented with the heat lamp could potentially be higher. Even the 1.55 µm center wavelength of the LED falls around the least sensitive region of the 3-D material system implying the response could be higher at longer wavelengths. Quantum efficiency measurements show a clear distinction between the planar diode and 3-D diode as infrared photodiodes and confirms the limiting effect of surface/interface states on the generated carrier recombination.

Chapter 7
Integrated IR Sensor Switch

In Chapter 5, the 3-D photoconductor was presented as an approach to demonstrate the effectiveness of 3-D hybrid ZnO NW/a-Si:H core-shell structure as an infrared photodetector. In this chapter, integration of the 3-D photoconductor onto a-Si:H TFT back channel compatible with flat panel technology is presented. Mask design and process development for the integrated device are first presented followed by some measurement results. A few process factors and their impact on the integrated device are also explored and presented.

7.1 Device Structure and Mask Development

In general, an image sensor pixel typically consists of 4 main blocks namely sensor, storage, switch and read-out blocks as shown in Fig 7.1a. The sensor block consists of the light sensor which could be a photodiode or photoconductor; the storage block generally consists of a capacitor for storing the sensor data after each capture frame; the switching block consists of a transistor used for switching between the storage and the read-out blocks; and the read-out block contains the read-out electronics to synchronize the stored data and transfer them to the buffer or amplifier for faithful reproduction of the sensor output. The output of the pixel is a sequence of charge integration and read-out employing several of the identified blocks in a synchronized fashion in order to effectively produce a digital image of the incident signal. During charge integration, the sensor block detects the incident radiation and converts that information into a current or voltage difference for storage in the storage block. After storing an equivalent electrical signal of the incident radiation into the storage block, the sensor block is turned off while the read-out phase starts. During the read-out phase, the switching block switches the stored signal from the storage block through to the readout block for onward transfer to an amplifier or buffer for display or further image processing. In the proposed infrared sensor-TFT (Fig 7.1b), the

sensor and the switching blocks are combined into a single device thereby enabling the potential for creating high resolution infrared sensor arrays.

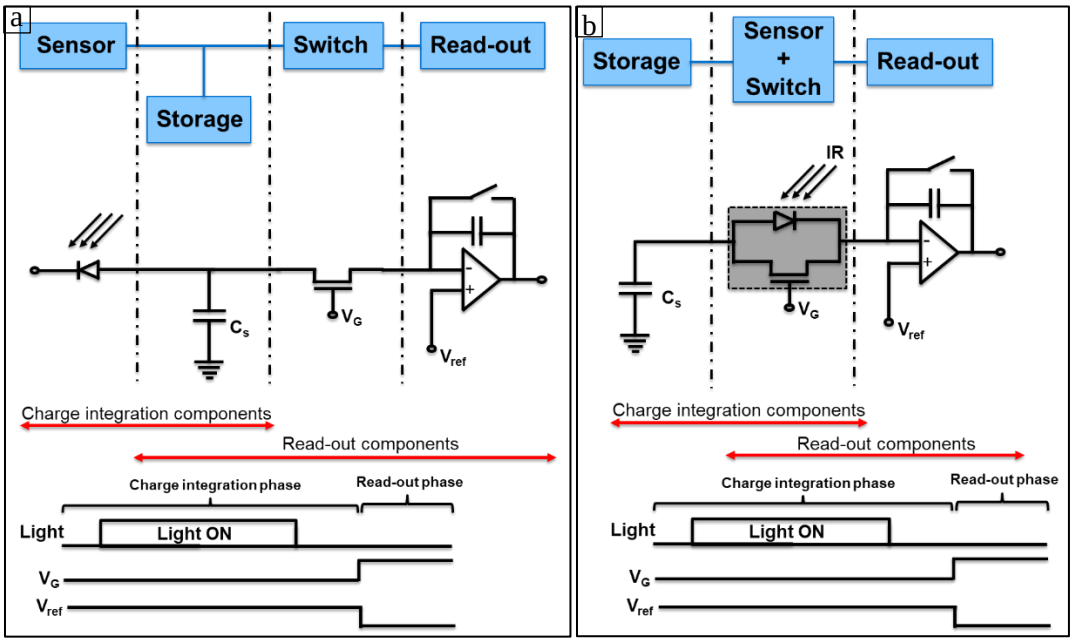

Fig 7.1 (a) Typical image sensor pixel showing the 4 main blocks of the pixel architecture; (b) Proposed sensor-TFT device pixel architecture showing the functionality of all main blocks of Fig 7.1a but using fewer components

Fig 7.2 shows a schematic structure of the proposed integrated infrared sensor-switch incorporating a TFT switch and a vertically integrated infrared sensor directly on top of the TFT. In the proposed infrared sensor-switch structure, the charge integration phase starts with exposure to infrared radiation while the TFT is in the OFF state. Absorption of infrared radiation by the top sensor layer would cause the sensor channel to conduct and charge the pixel storage capacitor. The amount of charge stored in the capacitor will depend on the intensity of the infrared radiation which will in turn determine the amount of current that will flow across the sensor channel. During the read out phase, the infrared signal is shut off thereby turning OFF the infrared channel while the TFT channel is turned ON by a gate bias. The charge integrated on the storage capacitor is then transferred to a charge amplifier through the TFT

channel thus realizing both infrared sensing and switching at different phases using a vertically stacked device which ensures maximum space utilization as well as high-resolution applications. The direct integration of an infrared sensor (in this case, a 3-D photoconductor) on the back surface of a-Si:H TFT produces a vertically integrated sensor-TFT which would be capable of the enhanced functionality of TFT switching and infrared detection. This enhanced single-device-dual-function structure could find applications in large area infrared sensor and high resolution arrays.

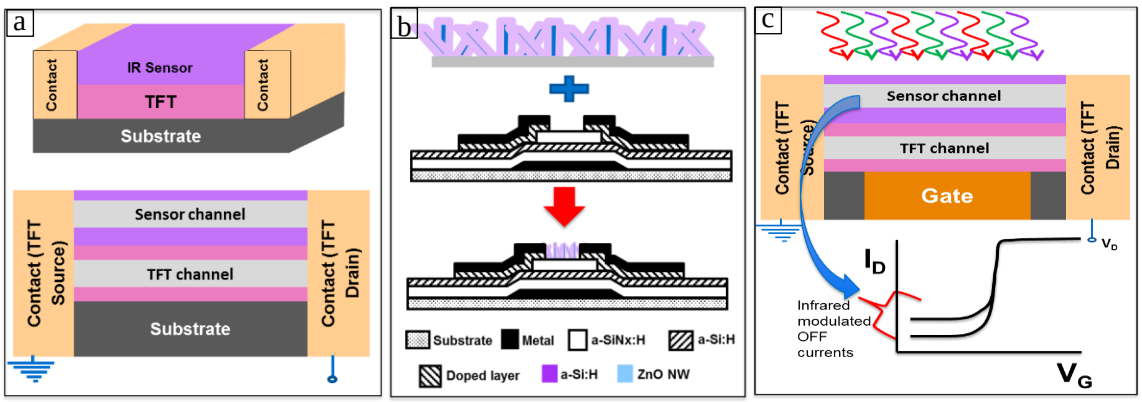

Fig 7.2 (a) Block diagram schematic of the integrated infrared sensor-switch; (b) Integrated scheme for the sensor-switch device; (c) Operation of the integrated infrared sensor switch

To fabricate the integrated IR sensor-switch, masks are needed. The broad integration flow for the proposed integrated infrared sensor-switch is shown in Fig 7.2b. This type of integration flow proposes the fabrication of a switching TFT followed by the integration of an infrared detector. While both types of infrared detectors (photodiode and photoconductor) could be integrated, the infrared photoconductor will be adopted due to its simple fabrication process making it well suited for a first step development of a new concept device. The infrared photoconductor will be integrated above the back channel of the TFT to provide an alternate conductive channel (sensor channel) for infrared generated current while the TFT channel remains above the dielectric for the TFT switching (the TFT channel) as shown in Fig 7.2a and b. The effect is an expected infrared modulated OFF currents as shown in Fig 7.2c which can

be used to modulate the charging of the storage capacitor and hence give an indication of the incident radiation.

The desired requirements for the integrated infrared sensor-switch and its process include large-area scalability, low temperature processing which will enable its fabrication onto low cost and low melting point substrates such as glass and plastic materials, and ability to integrate into the flat panel manufacturing industry.

Fig 7.3a shows the process flow for a back channel etched a-Si:H TFT while Fig 7.3b shows the process flow for integrating an infrared photoconductor onto the BCE TFT. The TFT process is a 5 mask process using 5 distinct masks while the integrated infrared sensor-switch is a 7 mask process with 6 distinct masks.

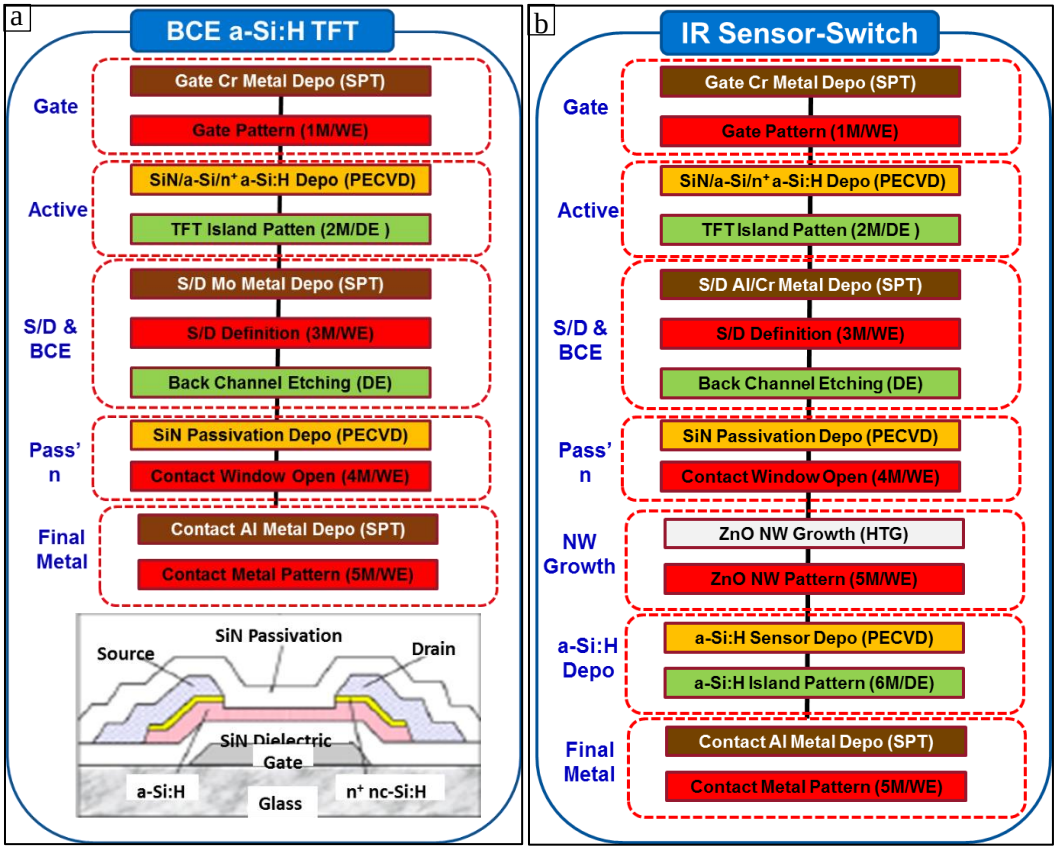

Fig 7.3 (a) Process flow for fabricating back channel etched TFT and schematic of the BCE TFT; (b) Process flow for fabricating integrated infrared sensor switch

The mask set was designed using Cadence IC Design Tool as part of a multi-project mask development with the integrated infrared sensor-switch portion contained in dies S1, S2 and X3 as shown in Fig 7.4. The mask set for the integrated infrared sensor-switch utilizes the same set of masks for the TFT with an additional mask for etching the NWs.

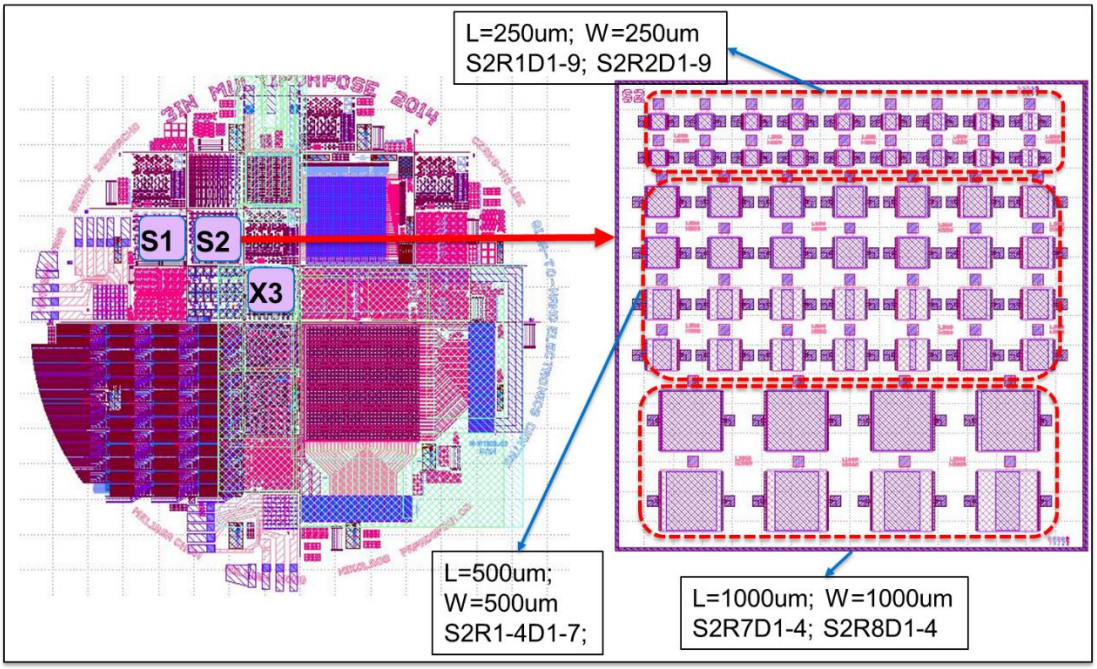

Fig 7.4 Integrated infrared sensor-switch mask set

7.2 Integrated 3-D Sensor-Switch Fabrication

As shown in Fig 7.3, integrated infrared sensor-switch fabrication first requires the fabrication of a TFT. The fabrication process starts with cleaning a Corning Eagle 2000 glass substrate with RCA-1 cleaning procedure. Next ~ 80 nm Cr gate electrode, deposited by rf sputtering is patterned and etched. The gate patterned substrate is then loaded into the PECVD cluster system for the deposition of 400 nm SiN_x, 125 nm a-Si:H and 55 nm n^+ a-Si:H films at 150°C. TFT Island or isolation patterning and etching are done. The process continues with a bi-layer Al/Cr deposition for S/D electrodes and afterwards, patterned and etched. The use of bi-layer of Al and Cr serves to improve the S/D contact while also protecting the S/D metal from via etching and future hydrothermal growth. The S/D patterns then serve as mask for a back channel etching where the n^+ film is etched up to the back a-Si:H channel. Passivation SiN_x is then deposited using the PECVD after which via holes are etched open for contact

to S/D electrodes. At this point, the fabricated TFT can be measured before further processing. Next, rf sputtered seed layer is deposited on the sample and immersed into a hydrothermal bath containing 25 mM aqueous solutions of zinc nitrate hexahydrate ($Zn(NO_3)_2 \cdot 6H_2O$, Sigma Aldrich) and hexamethylenetetramine (HMTA) ($C_6H_{12}N_4$, Sigma Aldrich) maintained at an average temperature of ~ 85°C for growth of ZnO NWs. The TFT sample containing grown ZnO NWs is cleaned, dried and the NWs patterned and etched. Next, the TFT-NW etched sample is loaded into the PECVD for conformal a-Si:H coating at 150°C. Afterwards, the island mask is re-used to pattern isolation islands to isolate each device. Then, a final Al metallization layer is deposited and etched for give the final device. A sample of the final device is shown in Fig 7.5

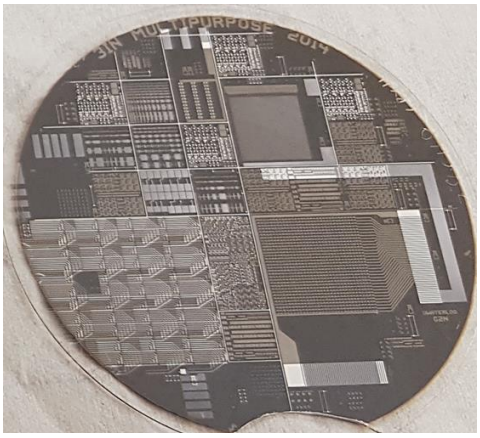

Fig 7.5 Integrated 3-D Sensor-Switch Device

7.3 Integrated 3-D Sensor-Switch Device Results

Fig 7.6 shows the transfer and output characteristics of a 500 µm x 500 µm base TFT of the integrated 3-D sensor-switch deposited at 150°C. The un-optimized TFT had an ON/OFF ratio of 10^5 at $1V_D$, V_T of 5.5V and OFF currents in the ~ 10^{-12} - 10^{-13} A range at a drain voltage of 1V. The output characteristics show both linear and saturation characteristics.

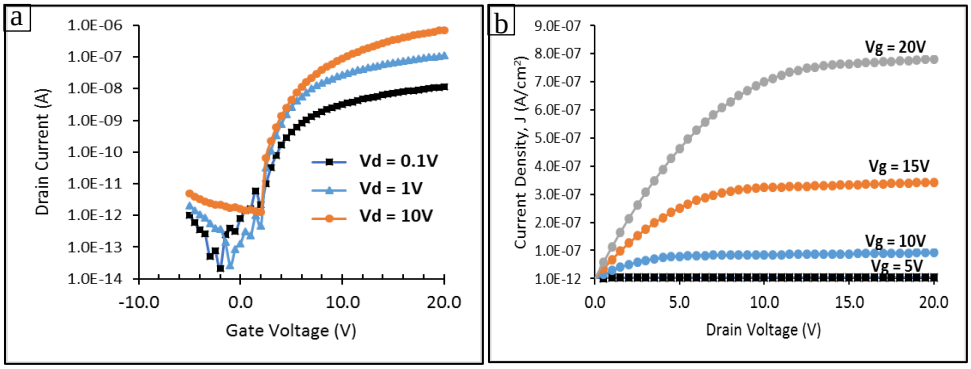

Fig 7.6 Characteristics of an integrated infrared sensor-switch base TFT (a) Transfer characteristics; (b) Output characteristics

The integration of 3-D photoconductors introduces several challenges which could impact the properties of the base TFT and/or the overall device. Some of these challenges are processing challenges such as exposure of the TFT for several hours in hydrothermal solution or etching non-idealities. Fig 7.7a shows the transfer characteristics a 250 µm x 250 µm TFT before and after 17 hours of hydrothermal ZnO NW growth. ZnO NWs were grown on the base TFT with an open 'via' for 17 hours in a hydrothermal solution. After the growth, the grown ZnO NWs were etched away and the TFT was re-measured. As can be seen from the figure, exposure to 17 hours of hydrothermal growth had no significant effect on the TFT performance as the characteristics of the TFTs overlapped each other. This is not surprising since the TFT was processed at 150°C while the ZnO NWs were grown at 85°C. The lower ZnO NW temperature means that heat effects are minimal. In addition, SiN_x passivation protected the channel and the rest of the TFT from oxidation or other chemical reactions from the solution. Only Cr metal on the via hole was exposed to the hydrothermal process which caused NWs to grow in the vias. Unetched NWs in the via hole could only impact the contact resistance of the top sensor device and not the TFT.

Similarly, Fig 7.7b shows the transfer characteristics of a 500 µm x 500 µm TFT with additional 700 nm a-Si:H film deposited on the back channel. The results show overlapping characteristics before and

after the top a-Si:H deposition. This indicates that the effect of additional stress of processing on the base TFT is negligible.

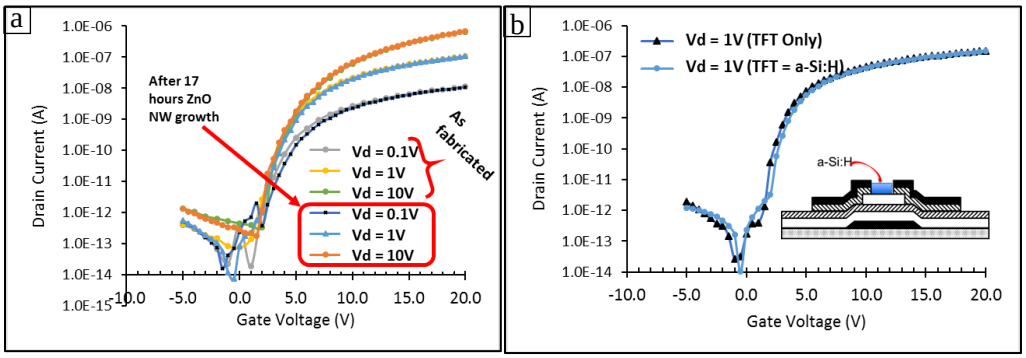

Fig 7.7 Transfer characteristics of a base TFT showing overlapping characteristics of the TFT (a) before and after 17 hours NW growth; (b) before and after 700nm a-Si:H deposition on the back channel

Fig 7.8a shows infrared response of the completed integrated sensor-switch device illuminated with the 1.55 µm LED. The device is a 250 µm x 250 µm sensor-TFT with only 50 µm x 250 µm NW coverage as shown in Fig 7.8b. The integrated device shows ~3 factor difference between the dark and infrared currents. This response is below the response of the infrared photoconductor shown in Fig 5.6 with the same outside dimensions. As shown in Fig 5.3, the increase in the NW gap for this integrated device (100 µm on each side adding up to 200 µm or 80% of the sensor channel length) creates a very resistive sensor channel that would suppress the infrared generated current. In addition, the reduction of the NW coverage reduces the capacity to absorb and generate carriers. For the photoconductor in Fig 5.6, the NW gap was 5µm on each side which minimizes both factors. In general, the response of Fig 7.8 shows that integrated infrared sensor-switch is feasible.

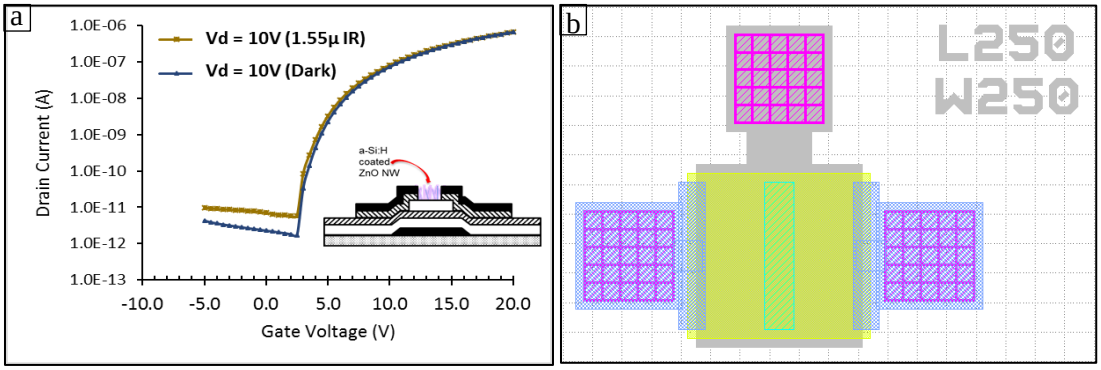

Fig 7.8 Infrared response of integrated sensor-switch showing infrared modulated dark current; (b) Top view of mask pattern showing the relative size of NW coverage in measured device of (a) with respect to the base TFT

7.4 Summary

This chapter demonstrated a new concept device called integrated infrared sensor – switching device and its feasibility to be integrated into the flat panel industry. To do that, the design and process development of the proposed integrated infrared sensor-switch were carried out. The hydrothermal growth process was shown to have minimal effect on the performance of the base TFT. Also, proof of concept result of an integrated infrared photoconductor and TFT switch was presented. The result demonstrated the feasibility of integrating 3-D infrared detectors into the flat panel industry for integrated functionality and to meet the needs of emerging applications in large area infrared detection.

Chapter 8
Summary and Contributions

8.1 Conclusion and Summary of Contributions

As stated in the Chapter 1, the objective of this Ph.D. is to develop and study the optoelectronic properties of a-Si:H based hybrid 3-D core-shell structures and their application as alternative infrared photodetectors suitable for meeting the needs of large-area infrared detection for emerging applications. The summary of the main contributions from this thesis is itemized below:

1. Development of 3-D a-Si:H coated ZnO NW material system for large-area infrared detection applications
2. Detailed study and characterization of the infrared optical properties of 3-D a-Si:H coated ZnO NW materials and demonstrated control of infrared absorption through control of the material properties
3. Fabrication of 3-D infrared photoconductors on low cost substrates and at low process temperatures using a simple processing technique
4. Demonstration of the infrared switching action of 3-D infrared photoconductors using pulsed infrared illumination
5. Fabrication of 3-D infrared photodiodes on low cost substrates and at low process temperatures
6. Dark current studies and optimization of 3-D diodes of a-Si:H coated ZnO NWs for higher signal to noise ratio
7. Proof of concept integration of 3-D photoconductors onto industry standard back channel etched thin film transistors suitable for large-area and flat panel industry integration

Three dimensional (3-D) material system comprising a-Si:H coated on a disordered network of ZnO NWs have been developed for large-area infrared detection applications. Properties of these 3-D material system have been extensively studied and factors that affect or control their infrared sensitivity were explored. The enhanced scattering due to the 3-D material morphology led to increased effective thickness of the coated film. The increased thickness enabled greater light-matter interaction which led to infrared absorption in a coated a-Si:H film. The infrared absorption was correlated to the defect density of the coated film and increases as the defect density increases. The results demonstrate a path to transforming otherwise defective thin amorphous films into useful materials that could be suitable for infrared absorption.

The developed infrared sensitive 3-D material system has been used to fabricate 3-D infrared photoconductors at a process temperature of ≤ 150°C. The 3-D photoconductors show low dark current through the introduction of a '*NW gap*' that makes the effect of the surface and interface states irrelevant. The NW gap however impacts on the infrared photocurrent as it presents it with a higher resistance to collection at the electrodes. A compromise is hence needed to accommodate low dark currents in the photoconductor with less resistance to infrared generated currents. Regardless, signal to noise ratio of 3.2×10^2 has been achieved for a 250 µm x 250 µm device. The results demonstrate the feasibility of having low cost, easy to fabricate infrared photodetectors for low cost infrared applications.

Similarly, 3-D infrared photodiodes have also been fabricated at a process temperature of ≤ 150°C. The high dark current density of the 3-D diodes was found to be primarily due to the increased surface/interface states that occurred as a consequence of the 3-D material structure. Optimization of the surface/interface states either by isolation, modification or reduction will thus lead to lower dark currents. Reducing the density of surface/interface states by reducing the height, density or coverage of NWs in the 3-D photodiode showed a decrease in the dark current density from a high of ~ 10^{-4} A/cm^2

to a low of ~ 10^{-9} A/cm^2, a 5 order of magnitude decrease with a promise of even more reductions by isolation or modification. Infrared signal to noise ratios of ~ 62 were achieved with 3-D photodiodes with 2 µm thick i-layer irradiated with a commercially available heat lamp while 2.5 x 10^2 ON/OFF ratios were achieved with a 1.55 µm LED illumination. The results demonstrate the possibility of large-area and low cost infrared detection for civilian applications with materials that pose little environmental and health problems to the populace.

To enable the integration of infrared detectors onto new devices for emerging applications, the developed 3-D photoconductor was integrated onto industry standard back channel etched TFTs. The process was developed at 150°C. The results show that integration of the infrared detector on the TFT has minimal impact on the switching ability of the base TFT. The integrated device show 3× increase in infrared generated current over the OFF current with the 1.55 µm LED illumination. The results show a proof of concept demonstration of the feasibility of integrating 3-D infrared detectors onto TFT backplanes used in flat panel industry.

8.2 Future Work

Based on the results obtained in this PhD study, several areas of interest have been identified for future work. They include

1. Surface/interface state treatment or isolation for more reduced dark current density of photodiodes
2. Integration of 3-D photodiodes onto BCE TFTs for large-area applications
3. Process optimization of 3-D integration for higher yield and higher infrared control of OFF current modulation

Point 1: To further improve the performance of 3-D infrared photodiodes, surface/interface treatment or isolation may be necessary. The significant impact of interface state defects on the dark current

behavior of 3-D photodiodes has been identified. Treatment or isolation of these interface state defects will expand the potential of fabricating 3-D photodiodes with very high NvF factors. Due to the exponential increase in surface area and its attendant increase in surface state defects, surface treatment will require a focused attention. However, another alternative might be to adopt a NW isolation technique where the impact of the NW surface on the photodiode will be isolated from the device behavior. Two isolation mechanisms have been proposed as shown schematically in Fig 8.1. In the first approach, the bottom electrode is placed on top of the ZnO NWs where it will be sandwiched between the NWs and the n^+ layer. This approach to NW isolation however requires a conformal bottom electrode as could be realized using deposition techniques such as Atomic Layer Deposition (ALD). In a second approach, a horizontal device structure where the contacts are offset and isolated from the NWs while a prior SiNx coating eliminates the ZnO NW surface from diode interference could be implemented. This structure can also serve as an alternative contact scheme to eliminate the top contact from the window area and eliminate infrared absorption from the TCO. This means that AZO could be used as a TCO since it will no longer interact with the incoming infrared radiation. Appendix B shows proposed process flow for both isolation schemes.

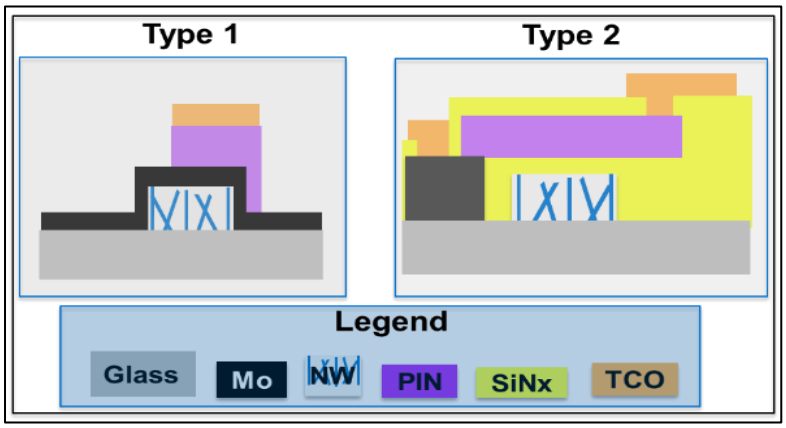

Fig 8.1 Schematic illustration of Proposed NW Isolation Schemes

Point 2: This PhD work has also demonstrated a proof of concept integration of 3-D photoconductors onto the back channel of industry standard BCE TFTs. It will be great to replicate this with a 3-D photodiode. This will especially be important to potentially increase the performance of the integrated sensor by allowing the suppression of dark current property of photodiodes to reduce its dark (OFF) current below the levels obtained with the photoconductor. This however, largely depends on the solution to point number one above and such solution when found will be of great impact to the integrated device

Point 3: The fabrication of integrated 3-D sensor-switching devices presents some challenging process constraints such as NWs growing in the 'via holes' leading to non – uniform density across the sample, which causes non – uniform NW etching which could impact yield. A grow, etch, re-grow and re-etch process could be implemented to minimize this impact. The importance of breaking this down is to reduce the wide difference in NW densities and lengths than can result in a single NW growth process and its resulting etching difficulties.

8.3 Published Articles and Conference Presentations

8.3.1 Refereed Journal Articles and Conference Proceedings

- **B.C. Iheanacho** and W. S. Wong, "Infrared Optical Absorption from Hybrid 3-D a-Si:H/ZnO Nanowire Structures", *Journal of Applied Physics*, **122**, 013102, **2017**
- M. Pathirane, **B. Iheanacho**, A. Tamang, C.-H. Lee, R. Lujan, D. Knipp, and W. S. Wong, "Hybrid ZnO nanowire/a-Si:H thin-film radial junction solar cells using improved nanoparticle front contact", *Applied Physics Letters*, **107**, 143903, **2015**
- Tamang, M. Pathirane, R. Parsons, M. M. Schwarz, **B. Iheanacho**, V. Jovanov, V. Wagner, W. S. Wong, and D. Knipp, "Zinc oxide nanowire arrays for silicon core/shell solar cells", *Optics Express*, **22**, pp. A622-A632, **2014**

- W. S. Wong, M. J. Chow, M. Pathirane, **B. Iheanacho**, and C.-H. Lee, "Heterogeneously integrated nanowires and thin films for flexible electronics", *IEEE AM-FPD*, **2014**, pp.37-40

- Liu, M. A. McCarthy, **B. Iheanacho**, W. S. Wong and A. G. Rinzler, "Recent developments of carbon nanotube enabled vertical organic light emitting transistors for OLED displays", *SID Symposium Digest of Technical Papers*, **44**, 1, p251, **2013**

Manuscripts under Review or In Progress

- **B.C. Iheanacho**, C.-H.Lee and W. S. Wong, "Hybrid ZnO Core – a-Si:H Shell Infrared Photodetectors Integrated with Thin-film Transistors" *submitted*, **2017**

- **B.C. Iheanacho** and W. S. Wong, "Radial Junction 3-D Infrared Photodiodes Using Hybrid 3-D ZnO Nanowires Core – a-Si:H Thin-Film Shell" *in progress,* **2017**

- **B.C. Iheanacho** and W. S. Wong, "Defect Mediated Infrared Response of 3-D Amorphous Silicon and Zinc Oxide Material System", *in progress,* **2017**

8.3.2 Refereed Conference Presentations and Exhibitions

- **B.C. Iheanacho**, C.-H. Lee and W. S. Wong, (2017) "Infrared Absorption of 3-D Core-Shell ZnO – a-Si:H Nanowire Structures" Electronics Materials Conference (EMC), Notre Dame, IN, USA

- D. Knipp, A. Tamang, **B. Iheanacho**, N. Yumnam, V. Jovanov, V. Wagner, and W. S. Wong, (2016) "Metal oxide optical antennas (Invited Paper)" SPIE Optics and Photonics, San Diego, CA, USA

- Pathirane M., **Iheanacho B.**, Hosseinzadeh H., Tamang A, Lee C-H., Goldthorpe I., Knipp D., and Wong W. S., (2015) "Hydrogenated Amorphous Silicon-based Flexible Nanowire Solar Cells", Materials Research Society (MRS), San Francisco, CA, USA

- Pathirane M., **Iheanacho B**., Lee C-H., and Wong W. S., (2015) "Amorphous Silicon Nanowire Solar Cells on Flexible Substrates", TechConnect World Innovation, Washington, DC, USA

- W. S. Wong, M. J. Chow, M. Pathirane, **B. Iheanacho**, and C.-H. Lee, (2014) "Heterogeneously integrated nanowires and thin films for flexible electronics", IEEE 21st International Workshop on Active-Matrix Flatpanel Displays and Devices, Kyoto, Japan

- **Iheanacho B.**, Pathirane M., Lee C-H., Hamadani B., and Wong W. S., (2014) "A-Si:H Thin-Film – Nanowire Hybrid Structure for Infrared Sensor Applications", Materials Research Society (MRS), San Francisco, CA, USA

- Pathirane M., Hosseinzadeh H., **Iheanacho B**., Tamang A, Lee C-H., Goldthorpe I., Knipp D., and Wong W. S., (2014) "Influence of Top Electrodes on Amorphous Silicon Nanowire Solar Cells", Waterloo Engineering Innovate, Waterloo, ON, Canada

- Pathirane M., **Iheanacho B**., Tamang A., Jovanov V., Knipp D., and Wong W. S., (2013) "Hybrid ZnO Nanowire/a-Si:H Thin-Film Solar Cells on Flexible Substrates", International Semiconductor Device Research Symposium, Bethesda, MD, USA

- **Iheanacho B.,** Pathirane M., and Wong W. S., (2013) "Infrared Absorption of Thin Film – Nanowire Hybrid Structures", International Semiconductor Device Research Symposium, Bethesda, MD, USA

- Pathirane M., **Iheanacho B**., Tamang A., Jovanov V., Knipp D., and Wong W. S., (2013) "Hybrid ZnO Nanowire/a-Si:H Thin-Film Solar Cells on Flexible Substrates", Electronics Materials Conference (EMC), Notre Dame, IN, USA

- B. Liu, M. A. McCarthy, **B. Iheanacho**, W. S. Wong and A. G. Rinzler, (2013) "Recent developments of carbon nanotube enabled vertical organic light emitting transistors for OLED displays", SID Display Week, Vancouver, BC, Canada

- Parsons R., Pathirane M., A. Tamang, **Iheanacho B**., Jovanov V., Schwarz M., Wagner V., Wong W. S., and Knipp D., (2013) "Zinc Oxide Nanowire Arrays for Silicon Rod Solar Cells: Wire Design and Experimental Realization", Materials Research Society (MRS), San Francisco, CA, USA

- Pathirane M., **Iheanacho B**, Tamang A, Jovanov V., Knipp D., and Wong W. S., (2013) "Novel Hybrid Nanowire/Thin-Film Core-Shell Structures for Solar Cells on Flexible Platforms", Waterloo Engineering Innovate, Waterloo, ON, Canada

- **Iheanacho B**., Pathirane M., and Wong W. S., (2013) "Towards Hybrid Thin Film – Nanowire Structures", Waterloo Engineering Innovate, Waterloo, ON, Canada

- Pathirane M., **Iheanacho B.,** Patchett S., Saini S., and Wong W. S. (2012) "Optical Characteristics of Solution-Grown ZnO Nanowires", NanoOntario, Waterloo, ON, Canada

Bibliography

[1] D. P. Event, “International Infrared Forum.” 2016.

[2] Y. Developpement, “Uncooled Infrared Imaging: Commercial & Military Applications - Market Report 2012-2017,” no. July. pp. 1–4, 2012.

[3] Y. Developpement, “Infrared detectors market 2015: From motion sensors to large arrays.” 2015.

[4] M. International, “Volume IRW - C : The World Market for Commercial and Dual - Use Infrared Imaging and Infrared Thermometry Equipment (2016 edition),” 2016. [Online]. Available: http://maxtech-intl.com. [Accessed: 24-Oct-2016].

[5] F. Prokoski, “History, current status, and future of infrared identification,” in *Proceedings IEEE Workshop on Computer Vision Beyond the Visible Spectrum: Methods and Applications (Cat. No.PR00640)*, 2000, pp. 5–14.

[6] A. Rogalski, “Infrared detectors: Status and trends,” *Prog. Quantum Electron.*, vol. 27, no. 2–3, pp. 59–210, 2003.

[7] A. Rogalski, “Recent progress in infrared detector technologies,” *Infrared Phys. Technol.*, vol. 54, no. 3, pp. 136–154, 2011.

[8] A. Singh, V. Srivastav, and R. Pal, “HgCdTe avalanche photodiodes: A review,” *Opt. Laser Technol.*, vol. 43, no. 7, pp. 1358–1370, 2011.

[9] A. Rogalski, “Infrared detectors: An overview,” *Infrared Phys. Technol.*, vol. 43, no. 3–5, pp. 187–210, 2002.

[10] T. Sprafke and J. W. Beletic, “High-Performance Infrared Focal Plane Arrays for Space Applications,” *Opt. Photonics News*, vol. 19, no. 6, p. 22, Jun. 2008.

[11] B. Nilsson, “Revolutionary New Transistor Technology for Flat Panel Displays,” in *SID Display Week 2014*.

[12] N. Shah, “Changing Trends in Camera & Display Resolutions in Smartphones,” Counterpoint Research, 2016.

[13] N. A. DiLello, D. K. Johnstone, and J. L. Hoyt, “Characterization of dark current in Ge-on-Si photodiodes,” *J. Appl. Phys.*, vol. 112, no. 5, p. 54506, 2012.

[14] G. G. Deng, Y. H. Zhang, and W. Z. Shen, “Design of a top mirror for the n-GaAs homojunction far-infrared/terahertz detectors,” *J. Appl. Phys.*, vol. 108, no. 7, pp. 1–6, 2010.

[15] R. Street, *Technology and Applications of Amorphous Silicon*, vol. 37. Berlin, Heidelberg: Springer Berlin Heidelberg, 2000.

[16] R.A. Street, *Hydrogenated amorphous silicon*, Cambridge. Cambridge University Press, 2005.

[17] J. Zhu, Z. Yu, G. F. Burkhard, C. M. Hsu, S. T. Connor, Y. Xu, Q. Wang, M. McGehee, S. Fan, and Y. Cui, “Optical absorption enhancement in amorphous silicon nanowire and nanocone arrays,” *Nano Lett*, vol. 9, no. 1, pp. 279–282, 2009.

[18] R. A. Street, P. Qi, R. Lujan, and W. S. Wong, “Reflectivity of disordered silicon nanowires,” *Appl. Phys. Lett.*, vol. 93, no. 16, pp. 3–5, 2008.

[19] M. Pathirane, B. Iheanacho, A. Tamang, C. H. Lee, R. Lujan, D. Knipp, and W. S. Wong, “Hybrid ZnO nanowire/a-Si:H thin-film radial junction solar cells using nanoparticle front contacts,” *Appl. Phys. Lett.*, vol. 107, no. 14, pp. 14–19, 2015.

[20] A. Tamang, M. Pathirane, R. Parsons, M. M. Schwarz, B. Iheanacho, V. Jovanov, V. Wagner, W. S. Wong, and D. Knipp, “Zinc oxide nanowire arrays for silicon core/shell solar cells,” *Opt. Express*, vol. 22, no. S3, p. A622, 2014.

[21] W. Choi, M. Y. Cho, A. Konar, J. H. Lee, G. B. Cha, S. C. Hong, S. Kim, J. Kim, D. Jena, J. Joo, and S. Kim, “High-detectivity multilayer MoS2 phototransistors with spectral response from ultraviolet to infrared,” *Adv. Mater.*, vol. 24, no. 43, pp. 5832–5836, 2012.

[22] S. Y. Han, K. T. Park, H. S. Jeon, Y. W. Heo, and B. S. Bae, “Optical Properties of a-SiGe:H Thin Film Transistor for Infrared Image Sensors in Touch Sensing Display,” *J. Disp. Technol.*, vol. 8, no. 10, pp. 617–622, 2012.

[23] S. Y. Han, K. S. Jeon, B. Cho, M. S. Seo, J. Song, and H. S. Kong, “Characteristics of a-SiGe:H thin film transistor infrared photosensor for touch sensing displays,” *IEEE J. Quantum Electron.*, vol. 48, no. 7, pp. 952–959, 2012.

[24] M. Z. Tidrow and W. R. Dyer, “Infrared sensors for ballistic missile defense,” *Infrared Phys. Technol.*, vol. 42, no. 3–5, pp. 333–336, 2001.

[25] M. Casalino, G. Coppola, M. Iodice, I. Rendina, and L. Sirleto, “Near-infrared sub-bandgap all-silicon photodetectors: State of the art and perspectives,” *Sensors*, vol. 10, no. 12, pp.

10571–10600, 2010.

[26] P. H. Cheng, H. X. Zhao, J. L. Bao, L. G. Wu, D. S. Li, and D. R. Yang, “Light absorption enhancement of amorphous silicon film coupled with metal nanoshells,” *J. Opt. Soc. Am. B-Optical Phys.*, vol. 30, no. 2, pp. 405–409, 2013.

[27] A. Luque, A. Martí, and C. Stanley, “Understanding intermediate-band solar cells,” *Nat. Photonics*, vol. 6, no. February, p. 146, 2012.

[28] Y. Okada, N. J. Ekins-Daukes, T. Kita, R. Tamaki, M. Yoshida, A. Pusch, O. Hess, C. C. Phillips, D. J. Farrell, K. Yoshida, N. Ahsan, Y. Shoji, T. Sogabe, and J.-F. Guillemoles, “Intermediate band solar cells: Recent progress and future directions,” *Appl. Phys. Rev.*, vol. 2, no. 2, p. 21302, Jun. 2015.

[29] B. K. Newman, J. T. Sullivan, M. T. Winkler, M. J. Sher, M. A. Marcus, S. Fakra, M. J. Smith, S. Gradecak, E. Mazur, and Buonassisi, “Illuminating the mechanism for sub-bandgap absorption in chalcogen-doped silicon materials for PV applications,” in *24th European Photovoltaic Solar Energy Conference*, 2009, no. September, pp. 236–238.

[30] J. E. Carey, C. H. Crouch, M. Shen, and E. Mazur, “Visible and near-infrared responsivity of femtosecond-laser microstructured silicon photodiodes.,” *Opt. Lett.*, vol. 30, no. 14, pp. 1773–1775, 2005.

[31] M.-J. Sher, Y.-T. Lin, M. T. Winkler, E. Mazur, C. Pruner, and A. Asenbaum, “Mid-infrared absorptance of silicon hyperdoped with chalcogen via fs-laser irradiation,” *J. Appl. Phys.*, vol. 113, no. 6, p. 63520, Feb. 2013.

[32] T. G. Kim, J. M. Warrender, and M. J. Aziz, “Strong sub-band-gap infrared absorption in silicon supersaturated with sulfur,” *Appl. Phys. Lett.*, vol. 88, no. 24, pp. 3–5, 2006.

[33] A. J. Said, D. Recht, J. T. Sullivan, J. M. Warrender, T. Buonassisi, P. D. Persans, and M. J. Aziz, “Extended infrared photoresponse and gain in chalcogen-supersaturated silicon photodiodes,” *Appl. Phys. Lett.*, vol. 99, no. 7, pp. 2011–2014, 2011.

[34] S. H. Pan, D. Recht, S. Charnvanichborikarn, J. S. Williams, and M. J. Aziz, “Enhanced visible and near-infrared optical absorption in silicon supersaturated with chalcogens,” *Appl. Phys. Lett.*, vol. 98, no. 12, pp. 2011–2014, 2011.

[35] R. R. Grote, B. Souhan, N. Ophir, J. B. Driscoll, K. Bergman, H. Bahkru, W. M. J. Green, and

R. M. Osgood, “Extrinsic photodiodes for integrated mid-infrared silicon photonics,” *Optica*, vol. 1, no. 4, p. 264, Oct. 2014.

[36] H. Siampour and Y. Dan, “Si nanowire phototransistors at telecommunication wavelengths by plasmon-enhanced two-photon absorption,” *Opt. Express*, vol. 24, no. 5, p. 4601, 2016.

[37] J. R. Sambles, G. W. Bradbery, and F. Yang, “Optical excitation of surface plasmons: An introduction,” *Contemp. Phys.*, vol. 32, no. 3, pp. 173–183, May 1991.

[38] D. Liu, D. Yang, Y. Gao, J. Ma, R. Long, C. Wang, and Y. Xiong, “Flexible Near-Infrared Photovoltaic Devices Based on Plasmonic Hot-Electron Injection into Silicon Nanowire Arrays,” *Angew. Chemie Int. Ed.*, vol. 55, no. 14, pp. 4577–4581, Mar. 2016.

[39] M. A. Nazirzadeh, F. B. Atar, B. B. Turgut, and A. K. Okyay, “Random sized plasmonic nanoantennas on Silicon for low-cost broad-band near-infrared photodetection.,” *Sci. Rep.*, vol. 4, p. 7103, 2014.

[40] J. Li, Z. R. R. Wasilewski, H. C. C. Liu, M. Buchanan, J. Li, Z. R. R. Wasilewski, and M. Buchanan, “Integrated quantum well intersub-band photodetector and light emitting diode,” *Electron. Lett.*, vol. 31, no. 10, pp. 832–833, May 1995.

[41] A. Kuo, “Novel Amorphous Silicon Thin-Film Transistor Structure for Flat-Panel Displays,” University of Michigan, 2008.

[42] Y. Suzuki, B. Iheanacho, A. Ahnood, P. Kathirgamanathan, W. Wong, and A. Nathan, “Electrical Characterization of Electrochemically Grown ZnO Nanorods using STM,” *MRS Proc.*, vol. 1391, no. 1540, p. mrsf11-1391-j07-57, Jan. 2012.

[43] Y. Kuang, K. H. M. Van Der Werf, Z. S. Houweling, M. Di Vece, and R. E. I. Schropp, “Design and photovoltaic performance of nanorod solar cells with amorphous silicon absorber layer thickness of only 25 nm,” *Conf. Rec. IEEE Photovolt. Spec. Conf.*, pp. 2212–2216, 2013.

[44] S. a Mann and E. C. Garnett, “Extreme Light Absorption in Thin Semiconductor Films Wrapped around Metal Nanowires,” *Nano Lett.*, vol. 13, no. 7, pp. 3173–3178, Jul. 2013.

[45] Q. G. Du, C. H. Kam, H. V. Demir, H. Y. Yu, and X. W. Sun, “Broadband absorption enhancement in randomly positioned silicon nanowire arrays for solar cell applications.,” *Opt. Lett.*, vol. 36, no. 10, pp. 1884–6, 2011.

[46] N. Huang, C. Lin, and M. L. Povinelli, “Broadband absorption of semiconductor nanowire

arrays for photovoltaic applications," *J. Opt.*, vol. 14, no. 2, p. 24004, 2012.

[47] V. E. Ferry, M. A. Verschuuren, H. B. T. Li, R. E. I. Schropp, H. A. Atwater, and A. Polman, "Improved red-response in thin film a-Si:H solar cells with soft-imprinted plasmonic back reflectors," *Appl. Phys. Lett.*, vol. 95, no. 18, pp. 95–98, 2009.

[48] E. Tutuc, J. Appenzeller, M. C. Reuter, and S. Guha, "Realization of a Linear Germanium Nanowire p−n Junction," *Nano Lett.*, vol. 6, no. 9, pp. 2070–2074, Sep. 2006.

[49] Z. Huizhao and X. Shoubin, "Synthesis and Properties of GaN Nanowires by RF Magnetron Sputtering Zhuang Huizhao 1 and Xue Shoubin 2 1," *Chinese J. Phys.*, vol. 46, no. 2, pp. 163–169, 2008.

[50] Y. Wu and P. Yang, "Direct Observation of Vapor−Liquid−Solid Nanowire Growth," *J. Am. Chem. Soc.*, vol. 123, no. 13, pp. 3165–3166, Apr. 2001.

[51] J. Westwater, "Growth of silicon nanowires via gold/silane vapor–liquid–solid reaction," *J. Vac. Sci. Technol. B Microelectron. Nanom. Struct.*, vol. 15, no. 3, p. 554, May 1997.

[52] C. Y. Lee, T. Y. Tseng, S. Y. Li, and P. Lin, "Growth of Zinc Oxide Nanowires on Silicon (100)," *Tamkang J. Sci. Eng.*, vol. 6, no. 2, pp. 127–132, 2003.

[53] S. Baruah and J. Dutta, "Hydrothermal growth of ZnO nanostructures," *Sci. Technol. Adv. Mater.*, vol. 10, no. 1, p. 13001, 2009.

[54] W. Qin, C. Yang, R. Yi, and G. Gao, "Hydrothermal Synthesis and Characterization of Single-Crystalline a-Fe2O3 Nanocubes," *J. Nanomater.*, vol. 2011, pp. 1–5, 2011.

[55] K. Govender, D. S. Boyle, P. B. Kenway, and P. O'Brien, "Understanding the factors that govern the deposition and morphology of thin films of ZnO from aqueous solution," *J. Mater. Chem.*, vol. 14, no. 16, pp. 2575–2591, 2004.

[56] L. Schmidt-Mende and J. L. MacManus-Driscoll, "ZnO – nanostructures, defects, and devices," *Mater. Today*, vol. 10, no. 5, pp. 40–48, May 2007.

[57] M. N. R. Ashfold, R. P. Doherty, N. G. Ndifor-Angwafor, D. J. Riley, and Y. Sun, "The kinetics of the hydrothermal growth of ZnO nanostructures," *Thin Solid Films*, vol. 515, no. 24 SPEC. ISS., pp. 8679–8683, 2007.

[58] S. Music, S. Popovic, M. Maljkovic, and E. Dragcevic, "Influence of synthesis procedure on

the formation and properties of zinc oxide," *J. Alloys Compd.*, vol. 347, no. 1–2, pp. 324–332, 2002.

[59] D. Chen, X. Jiao, and G. Cheng, "Hydrothermal synthesis of zinc oxide powders with different morphologies," *Solid State Commun.*, vol. 113, no. 6, pp. 363–366, 1999.

[60] Y. Chen, R. Yu, Q. Shi, J. Qin, and F. Zheng, "Hydrothermal synthesis of hexagonal ZnO clusters," *Mater. Lett.*, vol. 61, no. 22, pp. 4438–4441, 2007.

[61] F. Li, L. Hu, Z. Li, and X. Huang, "Influence of temperature on the morphology and luminescence of ZnO micro and nanostructures prepared by CTAB-assisted hydrothermal method," *J. Alloys Compd.*, vol. 465, no. 1–2, pp. 14–19, 2008.

[62] L. Tang, X.-B. Bao, H. Zhou, and A.-H. Yuan, "Synthesis and characterization of ZnO nanorods by a simple single-source hydrothermal method," *Phys. E Low-dimensional Syst. Nanostructures*, vol. 40, no. 4, pp. 924–928, 2008.

[63] X. Y. Zhang, J. Y. Dai, H. C. Ong, N. Wang, H. L. W. Chan, and C. L. Choy, "Hydrothermal synthesis of oriented ZnO nanobelts and their temperature dependent photoluminescence," *Chem. Phys. Lett.*, vol. 393, no. 1–3, pp. 17–21, 2004.

[64] Z. Li, X. Huang, J. Liu, Y. Li, X. Ji, and G. Li, "Growth and comparison of different morphologic ZnO nanorod arrays by a simple aqueous solution route," *Mater. Lett.*, vol. 61, no. 22, pp. 4362–4365, 2007.

[65] C. Xu and D. Gao, "Two-Stage Hydrothermal Growth of Long ZnO Nanowires for Efficient TiO 2 Nanotube-Based Dye-Sensitized Solar Cells," *J. Phys. Chem. C*, vol. 116, no. 12, pp. 7236–7241, Mar. 2012.

[66] T. Andelman, Y. Gong, M. Polking, M. Yin, I. Kuskovsky, G. Neumark, and S. O'Brien, "Morphological control and photoluminescence of zinc oxide nanocrystals.," *J. Phys. Chem. B*, vol. 109, no. 30, pp. 14314–14318, 2005.

[67] K. O. Choi, S. H. Yoon, W. S. Kim, K. H. Lee, C. M. Yang, J. H. Han, C. J. Kang, Y. J. Choi, and T. S. Yoon, "Morphological dependence of hydrothermally synthesized ZnO nanowires on synthesis temperature and molar concentration," *Phys. Status Solidi Appl. Mater. Sci.*, vol. 210, no. 7, pp. 1448–1453, 2013.

[68] J. Liu, J. She, S. Deng, J. Chen, and N. Xu, "Ultrathin Seed-Layer for Tuning Density of ZnO

Nanowire Arrays and Their Field Emission Characteristics," *J. Phys. Chem. C*, vol. 112, no. 31, pp. 11685–11690, Aug. 2008.

[69] M. R. Esmaeili-Rad, N. P. Papadopoulos, M. Bauza, A. Nathan, and W. S. Wong, "Blue-light-sensitive phototransistor for indirect X-ray image sensors," *IEEE Electron Device Lett.*, vol. 33, no. 4, pp. 567–569, 2012.

[70] H. W. Deckman, C. R. Wronski, H. Witzke, and E. Yablonovitch, "Optically enhanced amorphous silicon solar cells," *Appl. Phys. Lett.*, vol. 42, no. 11, pp. 968–970, 1983.

[71] W. S. Wong, M. J. Chow, M. Pathirane, B. Iheanacho, and C. Lee, "Heterogeneously Integrated Nanowires and Thin Films for Flexible Electronics," *AM-FPD*, vol. S1, pp. 37–40, 14AD.

[72] J. R. Abelson, "Plasma Deposition of Hydrogenated Amorphous Silicon : Studies of the Growth Surface," *Appl. Phys.*, vol. A56, pp. 493–512, 1993.

[73] W. G. J. H. M. van Sark, "Chapter 1 - Methods of deposition of hydrogenated amorphous silicon for device applications," *Handb. Thin Film.*, vol. 30, pp. 1–102, 2002.

[74] B. Pratt and R. Weil, "Post-Hydrogenation of Evaporated aSi," *J. Non. Cryst. Solids*, vol. 89, pp. 9–12, 1987.

[75] B. Ahn, K. Usami, H. Kanoh, and O. Sugiura, "The Effects of Post-Hydrogenation on Amorphous-Silicon Thin-Film Transistors," *Electron. Commun. Japan, Part 2*, vol. 76, no. 10, pp. 192–198, 1993.

[76] R. A. Street, W. S. Wong, and R. Lujan, "Low-temperature amorphous silicon p-i-n photodiodes," *Phys. status solidi*, vol. 246, no. 8, pp. 1854–1857, Aug. 2009.

[77] R. A. Street, "Doping and the Fermi Energy in Amorphous Silicon," *Phys. Rev. Lett.*, vol. 49, no. 16, pp. 1187–1190, Oct. 1982.

[78] T. N. Ng, R. A. Lujan, S. Sambandan, R. A. Street, S. Limb, and W. S. Wong, "Low temperature a-Si:H photodiodes and flexible image sensor arrays patterned by digital lithography," *Appl. Phys. Lett.*, vol. 91, no. 6, pp. 2005–2008, 2007.

[79] W. E. Howard, "Thin Film Transistors," in *Thin Film Transistors*, C. R. and P. A. Kagan, Ed. New York: Marcel Dekker Inc, 2003.

[80] R. A. Street, “Thin-film transistors,” *Adv. Mater.*, vol. 21, no. 20, pp. 2007–2022, 2009.

[81] M. G. Kanatzidis, “Semiconductor physics: quick-set thin films.,” *Nature*, vol. 428, no. 6980, pp. 269–271, 2004.

[82] E. Fortunato, P. Barquinha, and R. Martins, “Oxide semiconductor thin-film transistors: A review of recent advances,” *Adv. Mater.*, vol. 24, no. 22, pp. 2945–2986, 2012.

[83] F. Dehghan Nayeri and E. Asl Soleimani, “Influence of seed layers on the vertical growth of Zno nanowires by low-temperature wet chemical bath deposition on Ito-coated glass substrate,” *Exp. Tech.*, vol. 38, no. 4, pp. 13–20, 2014.

[84] J. Song and S. Lim, “Effect of Seed Layer on the Growth of ZnO Nanorods,” *J. Phys. Chem. C*, vol. 111, no. 2, pp. 596–600, 2007.

[85] T. Ma, M. Guo, M. Zhang, Y. Zhang, and X. Wang, “Density-controlled hydrothermal growth of well-aligned ZnO nanorod arrays.,” *Nanotechnology*, vol. 18, no. 3, p. 35605, 2007.

[86] W.-Y. Wu, C.-C. Yeh, and J.-M. Ting, “Effects of Seed Layer Characteristics on the Synthesis of ZnO Nanowires,” *J. Am. Ceram. Soc.*, vol. 92, no. 11, pp. 2718–2723, Nov. 2009.

[87] Q. Li, V. Kumar, Y. Li, H. Zhang, T. J. Marks, and R. P. H. Chang, “Fabrication of ZnO Nanorods and Nanotubes in Aqueous Solutions,” *Chem. Mater.*, vol. 17, no. 5, pp. 1001–1006, Mar. 2005.

[88] L. Tsakalakos, J. Balch, F. Fronheiser, S. F. Shih M.-Y. LeBoeuf, M. Pietrzykowski, P. J. Codella, B. A. Korevaar, O. Sulima, J. Rand, A. Davuluru, and R. Rapolc, “Strong broadband optical absorption in silicon nanowire films,” *J. Nanophotonics*, vol. 1, no. 13552, pp. 1–10, 2007.

[89] A. V. Singh, M. Kumar, R. M. Mehra, A. Wakahara, and A. Yoshida, “Al-doped zinc oxide (ZnO : Al) thin films by pulsed laser,” *J. Indian Instrum. Sci.*, vol. 81, pp. 527–533, 2001.

[90] J. L. Zhao, X. W. Sun, H. Ryu, and Y. B. Moon, “Thermally stable transparent conducting and highly infrared reflective Ga-doped ZnO thin films by metal organic chemical vapor deposition,” *Opt. Mater. (Amst).*, vol. 33, no. 6, pp. 768–772, 2011.

[91] Q.-B. Ma, Z.-Z. Ye, H.-P. He, L.-P. Zhu, J.-Y. Huang, Y.-Z. Zhang, and B.-H. Zhao, “Influence of annealing temperature on the properties of transparent conductive and near-infrared reflective ZnO:Ga films,” *Scr. Mater.*, vol. 58, no. 1, pp. 21–24, 2008.

[92] P. F. Cai, J. B. You, X. W. Zhang, J. J. Dong, X. L. Yang, Z. G. Yin, and N. F. Chen, "Enhancement of conductivity and transmittance of ZnO films by post hydrogen plasma treatment," *J. Appl. Phys.*, vol. 105, no. 8, 2009.

[93] S. Lee, M. Gunes, C. R. Wronski, N. Maley, and M. Bennett, "Effect of midgap states in intrinsic hydrogenated amorphous silicon on sub-band-gap photoconductivity," *Appl. Phys. Lett.*, vol. 59, no. 13, pp. 1578–1580, 1991.

[94] E. Yahya and H. R. Shanks, "Density Of States At Mid Gap In Hydrogenated Amorphous Silicon," in *SPIE Vil 653 Optical Materials Technology for Energy Efficiency and Solar Energy Conversion V*, 1986, pp. 315–320.

[95] W.S.Lau, *Infrared Characterization for Microelectronics*. WORLD SCIENTIFIC, 1999.

[96] S. E. Ready, J. B. Boyce, and C. C. Tsai, "Structure of Hydrogen in Microcrystalline and Amorphous Silicon: an NMR Comparison," *MRS Proc.*, vol. 118, p. 103, Jan. 1988.

[97] D. Yongchang, Z. Yufeng, Y. Datong, Z. Guanghua, and H. Ruqi, "The distribution of density of gap states for phosphorus doped amorphous silicon measured by DLTS," *J. Electron.*, vol. 2, no. 1, pp. 67–72, 1985.

[98] Exo Terra, "Infrared Basking Spot Lamp," 2016. [Online]. Available: http://www.exo-terra.com/en/products/infrared_basking_spot_lighting.php.

[99] R. A. Street, "Long-time transient conduction in a-Si:H p─i─n devices," *Philos. Mag. Part B*, vol. 63, no. 6, pp. 1343–1363, Jun. 1991.

[100] R. A. Street, "Thermal generation currents in hydrogenated amorphous silicon p-i-n structures," *Appl. Phys. Lett.*, vol. 57, no. 13, p. 1334, Sep. 1990.

[101] J. K. Arch and S. J. Fonash, "Origins of reverse bias leakage currents in hydrogenated amorphous silicon p-i-n detector structures," *Appl. Phys. Lett.*, vol. 60, no. 6, p. 757, 1992.

[102] A. K. Viswanath, "SURFACE AND INTERFACIAL RECOMBINATION IN SEMICONDUCTORS," in *Handbook of Surfaces and Interfaces of Materials*, vol. 1, Hari Singh Nalwa, Ed. Academy Press, 2001, pp. 217–284.

[103] D. J. Fitzgerald and A. S. S. Grove, "Surface recombination in semiconductors," *Surf. Sci.*, vol. 9, no. 2, pp. 347–369, Jan. 1968.

[104] C.-Y. Chen, J. Ramon, D. Retamal, I. Wu, D. Lien, M. Chen, Y. Ding, C. E. T. Al, J. R. D. Retamal, I. Wu, D. Lien, M. Chen, Y. Ding, Y.-L. Chueh, C.-I. Wu, and J.-H. He, "Probing Surface Band Bending of Surface-Engineered Metal Oxide Nanowires," *ACS Nano*, vol. 6, no. 11, pp. 9366–9372, Nov. 2012.

Appendix A

Photodiode Mask Floor Plan

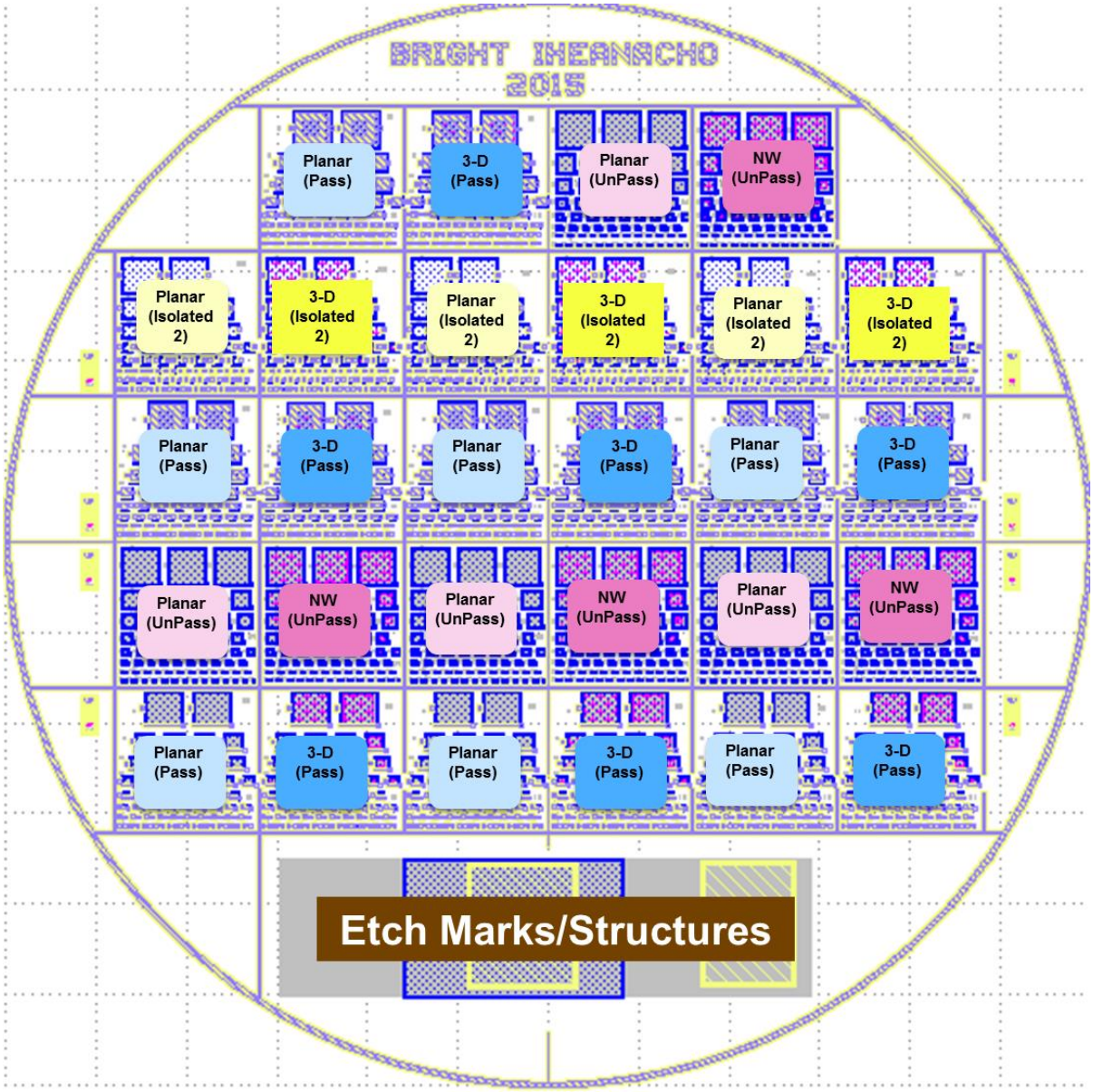

Appendix B

Process Summaries